Dissertation

submitted to the

Combined Faculty of Mathematics, Engineering and Natural Sciences

of Heidelberg University, Germany

for the degree of

Doctor of Natural Sciences

Put forward by

Susan van der Woude

born in: Groningen, The Netherlands

Oral examination: 15th of December 2021

This page was intentionally left blank.

Impacts of an extra scalar and a strongly coupled dark sector on the physics of the early universe

Gravitational waves and Leptogenesis

Referees:

Prof. Dr. Dr. h.c. Manfred Lindner

Jun.-Prof. Dr. Susanne Westhoff

This page was intentionally left blank.

Acknowledgements

First of all i would like to thank my supervisor Manfred Lindner for giving me a PhD position in his amazing group at the Max Planck Insitut für Kernphysik and for guiding me towards interesting projects these past four years. I would also like to thank Susanne Westhoff for agreeing to be the second referee and Björn Malte Schäfer and Teresa Marrodán Undagoitia for being on the committee for my PhD defense.

Many thanks to my collaborators, Jisuke Kubo, Alexander Helmboldt and Oliver Fischer; it has been great working with you and discussing challenging projects with you.

I would also like to express my gratitude towards my office mate Thomas Hugle and my fellow PhD students Christian Doering, Ting Cheng, Tim Herbermann and Thomas Rink for proofreading parts of this thesis and giving me many useful suggestions to improve it.

In addition i would like to thank all former and current master students, PhD students, post docs and senior staff from the Lindner group for making the past four years an enjoyable and educational experience. Many thanks also to Anja Berneiser, Britta Schwarz and the IT-departement for making sure things kept running smoothly and quickly fixing any problems encountered.

I would also like to thank all fellow students and my teachers Frau Noki and Frau Wolff from my german class at the university of Heidelberg for providing some much needed distraction from lockdowns and home-office during COVID times.

Many thanks to my parents, Pieter and Greet, my brother Tim and my sister Debby for always supporting me even though the distance was sometimes hard.

Last but least, none of this would have been possible without the continuous support from my boyfriend Manuel. Thanks for always being there, even if it was not always possible to be together in person, and for encouraging me to keep working even when projects got stuck.

This page was intentionally left blank.

Abstract

In this thesis two aspects of Standard Model extensions are discussed. Firstly, a Standard Model extension with a strongly coupled hidden sector is investigated. For suitable parameters, such a hidden sector is expected to undergo a first order phase transition, consequently resulting in the production of gravitational waves. Due to their strongly coupled nature, effective low energy models have to be used to determine the phase transition dynamics and calculate the predicted gravitational wave signals. It is shown that different effective models in general predict similar but by no means equal gravitational wave signals. Thus showing that calculations from first principles, like lattice calculations, are needed. Secondly, scalar extensions are discussed, which can result in a first order electroweak phase transition. In contrast to phase transitions in strongly coupled sectors, the dynamics of these phase transitions is rather well known. Consequently, the gravitational wave signals from the electroweak phase transition can be predicted reasonably well. In this thesis, instead of phase transition dynamics, a different aspect of scalar extensions will be discussed, namely their effect on leptogenesis via oscillations. Our results show that a scalar extension in general reduces the produced baryon asymmetry of the Universe. In the future these results, together with possible proof of a first order phase transition, can be used to further constrain scalar extensions.

Zusammenfassung

In dieser Doktorarbeit werden zwei Aspekte von Standardmodellerweiterungen diskutiert. Zuerst wird eine Erweiterung des Standardmodells mit einem stark gekoppelten verborgenen Sektor untersucht. Für geeignete Parameter wird erwartet, dass ein solcher verborgener Sektor einen Phasenübergang erster Ordnung durchläuft, der zur Erzeugung von Gravitationswellen führt. Aufgrund ihrer stark gekoppelten Natur müssen effektive Theorien bei niederigen Energien verwendet werden, um die Dynamik des Phasenübergangs zu bestimmen und die vorhergesagten Gravitationswellensignale zu berechnen. Es wird gezeigt, dass verschiedene effektive Modelle im Allgemeinen ähnliche, aber keineswegs gleiche Gravitationswellensignale vorhersagen. Dies zeigt, dass Berechnungen aus fundamentalen Prinzipien, wie z.B. Berechnungen auf einem Gitter, notwendig sind. Zweitens werden skalare Erweiterungen diskutiert, die eine elektroschwachen Phasenübergang erster Ordnung ermöglichen können. Im Gegensatz zu stark gekoppelten Sektoren ist die Dynamik dieses Phasenübergangs recht gut bekannt. Folglich können die Gravitationswellensignale aus dem elektroschwachen Phasenübergang recht gut vorhergesagt werden. In dieser Arbeit wird, statt Phasenübergangsdynamik, ein anderer Aspekt von skalaren Erweiterungen diskutiert, nämlich ihr Einfluss auf Leptogenese mittels Oszillationen. Unsere Ergebnisse zeigen, dass eine Skalarerweiterung im Allgemeinen die erzeugte Baryon-Asymmetrie des Universums reduziert. In der Zukunft können diese Ergebnisse, zusammen mit einem möglichen Nachweis eines Phasenübergangs erster Ordnung, genutzt werden, um skalare Erweiterungen weiter einzuschränken.

This page was intentionally left blank.

Contents

Chapter 1

Introduction

Almost all physical processes describing the evolution of the Universe from the Big Bang to the present day can be explained by the Standard Model (SM), General Relativity (GR) and the ΛCDM cosmological model. The SM was developed in the second half of the previous century and is able to extremely well describe all processes encountered in daily life as well as processes observed in precision experiments or collider experiments. Everything ranging from electromagnetism and nuclear fusion to collider physics: the Standard Model can to high precision explain it. In the past decades all elementary particles predicted by the Standard Model have been observed. This search was concluded by the observation of the Higgs boson in 2012 [3, 4]. As of now collider experiments have not yet found clear signals of particles not included in the Standard Model.

Gravity is described by the theory of General Relativity, first developed by Albert Einstein around 1915 [5]. The theory was confirmed by measurements of for example the perihelion precession of Mercury as well as the deflection of light due to the sun, see e.g. ref. [6]. Furthermore, the observation of the first gravitational wave signals from a Black Hole binary merger by the LIGO and VIRGO collaboration [7] provided an excellent test of the theory of General Relativity in the strong gravity regime, which the theory passed with flying colours [8].

In order to explain how the universe evolved from the Big Bang till the present time the ΛCDM has been developed, see e.g. [9]. The ΛCDM is a cosmological model which describes Standard Model particles as well as cold Dark Matter in an expanding universe. It is only able to predict for example the correct Cosmic Microwave Background (CMB), measured by for example WMAP [10] or Planck [11] and predict the correct large scale structure of the Universe, if an extra matter and energy component are introduced. The

matter component is expected to not interact (or only weakly) with the particles of the SM. This component is usually called Dark Matter. Additionally an inflationary component needs to be included, called Dark Energy. These two new components comprise respectively 23% and 73% of the universe [11].

Thus, in order to explain the CMB within the ΛCDM model we have to conclude that about 95% of the Universe does not consist out of the particles described by the Standard Model. This observation offers one of the strongest hints for physics beyond the Standard Model. The origin and even the nature of the Dark Matter and Dark Energy components are almost completely unknown. Theories have been coined which contain Dark Matter candidates with masses covering the complete mass range, from the smallest masses of $\mathcal{O}(\mu\text{eV})$ to the largest masses of $\mathcal{O}(10^9\ \text{GeV})$ [12]. Note that Dark Matter does not necessarily have to be an elementary particle but can be composite in nature or even constitute primordial black holes [13]. Explanations for Dark Energy are maybe even more diverse and exotic [14], ranging from a simple inflaton field to models with modified gravity [15].

Apart from the issues relating to Dark Matter and Dark Energy, results from precision experiments hint towards more conflicts between experiments and the Standard Model predictions. The anomalies which are showing up in experimental data are for example the muon magnetic moment [16] and the flavour anomalies [17]. Additionally, there is also the problem of the unexplained Baryon Asymmetry of the Universe (BAU) [18], non-zero neutrino masses and the tension between early and late time measurements of the Hubble constant [19].

Aside from these hints from experiments there are also more fundamental problems with the Standard Model, these include the Hierarchy problem and the unknown origin of the many parameters of the Standard Model. Lastly, unification of gravity and particle physics at the Planck scale can not be explained within the SM and GR.

A lot of research on Beyond the Standard Model (BSM) models (and also ΛCDM extensions) is focussed on developing extensions which can explain one or more of the issues mentioned above. There are two main ways in which one can approach building a BSM model, the *bottom-up* or the *top-down* approach. Within a *bottom-up* approach additional particles are added to the Standard Model to see if and how they can alleviate the Standard Model problems. Alternatively, in a *top-down* one can start from the more conceptual, structural problems of the Standard Model.

In this thesis two aspects of BSM models will be discussed. In part A we will look into strongly coupled extension and their gravitational waves (GW) signal, whereas part B will be concerned with the consequences of scalar extensions for leptogenesis

via oscillations. These extension have in common that they are both rather minimalistic extensions of the Standard Model. Both extensions also contain a particle which could be a suitable Dark Matter candidate. The scalar and dark sector extension have another characteristic in common; namely the fact that they could each be included in a *classically conformal* SM extension. In conformal scalar extensions the mass scale is obtained via loop corrections through the Coleman-Weinberg potential [20]. See e.g. ref. [21] for an example of an explicit model. On the other hand, in strongly coupled conformal sectors mass scales are obtained through *non-perturbative* effects, similar to what occurs in QCD, see e.g. ref. [22, 23] for examples of explicit models.

Additionally, strongly coupled dark sectors as well as scalar extensions predict, for suitable model parameters, the existence of a first order phase transition in the early universe. These first order phase transitions can lead to the production of observable gravitational wave (GW) signals. Since the first detection of gravitational waves occurred in 2016 [7] and considering the many experiments planned to measure gravitational waves from phase transitions these type of models have become increasingly interesting to look at. Note that without gravitational wave signals both a scalar extension and a strongly coupled dark sector could easily be so weakly coupled to the Standard Model that conventional experiments like the Large Hadron Collider at CERN would never find signals. Whereas GW signals from a scalar extension of the Standard Model have been extensively investigated, see e.g. [24, 25], first order phase transitions in strongly coupled sectors are understood significantly less well.

In this thesis some aspects of the scalar and dark sector SM extension will be investigated. The goal of part A will be to understand the dynamics of phase transitions in strongly coupled hidden sectors better. We will show how effective models can be used to investigate a phase transition (PT) in strongly coupled sectors. Like in Quantum Chromodynamics (QCD), a strongly coupled dark sector can undergo a Chiral Phase Transition (χPT). Whereas this PT is crossover in QCD, the dark sector can have a first order χPT. Thus allowing for the possibility of measurable gravitational wave signals in the future. Due to the strongly coupled nature of such a dark sector the traditional perturbative methods in Quantum Field Theory (QFT) using Feynman diagrams, cannot be applied, therefore other methods are needed. We will be using low-energy effective models to describe the dynamics of QCD-like theories. Part A is organized as follows: In chapter 2 strongly coupled theories and several effective models will discussed. Once we have introduced these models they can be used to investigate the GW signal from a first order PT in a strongly coupled sector. The basics of GW signals will be discussed in chapter chapter 3, whereas the results will be discussed in chapter 4. The research presented in this part will allow us to answer two main questions:

1. Do low-energy effective models have similar effective potentials and/or predict similar GW signals?

2. Can these GW signals be measured in current or future experiments?

Part A is based on work published in collaboration with Jisuke Kubo and Alexander Helmboldt [1].

The dynamics of first order phase transitions in scalar extensions is already rather well understood, see e.g. ref. [26]. Also the predicted gravitational wave signals in such models are extensively researched see e.g. refs.[24, 27, 28] and will not be further discussed here. However, if gravitational wave experiments do find hints for the existence of a first order phase transition it would be interesting to investigate in what other ways a scalar impacts the physics of the early universe. We will therefore looks at the effect of a scalar on one of the most pressing issues of the Standard Model, the BAU. The aim of part B is to determine if and how a scalar extension of the SM affects ARS leptogenesis [29] as used in for example the νMSM model [30]. In chapter 5 leptogenesis will be discussed with special emphasis on ARS leptogenesis and the νMSM. In chapter 6 we will look at the scalar extension of the νMSM and determine how the scalar affects (ARS) leptogenesis through scalar decay and thermal effects. The main question we would like to answer through this research is if scalars can enhance leptogenesis production in ARS leptogenesis. Part B is based on work in collaboration with Oliver Fischer and Manfred Lindner, which will be published soon [2].

Throughout this thesis we will be working with natural units, i.e., $\hbar = c = k_B = 1$ and use the following convention for the metric tensor, $\eta = \text{diag}(+1, -1, -1, -1)$.

Part A

Strongly coupled SM extensions and their GW signals

Chapter 2

Effective models of strongly interacting sectors

In this chapter we will look into strongly interacting theories, with the main focus on QCD-like theories, i.e. theories with a SU(3) gauge symmetry. Hidden strongly coupled sectors are interesting because they are included in many dark matter models. They are for instance used in models of strongly interacting dark matter (SIMP) [31, 32] and composite Higgs models, [33, 34]. See ref. [35] for a comprehensive overview. For a suitable choice of parameters, QCD-like theories can exhibit a first order chiral phase transition (χPT).

Due to their strong coupling at low energies these theories can not be described by the standard perturbative methods of QFT. As a result, no calculations from first principles exists which are able to investigate for example the dynamics of phase transitions in these sectors. Previous research on gravitational wave signals and phase transitions in strongly coupled hidden sectors usually relied on certain estimates, see e.g. refs. [35–37]. However, instead of relying on estimates it is possible to approximate the dynamics of these theories at low energies using effective models. The work presented in part A offers a first study towards using effective models to describe phase transitions and predict gravitational waves signals in strongly coupled models.

Note that, due to advances in computational methods, it has also become possible to explore strongly coupled models at low energies using lattice field theory. This has for example already been done for phase transitions in purely scalar models [38] and for a first order electroweak phase transition [39, 40]. Unfortunately, lattice calculations

are not yet able to fully determine the dynamics of phase transitions and the resulting gravitational wave signals when fermions are involved [1].

The outline of this chapter is as follows; after briefly reviewing QCD-like theories we will introduce three of the existing effective models, namely the Nambu-Jona-Lasinio (NJL) model, the Polyakov loop enhanced NJL (PNJL) model and the linear sigma model (LSM). For each of these models the effective potential will be derived. This will be needed later to characterize the phase transitions and subsequently calculate the gravitational wave signal produced during a first order Chiral Phase Transition (χPT). This chapter is based on work done together with J.Kubo and A.Helmboldt [1].

2.1 Strongly coupled theories

The best-known example of a strongly coupled theory is QCD, see e.g. ref. [42] for a review. Within the Standard Model of particle physics it is the theory which describes the strong interactions between gluons and quarks. QCD exhibits interesting properties like colour confinement, asymptotic freedom and a χPT. As we will later see, for QCD this phase transition is expected to be a crossover, however, with the right choice of (dark) fermion masses the χPT in a dark sector can be first order.

The QCD-like theories we will be investigating have a SU(3) gauge symmetry, for n_f flavours and gauge coupling g the Lagrangian can be written as:

$$\mathcal{L}_{\mathrm{SU(3)}} = \sum_{i=1}^{n_f} \bar{q}_i (i\gamma_\mu D^\mu - m_i) q_i - \frac{1}{4} G^a_{\mu\nu} G_a^{\mu\nu} \quad \text{with} \tag{2.1a}$$

$$D_\mu = \partial_\mu - igT_a A^a_\mu \,, \tag{2.1b}$$

$$G_{\mu\nu} = \partial_\mu A^a_\nu - \partial_\nu A^a_\mu + g f_{abc} A^b_\mu A^c_\nu \,. \tag{2.1c}$$

q is the fermion field, with quark masses m_i, and A_μ is the gluon field. The index $i = 1 \dots n_f$ is the flavour index while the index a runs from $1 \cdots 8$ and corresponds to the eight gauge bosons (gluons). $T_a = \lambda_a/2$, where λ_a are the Gell-Mann matrices, which satisfy $\mathrm{Tr}(T_a T_b) = \delta_{ij}/2$. f_{abc} are defined through the commutator of the Gell-Mann matrices as $[\lambda_a, \lambda_b] = 2if^{abc}\lambda_c$. The colour index $\alpha = 1, 2, 3$ has been suppressed but is implicitly summed over. The same holds for the spinor indices.

[1] Very recently in ref. [41] lattice calculations were used in combination with effective theories to calculate GW signals from phase transitions in strongly coupled models, their results seem qualitatively rather similar.

The fermionic part of this Lagrangian can also be written in terms of the chiral fields q_L and q_R, with $q = q_L + q_R$:

$$\mathcal{L}_m = \sum_{i=1}^{n_f} \bar{q}_i (\mathrm{i}\not{D} - m_i) q_i = \sum_{i=1}^{n_f} \left[\bar{q}_{Li} \mathrm{i}\not{D} q_{Li} + \bar{q}_{Ri} \mathrm{i}\not{D} q_{Ri} - m_i (\bar{q}_{Li} q_{Ri} + \mathrm{h.c.}) \right] . \tag{2.2}$$

In this form it becomes clear that apart form the SU(3) gauge symmetry the Lagrangian also has global symmetries. In the chiral limit, i.e. $m_i = 0$, this symmetry group is given by:

$$\mathcal{G}' = \mathrm{U}(n_f)_L \times \mathrm{U}(n_f)_R = \mathrm{SU}(n_f)_V \times \mathrm{SU}(n_f)_A \times \mathrm{U}(1)_V \times \mathrm{U}(1)_A \tag{2.3}$$

Note that $\mathrm{U}(n_f) \cong \mathrm{SU}(n_f) \times \mathrm{U}(1)$.

One can show the invariance of the (matter part) of the Lagrangian explicitly by looking at how $q_{(L/R)}$ transforms under each global symmetry. The Dirac spinor q transforms under $\mathrm{U}(1)_V$ and $\mathrm{U}(1)_A$ as

$$q \to \mathrm{e}^{\mathrm{i}\vartheta} q \qquad \text{and} \qquad q \to \mathrm{e}^{\mathrm{i}\vartheta_5 \gamma_5} q \, . \tag{2.4}$$

Whereas the chiral components q_L and q_R transform under $\mathrm{SU}(3)_L$ and $\mathrm{SU}(3)_R$ as

$$q_L \to U_L q_L \qquad \text{and} \qquad q_R \to U_R q_R \, , \tag{2.5}$$

with U_L and U_R unitary matrices which have a determinant equal to one. Substituting these transformations in the Lagrangian it is clear that for $m = 0$ the Lagrangian is invariant. Note that a non-zero mass term in the Lagrangian will cause the left and right-handed fermion fields to mix and $\mathrm{SU}(3)_L \times \mathrm{SU}(3)_R$ will subsequently be broken down to $\mathrm{SU}(3)_V$.

$\mathcal{G}'$ is the symmetry group on the classical level. It is well known that quantum corrections break the U(1) axial symmetry *explicitly*. This is called the chiral anomaly or the Adler-Bell-Jackiw anomaly [43, 44].

Including quantum corrections the global symmetry group of eq. (2.2) is thus:

$$\mathcal{G} = \mathrm{SU}(n_f)_V \times \mathrm{SU}(n_f)_A \times \mathrm{U}(1)_V \, . \tag{2.6}$$

Due to non-perturbative (strong coupling) effects the quarks will form a condensate $\langle \bar{q} q \rangle \neq 0$, which, similar to an explicit quark mass, will (spontaneously) break the symmetry group $\mathcal{G} \to \mathrm{SU}(n_f)_V \times \mathrm{U}(1)_V$. The symmetry is expected to be restored at high temperatures due to thermal effects.

The breaking of this symmetry is accompanied by the existence of $n_f^2 - 1$ massless Goldstone bosons. If the Lagrangian already explicitly breaks the chiral symmetry, through for example non-zero quark masses, the Goldstone bosons will only be pseudo-Goldstone bosons, which have a small but non-zero mass. In QCD the pseudo-Goldstone bosons correspond to the three pions with roughly equal masses, due to the finite mass of the two lightest quarks, the u and d quark, these pions are pseudo-Goldstone instead of Goldstone bosons.

The chiral phase transition signifies the transition from a quark-gluon plasma at high temperatures to a state which is described by quark condensates, i.e., mesons and baryons, at low temperatures. The nature of the χPT of QCD has been a topic of research for many years and will depend in general on the size of quark masses and the number of flavours [45].

2.1.1 The Phase Diagram of QCD

In the early universe we differentiate between roughly three types of transitions; the crossover, the second order phase transition and the first order phase transition. The crossover is a transition which is completely smooth and thus in the strictest sense not a true phase transition; no symmetries are broken and there is no singularity [46]. Whereas a second order PT is characterized by a continuous change from one phase to another, a first order PT is a discontinuous process where the new phase first develops in bubbles (from tunnelling) which subsequently expand and collide till the PT has completed. These bubble collisions can produce GWs and thus open up the possibility of measuring signals from dark sectors which are not detectable by any of the conventional experiments. In the next chapter the GW production from bubble collisions in a first order PT is discussed.

To determine for which number of flavours n_f and quark masses m_i QCD-like theories exhibit which type of transition one generally has to do lattice calculations. However, in the limits $m_i \to 0$ and $m_i \to \infty$ the nature of the phase transition can be determined to be first order based on general arguments using universality classes. See e.g. refs. [46, 47].

For $n_f = 2 + 1$ [2] the type of phase transition as function of m_i can be summarized in the Columbia plot (see fig. 2.1), named after the university where the seminal work on the QCD phase transition was done [45]. Although in recent years many more sophisticated lattice calculations have been performed [46], the general characteristics as

[2] $n_f = 2 + 1$ means that two quarks are degenerate in mass, whereas the third quark can have a different mass, this is to good approximation true for the physical masses of the three lightest quarks in QCD.

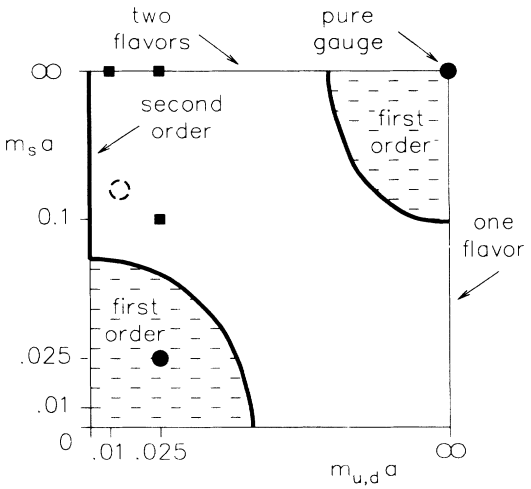

FIGURE 2.1: Columbia plot for three quark flavours, taken from ref. [45].

shown in fig. 2.1 are still the same. More precise calculations using lattice QCD have shown that due to the finite masses of the quarks, as measured for QCD, the transition is in fact a crossover [46].

QCD-like theories can thus exhibit different types of transitions, depending on the number of quarks and the size of the quark masses. For massless QCD-like sectors it is known that the PT must be first order for $n_f > 2$ [45], thus possibly allowing for the production of a significant gravitational wave signal. In order to characterize the PT in a QCD-like dark sector further we will need to find the effective potential. However, due to the non-perturbative nature of strongly coupled theories this is impossible within the conventional perturbative expansion of QFT. To circumvent this problem we will be using low-energy effective models. The following sections we will discuss the NJL model, the PNJL model and the LSM. We will be looking specifically at QCD-like dark sectors with $n_f = 3$.

The idea of all these effective models is that they are constructed such that they observe the same symmetries and symmetry breaking patterns as the full theory. We will later show how the parameters of the effective models can be selected in such a way that the observables are the same for each model.

2.2 Nambu-Jona-Lasinio model

In this section we closely follow the review from S.P. Klevansky [48, 49]. The NJL model was first proposed by Y. Nambu and G. Jona-Lasinio in the 60s as a model to describe nucleon interactions [50, 51], however it can be reformulated to describe quark interactions within QCD. The Lagrangian of the NJL model is not derived from first

principles but postulated such that it respects all the global symmetries of the complete theory. Although the NJL model does describe the quark degrees of freedom it does not describe the gluon interactions. Confinement is therefore not incorporated in the NJL model. Given the global symmetries of a SU(N) gauge theory with n_f flavours as summarized in eq. (2.6), one possible choice for an effective Lagrangian respecting all these symmetries is the following [23, 48]:

$$\mathcal{L}_{\text{NJL}} = \text{Tr}\,\bar{q}i\partial\!\!\!/ q + 2G\,\text{Tr}(\Psi^\dagger\Psi) + G_D(\det\Psi + h.c.) \qquad \text{with} \qquad (\Psi)_{ij} = \bar{q}_i(1-\gamma_5)q_j\ . \tag{2.7}$$

Here q corresponds to the (hidden) quarks and Ψ is a fermion bi-linear. The flavour indices i, j run from $i, j = 1 \ldots n_f$. The colour indices are again implicit. Note that we are looking at the chiral limit of the theories, such that the quarks do not have an explicit mass term.

The first term of this Lagrangian is the standard kinetic term for massless quarks. The second term encompasses the interaction term between four quarks. The last term is the 't Hooft determinant which is put in to break the $\text{U}(1)_A$ symmetry explicitly and thus take into account the quantum corrections. For a theory with three flavours the 't Hooft determinant corresponds to a 6-fermion interaction. Note that the Lagrangian is clearly non-renormalizable, since the mass-dimension of the interaction terms is larger than four. This non-renormalizability is however not surprising, nor concerning, since the aim of these effective QCD-like models is to describe the theory at low energies. The non-renormalizability of the NJL model just shows that at high temperatures the correct description of the physics is given by QCD.

To show that indeed this Lagrangian respects all the global symmetries of the full theory and that $\text{U}(1)_A$ is explicitly broken by the 't Hooft determinant we will use the transformations as defined in eqs. (2.4) and (2.5). Again the kinetic term trivially respects all global symmetries. To determine if the other terms respect the global symmetry group $\mathcal{G}'$ we first need to determine how the bi-linear Ψ transforms. To find the transformation of Ψ under $\text{SU}(n_f)_L$ and $\text{SU}(n_f)_R$ it is convenient to write Ψ in terms of the chiral fields; $\Psi_{ij} = \bar{q}_{Rj}q_{Li}$.

Using eqs. (2.4) and (2.5), it is straightforward to see that Ψ transforms as:

$$\begin{aligned} &\Psi \to U_L\Psi U_R^\dagger && \text{under } \text{SU}(3)_L \times \text{SU}(3)_R\ , \\ &\Psi \to \Psi e^{2i\vartheta_5\gamma_5} && \text{under } \text{U}(1)_A\ , \\ &\Psi \to \Psi && \text{under } \text{U}(1)_V\ . \end{aligned} \tag{2.8}$$

The unitarity of U_L and U_R implies that $U_{L/R}^\dagger U_{L/R} = I$, which will ensure that $\Psi^\dagger\Psi$ is invariant under $\text{SU}(3)_L \times \text{SU}(3)_R$. Moreover, $\Psi^\dagger\Psi$ also remains invariant under both

U(1) symmetries. The situation for the 't Hooft determinant is slightly more complicated; Clearly this term is invariant under $U(1)_V$, since unitary matrices have the property that their determinant is equal to one the 't Hooft determinant also respects $SU(3)_L \times SU(3)_R$. The axial symmetry is however explicitly broken by $U(1)_A$, as desired.

The low energy effective NJL model as described by the Lagrangian in eq. (2.7) thus respects exactly the same symmetries as the underlying QCD-like theory.

2.2.1 Mean Field Approximation

The Lagrangian in eq. (2.7) is not yet in a form which can be used to derive the effective potentials and investigate the possible PTs within this model. To work towards a useful Lagrangian we employ the so called Mean Field Approximation (MFA) [49, 52], which loosely speaking means we split up the Lagrangian in an interacting part, which we subsequently ignore, and a mean field term, by expanding the Lagrangian around the expectation value $\langle \Psi \rangle$. The mean field Lagrangian can then be used to derive the effective potential.

The split is achieved by expanding the Lagrangian around the expectation value, which can be defined as:

$$\langle \Psi \rangle = -\frac{1}{4G}\left((\sigma + i\eta')I + 2(a_a + i\pi_a)T^a\right) \ , \tag{2.9}$$

with

$$\sigma = -\frac{4G}{3}\langle \bar{q}q \rangle \ , \quad \pi_a = -4\mathrm{i}G\langle \bar{q}\gamma_5 T_a q \rangle \ , \quad \eta' = -\frac{4\mathrm{i}G}{3}\langle \bar{q}\gamma_5 q \rangle \ , \quad a_a = -4G\langle \bar{q}T_a q \rangle \ . \tag{2.10}$$

These fields correspond to the physical mesons of the theory and a runs from $1 \ldots 8$. Note that all these fields are 3×3 matrices in flavour space. When the quark masses are degenerate there is no mixing between π_0 (the η' meson) and π_8.

Expanding the bi-linear around the vacuum expectation value as:

$$\Psi = \langle \Psi \rangle + : \Psi : \ , \tag{2.11}$$

we can also determine how $\Psi^\dagger \Psi$ is expanded:

$$\begin{aligned} \Psi^\dagger \Psi &= (\langle \Psi \rangle + : \Psi :)^2 && (2.12)\\ &= \langle \Psi \rangle^2 + 2\langle \Psi \rangle : \Psi : + : \Psi :^2 && (2.13)\\ &= -\langle \Psi \rangle^2 + 2\langle \Psi \rangle \Psi + : \Psi :^2 \ , && (2.14) \end{aligned}$$

where in the last line we have put back : $\Psi := \Psi - \langle\Psi\rangle$ such that we get a mean field term which is at most linear in the fermion bi-linear Ψ.

By expanding the bi-linear around the expectation value it is thus possible to split the Lagrangian into a part which only contains terms which are at most linear in Ψ, i.e. quadratic in the fermion, and a part which contains the interaction terms:

$$\mathcal{L}_{\text{NJL}} = \mathcal{L}_{\text{MFA}} + \mathcal{L}_{\text{int}} \,. \tag{2.15}$$

Following the above steps and using the Cayley-Hamilton theorem to expand the determinant of a 3×3 matrix: $\det\Psi = \frac{1}{3}\operatorname{Tr}(\Psi^3) - \frac{1}{2}\operatorname{Tr}(\Psi^2)\operatorname{Tr}(\Psi) + \frac{1}{6}(\operatorname{Tr}(\Psi))^3$ it is possible to derive the MFA Lagrangian:

$$\begin{aligned}\mathcal{L}^{\text{MFA}}_{\text{NJL}} = {} & \operatorname{Tr}\bar{q}(\mathrm{i}\partial\!\!\!/ - M)q - \mathrm{i}\operatorname{Tr}(\bar{q}\gamma_5\pi q) - \mathrm{i}\operatorname{Tr}(\bar{q}\gamma_5\eta' q) - \operatorname{Tr}(\bar{q}aq) \\ & + \frac{G_D}{8G^2}\Big[(\pi_a\pi_a - a_a a_a - \eta'^2)\operatorname{Tr}(\bar{q}q) - \operatorname{Tr}(\bar{q}\pi^2 q) + \operatorname{Tr}(\bar{q}a^2 q) \\ & + \operatorname{Tr}(\bar{q}\eta'\pi q) + \mathrm{i}\operatorname{Tr}(\bar{q}\gamma_5\sigma\pi q) - 2\mathrm{i}\operatorname{Tr}(\bar{q}\gamma_5\pi a q) + \mathrm{i}\operatorname{Tr}(\bar{q}\gamma_5\eta' a q) - \operatorname{Tr}(\bar{q}\sigma a q) \\ & + \mathrm{i}(3a_a\pi_a - 2\sigma\eta')\operatorname{Tr}(\bar{q}\gamma_5 q)\Big] - V^{\text{tree}}_{\text{NJL}} \,.\end{aligned} \tag{2.16}$$

The flavour indices a are implicitly summed over from $a = 1 \ldots 8$. And π and a are defined as $\pi := 2\pi_a T_a$ and $a := 2a_a T_a$. The effective fermion mass M is defined as:

$$M = \sigma - \frac{G_D}{8G^2}\sigma^2 \,. \tag{2.17}$$

And the tree-level potential $V^{\text{tree}}_{\text{NJL}}$ is

$$V^{\text{tree}}_{\text{NJL}} = \frac{1}{8G}\left(3\sigma^2 + 3\eta'^2 + 2\pi_a\pi_a + 2a_a a_a\right) - \frac{G_D}{16G^3}\left[\sigma\left(\sigma^2 + \pi_a\pi_a - 3\eta'^2 - a_a a_a\right) + 5a_a\pi_a\eta'\right] \,. \tag{2.18}$$

Note that this Lagrangian gives the same tree-level mass to each of the three quark flavours. Since we left out explicit masses and the model consequently has a Z_3 symmetry, this is to be expected. In the presence of a degenerate explicit quark mass m the effective mass becomes $M = m + \sigma - \frac{G_D}{8G^2}\sigma^2$.

2.2.2 Effective Potential

Having obtained the Lagrangian in the Mean Field Approximation, $\mathcal{L}_{\text{MFA}}$, it is now possible to derive the effective potential. The NJL effective potential will be determined in a loop expansion, up to and including the one-loop effects. Because the vacuum needs

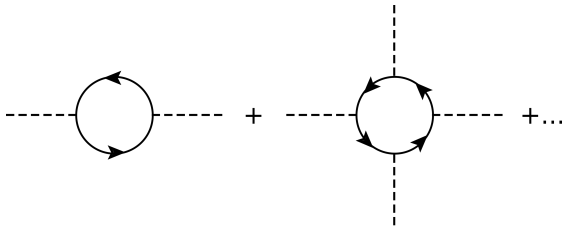

FIGURE 2.2: Terms contributing to the one-loop effective potential.

to be parity even and the quarks are degenerate and thus respect a Z_3 symmetry in the chiral limit, for which all quarks are massless, the only meson field which is able to obtain a vacuum expectation value is the σ meson. The effective potential describing the phase transition thus only needs to contain all the terms depending on σ. To determine the one-loop contribution we need to realize that only the quarks can run in the loop because the mesons are non-propagating at tree-level, i.e. they don't have kinetic terms. The effective potential is thus given by a tree level term V_0^{NJL} and loop contributions from the fermions running in the loop;

$$V_{\text{EFF}}^{\text{NJL}} = V_0^{\text{NJL}} + V_{\text{loop}} \,. \tag{2.19}$$

At tree level the effective potential can simply be determined from eq. (2.18) as,

$$V_0^{\text{NJL}} = \frac{3}{8G}\sigma^2 - \frac{G_D}{16G^3}\sigma^3 \,. \tag{2.20}$$

As mentioned, the loop-level terms in the potential are obtained by integrating out the fermions. The one-loop contribution to the effective potential is given by the Coleman-Weinberg term [20, 53], for $\mathcal{L} \sim \bar{q}Mq$ it is given as:

$$\begin{aligned} V_{\text{loop}} &= i \int \frac{\mathrm{d}^4 p}{(2\pi)^4} \sum_{n=1}^{\infty} 4 n_c n_f \left(\frac{M^2}{p^2}\right)^n \frac{1}{2n}(-1) \\ &= 2 i n_c n_f \int \frac{\mathrm{d}^4 p}{(2\pi)^4} \log\left(1 - \frac{M^2}{p^2}\right) \,. \end{aligned} \tag{2.21}$$

Here we have already taken the trace over Dirac indices and summed over flavour and colour indices. Diagrammatically this equation is equivalent to summing over the class of Feynman diagrams as shown in fig. 2.2. In this figure the external lines are given by the field M and the internal lines are the (massless) quarks. In our case only the diagrams with an even number of external legs will contribute, because the trace over an uneven number of gamma matrices is zero.

Following ref. [53] and using similar techniques as for determining the thermal scalar mass (see appendix A), the loop contribution to the effective potential can be split up

in a temperature independent part, $V_{\rm CW}^{\rm NJL}$, and a temperature dependent term $V_{\rm FT}^{\rm NJL}$.

Note that the temperature independent part of eq. (2.21) is divergent. For our purposes the NJL model is being treated as an effective low-energy theory with an explicit cut-off, therefore we will employ an explicit 4D Euclidean cut-off Λ to regularize this integral [3],

$$\begin{aligned} V_{\rm CW}^{\rm NJL}(\sigma) &= -2n_c n_f \frac{1}{8\pi^2}\int_0^\Lambda \mathrm{d}p_E p_E^3 \log\left(1+\frac{p_E^2}{M^2}\right) \\ &= -\frac{n_c n_f}{16\pi^2}\left[M^2\Lambda^2+\Lambda^4\log\left(1+\frac{M^2}{\Lambda^2}\right)-M^4\log\left(1+\frac{\Lambda^2}{M^2}\right)\right] . \end{aligned} \tag{2.22}$$

At finite temperature, using the imaginary time formalism, the integral in eq. (2.21) can be written as:

$$V_{\rm loop} = -2n_c n_f T\sum_n \int \frac{\mathrm{d}^3 p_E}{(2\pi)^3}\log\left(1+\frac{M^2}{p_E^2+\omega_n^2}\right) , \tag{2.23}$$

where the sum is over the Matsubara frequencies, see appendix A, and p_E is the momentum. Using similar techniques as those employed in appendix A to determine thermal masses, the temperature dependent part of this equations gives,

$$V_{\rm FT}^{\rm NJL}(\sigma) = \frac{2n_c n_f T^4}{\pi^2} J_F(M/T) , \tag{2.24}$$

with $J_F(r) = -\int_0^\infty \mathrm{d}x\, x^2 \log\left(1+\mathrm{e}^{-\sqrt{x^2+r^2}}\right)$, $r = M/T$ and $x = p_E/T$.

Combining everything we obtain the following effective potential for the NJL model

$$\begin{aligned} V_{\rm EFF}^{\rm NJL} = &+\frac{3}{8G}\sigma^2 - \frac{G_D}{16G^3}\sigma^3 \\ &-\frac{3n_c}{16\pi^2}\left[\Lambda^4\log\left(1+\frac{M^2}{\Lambda^2}\right)-M^4\log\left(1+\frac{\Lambda^2}{M^2}\right)+\Lambda^2M^2\right] \\ &+\frac{2n_c n_f T^4}{\pi^2}J_F(M/T) . \end{aligned} \tag{2.25}$$

2.2.3 Phase diagram

Since only first order phase transitions occur through the production of bubbles, gravitational waves are only produced in this type of phase transition. To determine the nature of the phase transition the global minimum of $V_{\rm NJL}(\sigma)$ as a function of the temperature needs to be determined. It is possible to do this calculation for zero as well as non-zero (but degenerate) quark masses. The results are shown in fig. 2.3, where the

[3] Note that other regularization schemes can also be used, see ref. [54] for a discussion on this.

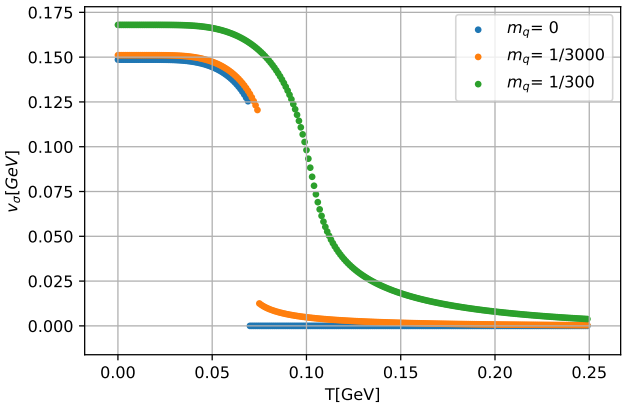

FIGURE 2.3: Phase transition in the NJL model for several values of the (degenerate) quark mass. Using BP A as defined in table 4.1.

global minimum v_σ is shown as a function of T for several values of the degenerate quark mass m_q.

Figure 2.3 shows that for zero quark mass the transition is indeed discontinuous, i.e. first order, while for larger quark masses the transition becomes crossover or second order. This result agrees with the general behaviour of the Columbia plot shown in fig. 2.1. We thus see that qualitatively the NJL model has the same symmetry breaking behaviour as QCD. This is to be expected since the fact that the phase transition of chiral models with more than two flavours is first order is based on general symmetry arguments; both massless QCD and the NJL respect the same symmetries, thus the phase transition should be of the same type. The same holds for the other effective models.

2.2.4 Meson masses

In order to compare the NJL model with other effective models we need to determine the observables predicted by the effective models. For the NJL model the observables are given by the masses of the mesons m_σ, m_π, m_η and m_a. To determine the masses of these mesons the (zero temperature) propagators need to be determined. This is done by taking into account all the one-loop contributions to the propagator, while keeping in mind that only the fermions, not the mesons, propagate in the loop. As an example the diagrams contributing to the σ propagator are shown in fig. 2.4.

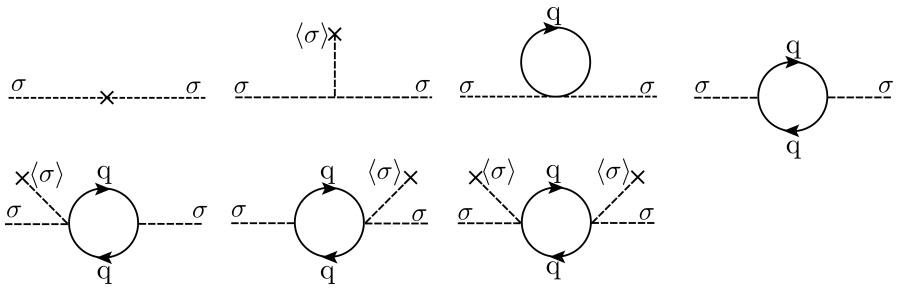

FIGURE 2.4: Feynman diagrams contributing to the one-loop propagator of the σ meson.

Calculating these diagrams the propagator for each meson can be determined:

$$\Gamma_{\sigma\sigma}(p^2, v_\sigma) = -\frac{3}{4G} + \frac{3G_D v_\sigma}{8G^3} - \left(1 - \frac{G_D v_\sigma}{4G^2}\right)^2 3n_c I_S(p^2, v_\sigma) + \frac{G_D}{G^2} 3n_c I_V(v_\sigma)\,, \quad (2.26a)$$

$$\Gamma_{\pi\pi}(p^2, v_\sigma) = -\frac{1}{2G} + \frac{G_D v_\sigma}{8G^3} + \left(1 - \frac{G_D v_\sigma}{8G^2}\right)^2 2n_c I_P(p^2, v_\sigma) + \frac{G_D}{G^2} n_c I_V(v_\sigma)\,, \quad (2.26b)$$

$$\Gamma_{\eta'\eta'}(p^2, v_\sigma) = -\frac{3}{4G} - \frac{3G_D v_\sigma}{8G^3} + \left(1 + \frac{G_D v_\sigma}{4G^2}\right)^2 3n_c I_P(p^2, v_\sigma) - \frac{G_D}{G^2} 3n_c I_V(v_\sigma)\,, \quad (2.26c)$$

$$\Gamma_{aa}(p^2, v_\sigma) = -\frac{1}{2G} - \frac{G_D v_\sigma}{8G^3} - \left(1 + \frac{G_D v_\sigma}{8G^2}\right)^2 2n_c I_S(p^2, v_\sigma) - \frac{G_D}{G^2} n_c I_V(v_\sigma)\,. \quad (2.26d)$$

With the integrals defined as,

$$I_V(v_\sigma) = \int \frac{\mathrm{d}^4 k}{\mathrm{i}(2\pi)^4} \frac{M_c}{k^2 - M_c^2}\,, \quad (2.27a)$$

$$I_S(p^2, v_\sigma) = \int \frac{\mathrm{d}^4 k}{\mathrm{i}(2\pi)^4} \frac{\mathrm{Tr}[(\not{k} + \not{p} + M_c)(\not{k} + M_c)]}{((k+p)^2 - M_c^2)(k^2 - M_c^2)}\,, \quad (2.27b)$$

$$I_P(p^2, v_\sigma) = \int \frac{\mathrm{d}^4 k}{\mathrm{i}(2\pi)^4} \frac{\mathrm{Tr}[(\not{k} + \not{p} + M_c)\gamma_5(\not{k} + M_c)\gamma_5]}{((k+p)^2 - M_c^2)(k^2 - M_c^2)}\,. \quad (2.27c)$$

$M_c = M(v_\sigma)$ is the constituent quark mass at the true minimum. For the purpose of finding the zero temperature masses, these integrals are calculated using an explicit 4D Euclidean cut-off Λ. The effective masses are then determined from the root of the (zero-temperature) propagators;

$$\Gamma(p^2)\big|_{p^2=m^2} = 0\,, \quad (2.28)$$

where v_σ is the vacuum expectation value of the field σ at zero temperature, which can be found from the effective potential, as depicted in fig. 2.3

The mass spectrum of the mesons was determined for Benchmark Point A, as defined in table 4.1; i.e. $\Lambda = 0.93$ GeV, $G_D = -90.65$ GeV^{-5}, $G = 3.84$ GeV^{-2} and $m_q = 0$ GeV. To check the consistency of the NJL model the mass spectrum is also determined for a

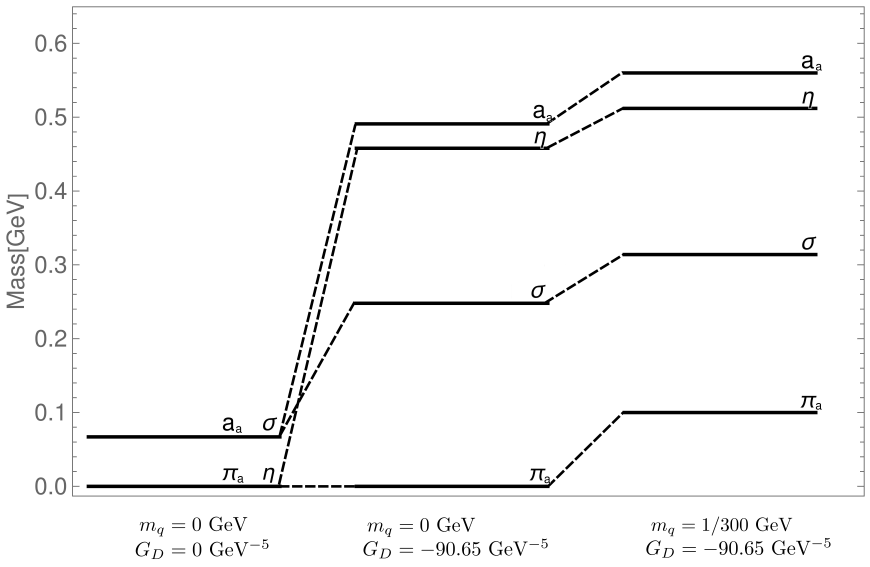

FIGURE 2.5: The effect of the 't Hooft determinant and explicit quark masses on the mass spectrum of the (pseudo)scalar mesons.

theory in which the 't Hooft determinant is zero; $G_D = 0$ and for a theory with non-zero but degenerate quark masses; $m_q = 1/300$ GeV. Whereas $G_D = 0$ corresponds to unbroken axial U(1)$_A$ symmetry, non-zero quark masses correspond to a theory with explicitly broken chiral symmetry. The results are shown in fig. 2.5. Here the index a runs from $a = 1 \ldots 8$.

This meson spectrum is qualitatively as expected; For unbroken U(1)$_A$ the scalar and pseudoscalar nonet are degenerate in mass, additionally the pseudoscalars are massless due to their Goldstone boson nature. Furthermore, U(1)$_A$ breaking through a non-zero 't Hooft determinant splits the nonets into octets and singlets, where the pseudoscalar octet (pions) are the massless Goldstone bosons. When an explicit (degenerate) mass term is added to the model the pions become pseudo Goldstone bosons and thus obtain a small but non-zero mass. Note that the addition of a degenerate quark mass, as opposed to a non-degenerate quark mass, ensures that the masses of both octets remain degenerate. When the u, d and s quark have different masses, as seen in QCD, both octets will split. See for example ref. [55] for more details on meson spectra. Note that in the chiral limit the NJL model has two free parameters which together fix four masses.

2.2.5 Wave function Renormalization, σ propagation

The last quantity needed to determine the dynamics of the phase transition is the wave function renormalization of the meson σ. This is necessary because we need σ to tunnel from the false vacuum into the real vacuum (first order phase transition) [56]. At tree level the field σ is not dynamical due to its composite nature and therefore can not tunnel. To obtain a dynamical meson we will need to look at the loop diagrams and determine the wave function renormalization (Z_σ^{-1}). The kinetic term for σ is then given by,

$$\mathcal{L} \supset Z_\sigma^{-1}(\partial\sigma)^2 \,. \tag{2.29}$$

The wave function renormalization is defined as [56]:

$$Z_\sigma^{-1} = \frac{d}{dp^2}\Gamma_{\sigma\sigma}(p^2,\sigma)\bigg|_{p^2=0} \,. \tag{2.30}$$

Note that for an elementary particle Z_σ^{-1} is equal to one at tree level.

The one-loop σ propagator, $\Gamma_{\sigma\sigma}(p^2,\sigma)$, was already defined in eq. (2.26) to determine the meson mass. Using this propagator the wave function renormalization can be determined as [1]:

$$Z_\sigma^{-1}(\sigma) = -3n_c\left(1-\frac{G_D}{4G^2}\sigma\right)^2\left[-2A_0+2B_0+8C_0-2\ell_A(r)+2\ell_B(r)+8\ell_C(r)\right] \,, \tag{2.31}$$

with $r \equiv r(\sigma) = |M(\sigma)|/T$ and

$$\begin{aligned} A_0 &= \frac{1}{16\pi^2}\left[\log\left(1+\frac{\Lambda^2}{M^2}\right)-\frac{\Lambda^2}{\Lambda^2+M^2}\right] \,, \\ B_0 &= -\frac{1}{32\pi^2}\frac{\Lambda^4}{(M^2+\Lambda^2)^2} \,, \\ C_0 &= \frac{1}{96\pi^2}\frac{3M^2\Lambda^4+\Lambda^6}{(M^2+\Lambda^2)^3} \,. \end{aligned}$$

The thermal integrals $\ell_I(r)$ are determined to be

$$\ell_A(r) = -\frac{1}{4\pi^2}\int_0^\infty \mathrm{d}x \left(\frac{x^2}{\sqrt{x^2+r^2}^3}\frac{1}{1+\exp\sqrt{x^2+r^2}} + \frac{1}{2}\frac{x^2}{(\sqrt{x^2+r^2})^2}\frac{1}{1+\cosh\sqrt{x^2+r^2}}\right), \tag{2.32}$$

$$\ell_B(r) = \frac{r^2}{16\pi^2}\int_0^\infty \mathrm{d}x \left(\frac{3x^2}{\sqrt{x^2+r^2}^5}\frac{1}{1+\exp\sqrt{x^2+r^2}} + \frac{3x^2}{2(\sqrt{x^2+r^2})^4}\frac{1}{1+\cosh\sqrt{x^2+r^2}} + \frac{x^2}{2(\sqrt{x^2+r^2})^5}\frac{1}{1+\cosh\sqrt{x^2+r^2}}\right), \tag{2.33}$$

$$\ell_C(r) = -\frac{r^4}{96\pi^2}\int_0^\infty \mathrm{d}x \left(\frac{15x^2}{\sqrt{x^2+r^2}^7}\frac{1}{1+\exp\sqrt{x^2+r^2}} + \frac{15x^2}{2(\sqrt{x^2+r^2})^6}\frac{1}{1+\cosh\sqrt{x^2+r^2}} + \frac{3x^2}{(\sqrt{x^2+r^2})^5}\frac{\tanh(\sqrt{r^2+x^2}/2)}{1+\cosh\sqrt{x^2+r^2}} + \frac{x^2}{2(\sqrt{x^2+r^2})^4}\frac{1}{1+\cosh\sqrt{x^2+r^2}} - \frac{3x^2}{2(\sqrt{x^2+r^2})^4}\frac{1}{(1+\cosh\sqrt{x^2+r^2})^2}\right). \tag{2.34}$$

Note that these rather lengthy expression are the result of calculating the integrals in eq. (2.27) at *finite* temperature, with explicit 4D Euclidean cut-off Λ for the zero temperature part. The temperature dependent integrals are determined within the imaginary time formalism, see e.g. ref. [57] for a review on thermal quantum field theory.

Having derived the effective potential, meson masses and the wave function renormalization of σ, we now have all necessary ingredients to determine the phase transition dynamics of the NJL model. This will be the topic of the coming chapters, first two more effective models of QCD-like theories will be discussed.

2.3 Polyakov Extended NJL

Whereas the NJL model describes the effective dynamics of mesons and quarks, it does not contain gluons and is therefore not able to describe the (de)confinement PT which is expected to take place in QCD-like theories. From QCD it is known that the chiral and (de)confinement PT occur at similar temperatures [58], therefore the inclusion of gluon effects might have an important effect on the χPT. The problem of how to incorporate gluon effects into the effective potential was discussed some decades ago by Fukushima [59], he showed that gluon effects can be put explicitly into the effective potential by using the expectation value of the Polyakov loop, denoted as L [59, 60]. A review on the Polyakov loop can be found in e.g. ref. [58]. The effective gluon potential

which can be formed with the Polyakov loop is not derived from first principles but is phenomenological; its parameters are determined from for example lattice calculations.

There are many possible choices for the gluon potential, which are all approximately equivalent for temperatures up to the critical temperature of the (de)confinement phase transition [61]. Following ref. [60] the Polyakov potential is chosen as:

$$T^{-4}V_{\text{glue}}(L,T) = -\tfrac{1}{2}a(T)L\bar{L} + b(T)\log\left[1 - 6L\bar{L} - 3(L\bar{L})^2 + 4(L^3 + \bar{L}^3)\right] , \qquad (2.35)$$

with

$$a(T) = a_0 + a_1\frac{T_{\text{glue}}}{T} + a_2\left(\frac{T_{\text{glue}}}{T}\right)^2 \qquad \text{and} \qquad b(T) = b_3\left(\frac{T_{\text{glue}}}{T}\right)^3 . \qquad (2.36)$$

Here L is the order parameter, which is equivalent to the expectation value of the Polyakov loop. Due to the logarithmic term in the potential L is limited to lie between $L = 0$ and $L = 1$. This potential can be further simplified by the fact that we are assuming the chemical potentials to be equal to zero, thus $L = \bar{L}$ [58].

The parameters a_i and b_3 in eq. (2.36) can be determined by lattice QCD calculations, in ref. [60] they are stated to be:

$$a_0 = 3.51 , \qquad a_1 = -2.47 , \qquad a_2 = 15.2 , \qquad b_3 = -1.75 . \qquad (2.37)$$

The last unknown parameter of the gluon potential is T_{glue}, the critical temperature of the (de)confinement PT. The value of T_{glue} can be determined from lattice calculations. In the pure gauge limit, where quarks are assumed to be infinitely heavy, $T_{\text{glue}} = 270$ MeV, while the presence of finite-mass quarks reduces T_{glue} to 178 MeV[62].

The (de)confinement phase transition described by the gluon potential corresponds to a transition between a confined phase at low temperatures and a deconfined phase at higher temperature, with $\langle L\rangle = 0$ and $\langle L\rangle \neq 0$, respectively. By determining the minimum of L as a function of the temperature T the phase transition can be quantified, this is shown in fig. 2.6. The figure shows that the gluon potential exhibits a first order phase transition; with the critical temperature given by T_{glue}. This first order nature of the (de)confinement phase transition is only true in the case of a pure gluonic model, i.e. infinitely heavy or absent quarks. In ref. [63] lattice calculations with the inclusion of (light) quarks predict that the transition in this case is no longer first order but becomes a crossover.

The gluon potential in itself does not couple to the quarks and mesons and would therefore not affect the χPT. Following ref. [58] the interaction between gluons and quarks is taken into account in the temperature dependent term of the NJL effective

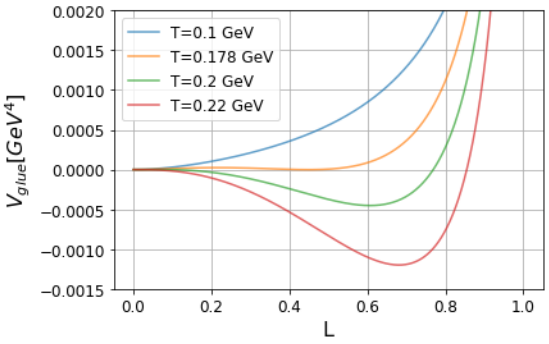

FIGURE 2.6: Gluon potential in terms of the Polyakov loop for multiple temperatures. Note that T_{glue} corresponds to the critical temperature, i.e. the potential shown by the yellow line.

potential eq. (2.25) as follows:

$$V_{\text{FT}}^{\text{NJL}} = -\frac{2n_c n_f T^4}{\pi^2}\int_0^\infty \mathrm{d}x x^2 \log\left(1+\mathrm{e}^{-\sqrt{x^2+r^2}}\right) \tag{2.38}$$

$$\to -\frac{2n_f T^4}{\pi^2}\int_0^\infty \mathrm{d}x\, x^2 \log\left(1+\mathrm{e}^{-3\sqrt{x^2+r^2}}+3L\mathrm{e}^{-\sqrt{x^2+r^2}}+3L\mathrm{e}^{-2\sqrt{x^2+r^2}}\right) = V_{\text{FT}}^{\text{PNJL}} \tag{2.39}$$

Note that at high temperature $\langle L\rangle \to 1$, thus, the interaction term reduces to that of the NJL model, i.e. $\log(1+3x+3x^2+x^3) = 3\log(1+x)$, with the factor of 3 being the number of colours. Thus in the limit $T\to\infty$ the dynamics of the PNJL and NJL model are the same, the gluon potential itself does not affect the sigma dynamics without an interaction term. At zero temperature both models are also equivalent, since the finite temperature loop contributions do not contribute at zero temperature.

The tree level and Coleman-Weinberg term of the effective potential as derived for the NJL model eq. (2.25) remain the same. Combining everything the effective potential of the PNJL is given as:

$$\begin{aligned} V_{\text{EFF}}^{\text{PNJL}} =& V_0^{\text{NJL}} + V_{\text{CW}}^{\text{NJL}} + V_{\text{FT}}^{\text{PNJL}} + V_{\text{glue}} \\ =& +\frac{3}{8G}\sigma^2 - \frac{G_D}{16G^3}\sigma^3 \\ & -\frac{3n_c}{16\pi^2}\left[\Lambda^4\log\left(1+\frac{M^2}{\Lambda^2}\right) - M^4\log\left(1+\frac{\Lambda^2}{M^2}\right) + \Lambda^2M^2\right] \\ & -\frac{2n_f T^4}{\pi^2}\int_0^\infty \mathrm{d}x\, x^2\log\left(1+\mathrm{e}^{-3\sqrt{x^2+r^2}}+3L\mathrm{e}^{-\sqrt{x^2+r^2}}+3L\mathrm{e}^{-2\sqrt{x^2+r^2}}\right) \\ & +T^4\left(-\tfrac{1}{2}a(T)L^2 + b(T)\log\left[1-6L^2-3L^4+8L^3\right]\right) . \end{aligned} \tag{2.40}$$

The above potential contains two fields, σ and L. In order to use the standard (one-field) tunnelling formalism, as discussed in the following chapter, the potential needs to be

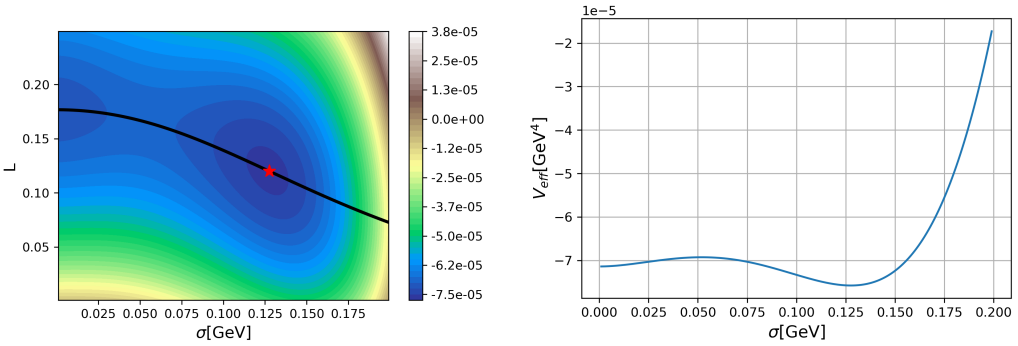

FIGURE 2.7: On the left the effective potential, $V_{\text{eff}}[\,\text{GeV}^4]$ as a function of $\sigma[\,\text{GeV}]$ and L. The black line corresponds to $L = L_{\text{min}}$ and the red star indicates the true minimum. On the right the potential along this line is shown. For BPA, as defined in table 4.2, with $T = 0.12$ GeV.

reduced such that it only depends on one field. Thus we need to put in an assumption for the Polyakov loop L. As discussed, L undergoes a crossover transition in the presence of light quarks. It is therefore reasonable to assume that L will simply follow its minimum during the transition, thus becoming a function of σ and T. Mathematically we determine L by minimizing $V_{\text{EFF}}^{\text{PNJL}}$ for each T and σ, i.e. $L \to L_{\text{min}}(\sigma, T))$.

In the left plot of fig. 2.7 the potential at $T = 0.12\,\text{GeV}$ is shown as a function of σ and L, in this plot $L_{min}(\sigma)$ is also depicted. The effective potential which is used to determined the dynamics of the first order phase transition is defined along this line. This potential is shown in the right figure of fig. 2.7, note that even with the inclusion of the gluon dynamics the chiral phase transition remains first order, as seen by the bump separating the two minima.

With the substitution $L \to L_{\text{min}} = L_{\text{min}}(\sigma, T)$ we have thus obtained a one dimensional effective potential which can be used to determine the dynamics of the first order phase transition and the strength of the gravitational wave signals. This will be discussed in chapters 3 and 4. Note that in ref. [64] a similar, but slightly less sophisticated choice of $L_{min}(\sigma, T)$ was used.

The observables, i.e. the masses and the pion decay constant, are determined at zero temperature and will thus not be affected by the inclusion of the Polyakov loop; they will be equal to those determined in the NJL model. Furthermore, it is assumed that the effect of the Polyakov loop on the wave-function renormalization can be neglected, thus Z_σ^{-1} as derived for the NJL model will also be used in the PNJL model.

The derivation of all relevant elements needed to determine the dynamics of the phase transition is now completed for both the NJL and PNJL model. As a last model the Linear Sigma Model will be discussed.

2.4 Linear Sigma Model

The Linear Sigma Model (LSM) was first introduced by Gell-Mann in the 60s in ref. [65]. Like the (P)NJL model the aim of the LSM is to describe non-perturbative behaviour of strongly coupled theories like QCD. Whereas the (P)NJL model contains quark degrees of freedom and the PNJL additionally contains the gluon dynamics, the LSM only describes scalar degrees of freedom, i.e. the mesons. The Lagrangian of the LSM is, like the (P)NJL Lagrangian, chosen such that it respects the same symmetries as the full theory. As mentioned before the symmetry group of massless QCD, with $n_f = 3$, is given by $\mathrm{SU}(3)_V \times \mathrm{SU}(3)_A \times \mathrm{U}(1)_V$. A general renormalizable Lagrangian respecting this symmetry group is:

$$\mathcal{L}_{\mathrm{LSM}} = \mathrm{Tr}\,\partial_\mu \Phi^\dagger \partial^\mu \Phi - V_{\mathrm{tree}}^{\mathrm{LSM}}(\Phi)\,, \tag{2.41}$$

with $V_{\mathrm{tree}}^{\mathrm{LSM}}(\Phi)$ defined as [66]:

$$\begin{aligned} V_{\mathrm{tree}}^{\mathrm{LSM}}(\Phi) = & -m^2\,\mathrm{Tr}(\Phi^\dagger\Phi) + \tfrac{1}{2}(\lambda_\sigma - \lambda_a)\big(\mathrm{Tr}(\Phi^\dagger\Phi)\big)^2 + \tfrac{3}{2}\lambda_a\,\mathrm{Tr}\big((\Phi^\dagger\Phi)^2\big) \\ & - \sqrt{\tfrac{2}{3}}\,c\big(\det\Phi + \det\Phi^\dagger\big)\,. \end{aligned} \tag{2.42}$$

The meson field Φ is a complex scalar field, given by a 3×3 matrix

$$\Phi = \frac{1}{\sqrt{6}}(\sigma + \, i\eta')I + (a_a + \mathrm{i}\pi_a)\,T^a\,. \tag{2.43}$$

with a again running from $1 \ldots 8$ and T_a are the reduced Gell-Mann matrices as defined below eq. (2.1). The LSM thus describes the same meson fields as the (P)NJL; the scalars σ and a_a and the pseudoscalars η' and π_a.

Following the same reasoning as for the NJL Lagrangian, it is clear that, apart from the determinant, this Lagrangian is invariant under $\mathrm{U}(3)_L \times \mathrm{U}(3)_R$. Similar to the determinant in the (P)NJL the determinant in this Lagrangian explicitly breaks the axial symmetry, $\mathrm{U}(1)_A$. Due to spontaneous symmetry breaking the scalar σ will obtain a vacuum expectation value v_σ from the chiral phase transition. As explained before the other mesons will not obtain a vacuum expectation value.

2.4.1 Effective Potential

To determine the dynamics of the phase transition we again derive the effective potential at finite temperature. The tree level effective potential $V_0(\bar{\sigma})$ can be determined

from the LSM potential, eq. (2.42), by expanding the potential around $\Phi = \frac{1}{\sqrt{6}}\bar{\sigma}$;

$$V_0(\bar{\sigma}) = -\frac{1}{2}m^2\bar{\sigma}^2 + \frac{1}{8}\bar{\sigma}^4 - \frac{1}{9}c\bar{\sigma}^3 \,, \tag{2.44}$$

with $\bar{\sigma}$ the classical field of the σ meson.

Due to infrared divergences standard perturbation theory unfortunately breaks down and thus can not be used to reliably determine the loop level contributions to the effective potential [67]. It is however possible to deal with these divergences by resummation techniques. In the following the Cornwall-Jackiw-Tomboulis (CJT) formalism [68] will be used to re-sum specific classes of diagrams and thus alleviate the problem of infrared divergences. This formalism was extended to be applicable at finite temperature in for example refs. [69–71]. Furthermore, in refs. [72–75] the CJT formalism has been applied to the LSM to determine the effective potential. A short summary of this formalism for a single scalar field is given in appendix B. The extension of this formalism to multiple scalars is straightforward.

Following appendix B and the papers mentioned above, the CJT formalism within the Hartree-Fock approximation [76, 77] gives the following effective potential:

$$V_{\text{EFF}}^{\text{LSM}} = V_0(\bar{\sigma}) + V_{\text{FT}}^{\text{LSM}}(\bar{\sigma}, T) \tag{2.45a}$$

$$= V_0(\bar{\sigma}) + \frac{T^4}{2\pi^2}\sum_i g_i \left[J_{\text{B}}(R_i^2) - \tfrac{1}{4}(R_i^2 - r_i^2) I_{\text{B}}(R_i^2) \right] \,, \tag{2.45b}$$

with $V_0(\bar{\sigma})$ defined in eq. (2.44). We have defined $r_i \equiv r_i(\bar{\sigma}, T) = m_i(\bar{\sigma})/T$ and $R_i \equiv R_i(\bar{\sigma}, T) = M_i(\bar{\sigma}, T)/T$. The sum runs over all the mesons; the scalars σ and a and the pseudoscalars π and η. With $g_i = 1$ and $g_i = 8$ for respectively the singlet and the octet (pseudo)scalars. The thermal integrals J_B and I_B are defined as:

$$J_B(r^2) = +\int_0^\infty \mathrm{d}x\, x^2 \log\left(1 - \mathrm{e}^{-\sqrt{x^2+r^2}}\right) \,, \tag{2.46a}$$

$$I_B(r^2) = 2\,\frac{\mathrm{d}J_B(r^2)}{\mathrm{d}r^2} = \int_0^\infty \mathrm{d}x \frac{x^2}{\sqrt{x^2+r^2}} \frac{1}{\mathrm{e}^{\sqrt{x^2+r^2}} - 1} \,. \tag{2.46b}$$

Note that one-loop zero temperature contributions to the effective potential are neglected, in [73, 74] it was shown that this does not impact the results qualitatively. In these equations m_i correspond to the tree level masses of the mesons, whereas M_i are the effective temperature dependent masses. The thermal masses of the mesons are determined self-consistently via so called fixed-point equations. Within the CJT formalism, using the Hartree-Fock approximation [76, 77], these fixed point equations are

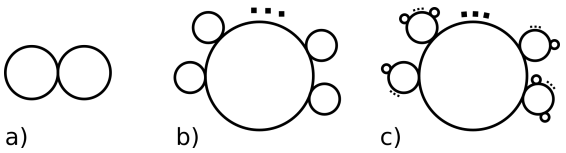

FIGURE 2.8: a) the double bubble diagram. b) the class of Daisy diagrams. c) the class of super-daisy diagrams.

given as:

$$M_\sigma^2(\bar{\sigma}) = m_\sigma^2(\bar{\sigma}) + \frac{T^2}{4\pi^2}\Big[3\lambda_\sigma I_{\text{B}}(R_\sigma^2) + 8(\lambda_\sigma + 2\lambda_a) I_{\text{B}}(R_a^2) + \lambda_\sigma I_{\text{B}}(R_{\eta'}^2) + 8\lambda_\sigma I_{\text{B}}(R_\pi^2)\Big]\,, \tag{2.47a}$$

$$\begin{aligned} M_a^2(\bar{\sigma}) = m_a^2(\bar{\sigma}) + \frac{T^2}{4\pi^2}\Big[&(\lambda_\sigma + 2\lambda_a) I_{\text{B}}(R_\sigma^2) + 5(2\lambda_\sigma + \lambda_a) I_{\text{B}}(R_a^2) \\ &+ \lambda_\sigma I_{\text{B}}(R_{\eta'}^2) + (8\lambda_\sigma + 9\lambda_a) I_{\text{B}}(R_\pi^2)\Big]\,, \end{aligned} \tag{2.47b}$$

$$M_{\eta'}^2(\bar{\sigma}) = m_{\eta'}^2(\bar{\sigma}) + \frac{T^2}{4\pi^2}\Big[3\lambda_\sigma I_{\text{B}}(R_{\eta'}^2) + 8(\lambda_\sigma + 2\lambda_a) I_{\text{B}}(R_\pi^2) + \lambda_\sigma I_{\text{B}}(R_\sigma^2) + 8\lambda_\sigma I_{\text{B}}(R_a^2)\Big]\,, \tag{2.47c}$$

$$\begin{aligned} M_\pi^2(\bar{\sigma}) = m_\pi^2(\bar{\sigma}) + \frac{T^2}{4\pi^2}\Big[&(\lambda_\sigma + 2\lambda_a) I_{\text{B}}(R_{\eta'}^2) + 5(2\lambda_\sigma + \lambda_a) I_{\text{B}}(R_\pi^2) \\ &+ \lambda_\sigma I_{\text{B}}(R_\sigma^2) + (8\lambda_\sigma + 9\lambda_a) I_{\text{B}}(R_a^2)\Big]\,, \end{aligned} \tag{2.47d}$$

with m_i the zero temperature masses of the mesons. Solving these fixed point equations we can determine $M \equiv M(\bar{\sigma}, T)$, thus resulting in a well defined effective potential.

Note that this effective potential only required the calculation of one type of diagram, namely the *double bubble diagram*. However due to resummation, i.e. inserting the full propagator instead of the tree level propagator and determining the full propagator self consistently using the gap equation, the effective potential automatically includes an infinite set of daisy and super-daisy diagrams [69]; without explicitly calculating these. Examples of daisy and super-daisy diagrams as well as the double bubble diagram are shown in fig. 2.8.

2.4.2 Observables

The observables we are interested in are the meson masses and the pion decay constant. The zero temperature masses of the mesons can be determined from the tree level potential eq. (2.42) using

$$m_\alpha^2 = \frac{\partial^2 V}{\partial \alpha^2}|_{\Phi = \frac{1}{\sqrt{6}}\bar{\sigma} I}\,. \tag{2.48}$$

Here we again assume only σ will obtain a vacuum expectation value. From the tree level LSM potential as defined in eq. (2.42), the following masses for the mesons can be derived:

$$m_\pi^2(\bar{\sigma}) = -m^2 - \tfrac{1}{3}c\bar{\sigma} + \tfrac{1}{2}\lambda_\sigma\bar{\sigma}^2 \,, \tag{2.49a}$$

$$m_{\eta'}^2(\bar{\sigma}) = m_\pi^2(\bar{\sigma}) + c\bar{\sigma} \,, \tag{2.49b}$$

$$m_\sigma^2(\bar{\sigma}) = m_\pi^2(\bar{\sigma}) - \tfrac{1}{3}c\bar{\sigma} + \lambda_\sigma\bar{\sigma}^2 \,, \tag{2.49c}$$

$$m_a^2(\bar{\sigma}) = m_\pi^2(\bar{\sigma}) + \tfrac{2}{3}c\bar{\sigma} + \lambda_a\bar{\sigma}^2 \,. \tag{2.49d}$$

The pion decay constant is related to the vacuum expectation value of $\bar{\sigma}$ as [66]:

$$v_\sigma = \sqrt{\frac{3}{2}}\, f_\pi \,. \tag{2.50}$$

In the chiral limit the Linear Sigma Model thus has four observables; m_σ, $m_{\eta'}$, m_a and f_π. Note that m_π is automatically zero in the chiral limit, no tuning of parameters is required. The LSM Lagrangian also has four free parameters λ_σ, λ_a, c, m^2, therefore, contrary to the (P)NJL model, each mass can be tuned individually by setting the parameters to specific values. As we will see later this will be crucial in order to compare the three effective models.

We have thus derived the effective potential for all three effective models. In the next chapter we will see how the effective potential can be used to investigate the dynamics of the phase transition and the gravitational wave production.

Chapter 3

Gravitational wave production from PTs in the early universe

Already in 1918, soon after the development of the theory of General Relativity (GR) in 1915 [5, 78], it was shown that the existence of gravitational waves is predicted by General Relativity [79]. GWs can be visualized as waves or ripples moving through spacetime which alternately stretch and contract spacetime. They are expected to be produced during violent events, meaning events with strong gravitational interactions, like the merger of black holes and/or neutron stars, but also during first order phase transitions (see e.g. ref. [80] for a recent review). Whereas a binary merger constitutes one single event coming from a specific source, the signal from a phase transitions is a stochastic signal, i.e. a signal which does not come from a resolvable source. This stochastic background is in general much harder to detect.

In each of the processes mentioned above the gravitational waves are produced either in the early universe and/or at a large distance from the earth. Due to the generic redshift from the expansion of the universe gravitational wave signals from these processes, as measured on earth, are thus rather weak. Direct detection of gravitational waves on earth is consequently extremely hard. However, since several decades there have been indirect hints from astrophysical measurements that strongly suggest that a binary inspiral indeed produces gravitational waves [81, 82]. It was shown that the binary first discovered in 1974 [81] and closely followed in the years afterwards, slowly looses energy, causing the two stars of the binary to move closer together [82]. Eventually over a long time the stars are expected to merge. The most straightforward way to explain this energy loss is through the emission of gravitational waves [82]. Precise calculations on the expected energy loss from gravitational wave emission in this binary, when compared to decades of precise measurement on the binary orbit have shown

that the theory of General Relativity is able to explain the binary inspiral remarkably well [83].

Finally in 2016, almost exactly 100 years after the first prediction of gravitational waves, they were for the first time directly observed when the LIGO and VIRGO collaboration managed to detect gravitational wave signals from a black hole merger [7]. In recent years the LIGO and VIRGO collaboration have measured many more black hole binary mergers as well as neutron star mergers [84–86]. These measurements allow for all kinds of interesting research on astrophysics and also offer a unique way of testing General Relativity in the limit of strong interaction [7]. Note that the gravitational wave signals from the first measured black hole merger corresponds to a physical length difference of about 10^{-18} m [87]: these signals are thus indeed extremely weak.

Unlike gravitational wave signals from binary mergers, a stochastic gravitational wave signal from a first order phase transition (PT) has not (yet) been detected. These signals would be interesting for multiple reasons; first of all they would likely point to new physics, after all the Standard Model is not expected to undergo any first order phase transition. Secondly, gravitational waves are produced in the early universe and thus describe physics at large energy scales, they therefore offer a channel complementary to standard collider searches, which are in general much more limited in the energy scale of new physics they can investigate. In the case of strongly coupled QCD-like dark sectors, which are not, or only very weakly, interacting with the Standard Model particles, gravitational wave signals might very well be one of the only signals one could expect to observe in the near future.

Although it will likely still be some decades before experiments are able to detect gravitational waves from first order phase transitions, if these even exist and are strong enough, it is in the meantime interesting to determine for Standard Model (SM) extensions what the possible GW signals would be. The goal of this type of research is two-fold; it helps set sensitivity targets for (future) experiments while it at the same time, once experimental results begin to emerge, will help to constrain SM extensions. The aim of this chapter is to show how the GW signals from a first order phase transition can be determined. In the following chapter this will be applied to the effective low-energy QCD-like models, which were discussed in chapter 2.

The remainder of this chapter is organized as follows; We will start with explaining the different quantities which are relevant for the PT dynamics. A discussion on how these can be derived or estimated from the effective potential and the Lagrangian will also be included. Following this, the three main production mechanisms of GWs (bubble collisions, soundwaves and turbulence) will be discussed. Formulas for calculating

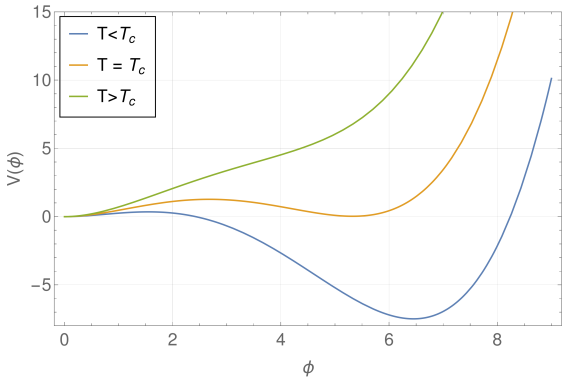

FIGURE 3.1: Potential for several temperature, exhibiting a first order phase transition. T_c is the critical temperature.

the energy density of each of these contributions will be given. To conclude the chapter some current and future GW experiments and their (proposed) sensitivities will be discussed. Reviews on this topic, which we will closely follow in this chapter, are for example refs. [25, 28].

3.1 Quantifying the PT dynamics

A first order PT occurs through the nucleation of bubbles as follows; In the early universe, for which the temperature is larger than some critical temperature T_c the universe is in the symmetric phase; there is no bubble nucleation. However, once the universe starts cooling down the effective potential can develop a second minimum, at the critical temperature T_c these minima have the same energy. Note that for a first order phase transition these minima are separated by a barrier, which causes the field to remain temporarily stuck in the old (false) vacuum. Quantum fluctuations and/or thermal fluctuations will subsequently push small patches of the universe into the new (true) vacuum. These bubbles of true vacuum will then expand and collide with each other. The phase transition is complete when the bubbles have filled the universe. An example of how a generic potential exhibiting a first order phase transition evolves from high to low temperature is shown in fig. 3.1.

Due to their approximate spherical symmetry neither the bubbles themself nor their expansion produces gravitational waves, however, the collisions of these bubbles *will* result in the production of gravitational waves [88]. If strong enough, these gravitational wave signals could in principle be measured by detectors on earth like LIGO and VIRGO [89, 90] or proposed space-based detectors like eLISA [28]. The expected signal from a first order phase transition can be characterized by a finite set of macroscopic quantities [28]:

- α, a measure of the relative energy released during the transition, i.e. the energy difference between the false and true vacuum;
- T_n, the nucleation temperature, i.e. the temperature at which bubble nucleation becomes efficient;
- β/H, a measure of the duration of the phase transition;
- v_w, the terminal velocity of the bubble wall.

Below each of these quantities will be discussed. Their meaning will be explained and we will describe how they can be determined from the effective potential.

3.1.1 Released energy

The most straightforward of these quantities is α. This quantity can be defined in several ways, depending on how one exactly defines the energy released during the transition [25]. We will here discuss the two definitions mainly encountered in the literature: α defined through the latent heat and α defined through the trace of the energy momentum tensor. Note that α is always normalized to the energy density outside the bubbles, i.e. the energy density in the symmetric phase.

Defining α through the latent heat gives (see e.g. [24]),

$$\alpha_L := \frac{1}{\rho_{\text{rad}}(T_n)} \left(\Delta V_{\text{eff}}(T_n) - T_n \left. \frac{\partial \Delta V_{\text{eff}}(T)}{\partial T} \right|_{T=T_n} \right) . \tag{3.1}$$

On the other hand defining α through the trace of the energy momentum tensor gives [91, 92],

$$\alpha_T := \frac{1}{\rho_{\text{rad}}(T_n)} \left(\Delta V_{\text{eff}}(T_n) - \frac{1}{4} T_n \left. \frac{\partial \Delta V_{\text{eff}}(T)}{\partial T} \right|_{T=T_n} \right) . \tag{3.2}$$

In these equations $\Delta V_{\text{eff}}(T) := V_{\text{eff}}(0,T) - V_{\text{eff}}(\bar{\sigma}_{\text{min}}(T),T)$ and $\bar{\sigma}_{\text{min}}(T)$ is the true minimum of the potential for a given temperature. V_{eff} is the effective potential of the theory. Furthermore, $\rho_{\text{rad}} = \frac{\pi^2}{30} g_\star T^4$ is the energy density of a radiation dominated universe and $g_\star$ is the number of degrees of freedom in the symmetric, high temperature phase. For our QCD-like model the degrees of freedom are determined by the three quarks with each four polarizations and three colours and the eight massless gluons with two polarizations each, i.e.,

$$g_\star = \frac{7}{8} \sum_f n_f + \sum_b n_b = 7/8 \times 4 \times 3 \times 3 + 2 \times 8 = 47.5 . \tag{3.3}$$

Note that α is related to the *strength* of the phase transition, the more energy released during a phase transition the stronger the phase transition will be. In case of strong phase transitions in which the universe remains stuck in the false vacuum long after the critical temperature we have $\Delta V_{\text{eff}} \gg T_n(\partial \Delta V_{\text{eff}}(T)/\partial T)$. In this regime, generally called supercooling, both definitions of α are equivalent. Strong phase transitions are characterized by $\alpha \gg 1$.

In the following chapter it will be shown that in general the chiral phase transitions of our effective models are weak first order, i.e. $\alpha \leq 1$. Therefore, a definition of α needs to be chosen. The choice of α will affect definitions of quantities discussed later, thus in order to remain consistent with definition of other quantities we follow the definition as given in ref. [91] and define α through the energy momentum tensor, i.e. $\alpha := \alpha_T$.

Given the effective potentials of the (P)NJL model and the LSM, which can be found in respectively eqs. (2.25), (2.40), (2.44) and (2.45), α can thus be straightforwardly determined once σ_{min} and T_n are known. While σ_{min} can be determined by minimizing each effective potential, the nucleation temperature T_n requires the determination of the bubble nucleation rate Γ, which will be the topic of the next section.

3.1.2 Bubble nucleation rate

The effective potential and bubble nucleation dynamics are characterized by two temperatures, T_n and T_c, which are in general not equal. The critical temperature T_c is the temperature at which both minima are equal, i.e. the true and false minimum have the same energy, and can easily be determined by plotting the effective potential as a function of the temperature. Right below T_c bubbles will begin to nucleate. At some point the temperature will be small enough that bubble nucleation becomes efficient. This temperature is defined as T_n. Mathematically this condition is defined as the temperature at which one bubble per (4D) Hubble volume is produced [93],

$$\int_{T_n}^{T_c} \frac{\mathrm{d}T}{T} \frac{\Gamma(T)}{H(T)^4} \stackrel{!}{=} 1 \,, \tag{3.4}$$

where $\Gamma(T)$ is the bubble nucleation rate at finite temperature. Once this condition is full-filled, bubbles will be produced faster than the Hubble expansion can drive them apart, the relative space occupied by bubbles will therefore start to increase and the phase transition will soon after be completed. In general T_n is also the temperature at which the gravitational waves will be produced [28]. Note that in case of supercooling and subsequent reheating one needs to be careful with the equality [93]. This will however not be an issue for the weak first order phase transitions present in our

effective models. Equation (3.4) can be simplified by realizing that in general, for non-supercooled PTs, the integral is dominated by contributions at $T = T_n$. Thus, the nucleation temperature can to good approximated be determined from [93],

$$\Gamma(T_n) \stackrel{!}{=} H(T_n)^4 \,, \tag{3.5}$$

with the Hubble constant,

$$H^2(T) = \frac{\rho_{\text{rad}}(T)}{3M_{\text{Pl}}^2} \,, \tag{3.6}$$

and the Planck mass, $M_{\text{Pl}} = 2.435 \times 10^{21}$ MeV. Note that this definition of the Hubble constant is only valid for a radiation dominated universe.

At zero temperature the bubble nucleation rate, i.e. the tunnelling probability per unit time and unit volume, is defined as [94, 95]:

$$\Gamma = A \exp(-S_4(\phi)) \,, \tag{3.7}$$

with $S_4(\phi)$ the 4 dimensional Euclidean action. Which for a general scalar field ϕ is given by,

$$S_4(\phi) = \int \mathrm{d}^4x \left[\frac{1}{2} \left(\frac{\mathrm{d}\phi}{\mathrm{d}t} \right)^2 + \frac{1}{2} (\nabla\phi)^2 + V_{\text{eff}}(\phi) \right] \,. \tag{3.8}$$

The nucleation rate Γ can then be found by minimizing the Euclidean action $S_4(\phi)$ and substituting this into the definition of Γ. Assuming $O(4)$ symmetry and working in spherical coordinates this corresponds to solving the differential equation

$$\frac{\partial^2\phi}{\partial r^2} + \frac{3}{r}\frac{\partial\phi}{\partial r} - \frac{\partial V_{\text{eff}}}{\partial\phi} = 0 \,, \tag{3.9}$$

with boundary condition,

$$\phi(r)|_{r\to\infty} \to 0 \quad \text{and} \quad \left.\frac{\mathrm{d}\phi}{\mathrm{d}r}\right|_{r=0} = 0 \,. \tag{3.10}$$

Note that for zero temperature the transition from the false to the true vacuum occurs via quantum tunnelling.

We are however interested in the dynamics of the field at *finite* temperature, in this case temperature fluctuations will play a dominant role in transitioning the field from the false to the true vacuum [95]. At high temperatures the 4D Euclidean action will be replaced by the 3D action S_3 [95] which is defined as,

$$S_3[\phi] = \int \mathrm{d}^3x \left(\frac{1}{2}\partial_i\phi\partial^i\phi + V(\phi) \right) = \int \mathrm{d}\Omega \mathrm{d}r\, r^2 \left[\frac{1}{2} \left(\frac{\mathrm{d}\phi}{\mathrm{d}r} \right)^2 + V(\phi) \right] \,, \tag{3.11}$$

with the nucleation rate defined as [94],

$$\Gamma(T) \simeq T^4 \left(\frac{S_3[\phi]}{2\pi^2 T}\right)^{\frac{3}{2}} \exp(-S_3[\phi]/T) \,. \tag{3.12}$$

Similar to the zero temperature case the nucleation rate is determined by minimizing the action $S_3[\phi]$ and substituting this into the equation for $\Gamma(T)$. Again assuming spherical symmetry the $S_3[\phi]$ is minimized by the following equation of motion,

$$\frac{\partial^2\phi}{\partial r^2} + \frac{2}{r}\frac{\partial\phi}{\partial r} - \frac{\partial V}{\partial\phi} = 0 \,. \tag{3.13}$$

The boundary conditions are the same as those defined for the zero temperature case, see eq. (3.10). The solution of this equation of motion will be defined as $\phi_0(r)$.

The equation of motion as defined in eq. (3.13) can be used to describe bubble nucleation in the LSM, with the effective potential V_{eff} defined in eq. (2.45). Note that the field ϕ needs to be substituted by $\bar{\sigma}$. However, as discussed, the scalar σ in the (P)NJL model has a composite nature, consequently the kinetic term of the scalar field is not present at tree level. It is thus necessary to add the wave function renormalization to the Lagrangian. This results in a slightly changed equation of motion as compared to eq. (3.11),

$$\frac{\mathrm{d}^2\bar{\sigma}}{\mathrm{d}r^2} + \frac{2}{r}\frac{\mathrm{d}\bar{\sigma}}{\mathrm{d}r} - \frac{1}{2}\frac{\partial \log Z_\sigma}{\partial\bar{\sigma}}\left(\frac{\mathrm{d}\bar{\sigma}}{\mathrm{d}r}\right)^2 = Z_\sigma \frac{\partial V_{\text{eff}}}{\partial\bar{\sigma}} \,. \tag{3.14}$$

The same boundary conditions again apply. With V_{eff} given by eq. (2.25) and eq. (2.40) for the NJL and PNJL model, respectively. The wave function renormalization Z_σ is for both models defined in eq. (2.31).

Although a solution of this equation of motion can in general not be found analytically, it is possible to find in numerically. In the next section we will discuss how this equation of motion can be solved numerically to determine the minimum of the action $S_3[\phi]$, which we will define as $S_3[\phi_0]$.

Given the solution for the equation of motion, $S_3[\phi_0]$, the bubble nucleation rate can be determined. Combining eqs. (3.4), (3.6) and (3.12) the nucleation temperature is found by solving,

$$\left.\frac{S_3[\phi_0]}{T}\right|_{T=T_n} = 2\log\left(\frac{90}{g_*\pi^2}\frac{M_{Pl}^2}{T_n^2}\right) \,. \tag{3.15}$$

For weak phase transitions, as is the case for the transitions in our effective models, $T_n \sim T_c$. This equation can therefore be simplified by setting $T_n = T_c$ in the right-hand side of this equation.

From $S_3[\phi_0]$ it is thus possible to find the nucleation temperature T_n and once T_n is known α can be determined. The third quantity related to the bubble nucleation, β/H, which is a measure for the speed of the phase transition, can also be determined straightforwardly once $S_3[\phi_0]$ and T_n are derived. β is defined as [28],

$$\beta = H(T_n)T_n \cdot \left.\frac{\mathrm{d}(S_3(\phi_0)/T)}{\mathrm{d}T}\right|_{T=T_n} . \tag{3.16}$$

3.1.3 Velocity of the bubble wall

The last quantity relevant for the production of gravitational waves is the bubble wall velocity, v_w. Naively one can understand its importance by thinking about the bubble wall velocity as an energy contained in the bubbles. When bubbles collide, a large wall velocity will naively correspond to more gravitational wave production.

Unfortunately the bubble wall velocity is the least well understood of the four quantities discussed here. The terminal velocity the bubble wall reaches when expanding is strongly related to the interaction of the particles undergoing the phase transition with the plasma. One can in general distinguish two separate cases, runaway and non-runaway. In case of a scalar field which does not couple to the plasma the bubbles formed during the first order phase transition will be able to expand without any friction. This results in so called runaway bubbles for which the bubble wall velocity will very quickly reach the speed of light, $v_w \to 1$. On the other hand, a field which is strongly coupled to a plasma will have an expanding bubble wall which encounters a large amount of friction from the plasma, thus resulting in a wall velocity which reaches a terminal value $v_w \leq 1$ [28]. In this scenario the bubbles are called non-runaway.

To deal with the uncertainty in the bubble wall velocity we will in the next chapter determine the gravitational wave spectra for a range of bubble wall velocities, namely, $0.75 < v_w < 1$.

3.2 Solving the equations of motions

In the following we will discuss how eq. (3.11), but also eq. (3.14), can be solved to minimize $S_3[\phi]$ and find $\phi_0(r)$. The solution of the equations of motion, $\phi_0(r)$, describes a bubble profile; inside the bubble, at small r, the field is in the true vacuum, whereas outside the bubble the field value takes the value of the false vacuum. Below we will show explicitly how the equation of motion for an elementary particle, eq. (3.11), can be

solved. The extension of this method to solving the equation of motion of a composit field, eq. (3.14), is straightforward.

The equation of motion, eq. (3.11), shows that tunnelling from the false to the true vacuum is mathematically equivalent to the classical motion of a ball rolling down a potential $-V$ with the friction given by $\frac{2}{r}\frac{\partial\phi}{\partial r}$ [94, 96]. The friction term is the result of working in spherical coordinates. The boundary conditions then correspond to an initial position at which the velocity is zero and a final position exactly 'on top' of the false vacuum. Continuing this equivalence one can see that the parameter r is analogous to a time variable, while the field ϕ acts as a 1D position variable x. Note that the inversion of the potential is the result of changing from Minkowski to Euclidean space. The equation of motion can in principle also be generalized for ϕ consisting of multiple fields, see e.g. ref. [96], however for our purposes it is sufficient to describe the tunnelling of a single scalar field.

To solve the equation of motion for a field ϕ and determine the bubble profile $\phi_0(r)$ which minimizes the action $S_3[\phi]$ the Python package CosmoTransitions [96] is used. For the (P)NJL, the package was slightly adapted to allow for the changed equation of motion as defined in eq. (3.14). CosmoTransitions uses the overshoot/undershoot method (see e.g. [94]) to solve the equation of motion.

The overshoot/undershoot method works as follows; Given a potential $-V(\phi)$, as depicted in fig. 3.2, the boundary conditions correspond to the field having zero 'velocity', i.e. $\frac{\mathrm{d}\phi}{\mathrm{d}r} = 0$, at some initial point close to the true vacuum and to the field reaching the false vacuum for $r \to \infty$. To determine the tunnelling solution, i.e. the true bubble profile, we need to find the initial position $\phi(r = 0)$ such that at the end of the evolution the field has exactly reached the false vacuum, i.e. $\phi(r \to \infty) \to 0$. In general one can always find a value of $\phi(r = 0)$ for which the field roles down too fast, causing it to overshoot the false vacuum. The opposite case in which the field roles down so slow that it gets stuck in the minimum can also generally be found. This is called undershooting. Consequently there must be a *unique* point for which the field roles down with exactly the correct speed such that it ends up at the false vacuum with zero velocity. This corresponds to the true solution of the equation of motion $\phi_0(r)$. Within CosmoTransitions this point is determined by varying the initial position till the true solution is found up to some finite accuracy. In the right plot of fig. 3.2 the true solution and an example of an undershoot and overshoot bubble profile are shown. We note that the friction term results in the damped oscillation observed in the bubble profile of the undershoot solution.

Furthermore, note that for small $S_3[\phi_0]/T$ the bubble nucleation rate is large, while for large $S_3[\phi_0]/T$ the bubble nucleation rate is exponentially suppressed. For $T = T_c$ the

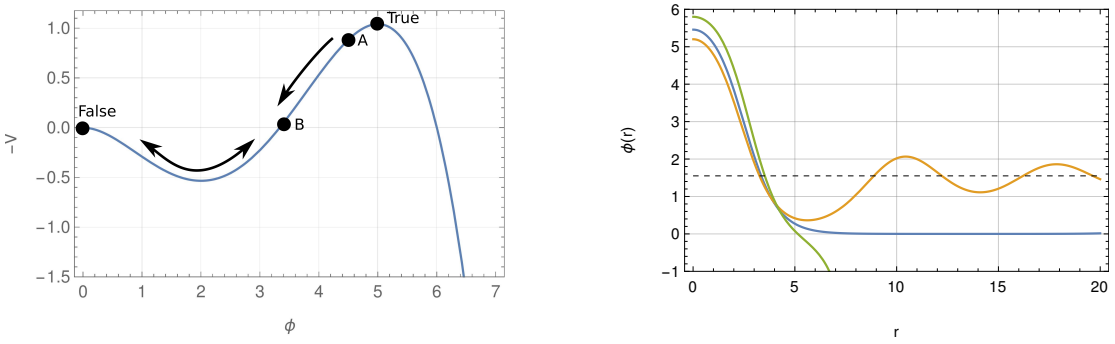

FIGURE 3.2: On the left the inverted potential plus two points corresponding to approximately overshoot (A) and undershoot (B). On the right we have the bounce solution for overshoot(green), undershoot(orange) and the true solution(blue)

true bubble profile $\phi_0(r)$ will give $S_3[\phi_0] \to \infty$. Which corresponds to the fact that when the true and false minimum have the same energy tunnelling will take infinitely long, i.e. there is no bubble nucleation at the critical temperature ($\Gamma(T_c) \to 0$). For smaller temperatures $T < T_c$ the energy difference between the two minima in general increases, thus increasing the bubble nucleation rate.

3.3 Contributions to the gravitational wave spectrum

Having introduced the four quantities describing a first order phase transition, we can now use them to determine the energy density of the gravitational waves produced during a first order phase transition.

The gravitational wave spectrum is not derived from first principles but determined numerically using large-scale simulations. With these simulations approximate formulas for the energy density of the gravitational wave signal have been determined, see e.g. ref. [97]. These formulas require the input of the four quantities discussed above.

There are three main processes which contribute to the gravitational wave production (see e.g. ref. [28]); bubble wall collisions, soundwaves and magnetohydrodynamic turbulence. The total gravitational wave signal is given as the sum of each of these processes,

$$h^2\Omega_{GW} \simeq h^2\Omega_{\text{coll}} + h^2\Omega_{\text{sw}} + h^2\Omega_{\text{turb}} \,. \tag{3.17}$$

Depending on the quantities α, β/H, T_n and v_w one or more of these contributions dominate. In the following each of these contributions will be discussed separately.

The contribution to the gravitational wave signals from bubble wall collisions can be approximated using the so called envelop approximation. From large scale simulations

this contribution is determined to be (see e.g. [28]),

$$\Omega_{\text{coll}}h^2(f) \approx 1.67 \times 10^{-5} \left(\frac{H}{\beta}\right)^2 \left(\frac{\kappa\alpha}{1+\alpha}\right)^2 \left(\frac{0.11 v_w^3}{0.42 + v_w^2}\right) \left(\frac{100}{g_\star}\right)^{1/3} S_{\text{env}}(f) \,, \quad (3.18)$$

with the spectral function $S_{\text{env}}(f)$,

$$S_{\text{env}}(f) = \frac{3.8\,(f/f_{\text{env}})^{2.8}}{1 + 2.8\,(f/f_{\text{env}})^{3.8}} \,. \quad (3.19)$$

The redshifted peak frequency f_{env} defined as,

$$f_{\text{env}} = 16.5 \times 10^{-3}\,\text{mHz}\, \frac{\beta}{H} \frac{f_\star}{\beta} \frac{T_n}{100\,\text{GeV}} \left(\frac{g_\star}{100}\right)^{1/6} \,, \quad (3.20)$$

and the peak frequency at the time the gravitational waves are produced, $f_\star$, is

$$\frac{f_\star}{\beta} = \frac{0.62}{1.8 - 0.1 v_w + v_w^2} \,. \quad (3.21)$$

Within the envelope approximation, see e.g. refs. [28, 98], the bubbles are approximated as a thin shell. It is assumed that after collisions between bubbles only the outer shells remain relevant, i.e. the *envelope*. The dynamics of the remnants of shells after their initial collision, which are contained within this envelope, are neglected.

The only unknown quantity in these equations is κ, which is the energy contributing to the bubble wall collisions as a fraction of the total energy produced during the phase transformation. For a runaway bubble the bubble wall velocity quickly reaches the speed of light. Therefore, almost all energy is contained in the bubble wall collisions and subsequently transformed into gravitational waves. In this scenario the bubble wall collisions will be the dominant contribution to the gravitational wave spectrum.

In case of a non-runaway bubble the friction of the bubble wall with the plasma will transfer a large fraction of its energy to the plasma. Consequently, contribution from soundwaves and turbulence are expected to be dominant and the contribution from collisions is expected to be negligible [28]. Note that, contrary to the contribution from bubble walls, the gravitational wave production from soundwaves as well as turbulence are processes taking place in the plasma, so called bulk motion. Both of these contributions are known less well, but can also be determined reasonably well with large scale simulations. The gravitational wave spectra for each of these contributions

are determined to be [28],

$$\Omega_{\rm sw}h^2(f) \approx 2.65\times10^{-6}\left(\frac{H}{\beta}\right)\left(\frac{\kappa_v\alpha}{1+\alpha}\right)^2\left(\frac{100}{g_\star}\right)^{1/3} v_w S_{\rm sw}(f)\,, \tag{3.22}$$

$$\Omega_{\rm turb}h^2(f) \approx 3.35\times10^{-4}\left(\frac{H}{\beta}\right)\left(\frac{\kappa_{\rm turb}\alpha}{1+\alpha}\right)^{3/2}\left(\frac{100}{g_\star}\right)^{1/3} v_w S_{\rm turb}(f)\,, \tag{3.23}$$

with the spectral functions $S_{\rm sw}$ and $S_{\rm turb}$,

$$S_{\rm sw}(f) = \left(\frac{f}{f_{\rm sw}}\right)^3\left(\frac{7}{4+3\,(f/f_{\rm sw})^2}\right)^{7/2}\,, \tag{3.24}$$

$$S_{\rm turb}(f) = \frac{(f/f_{\rm turb})^3}{(1+f/f_{\rm turb})^{11/3}\,(1+8\pi f/h_\star)}\,. \tag{3.25}$$

The frequencies are defined as,

$$f_{\rm turb} = 2.7\times10^{-2}\,{\rm mHz}\,\frac{1}{v_b}\frac{\beta}{H}\frac{T_n}{100{\rm GeV}}\left(\frac{g_\star}{100}\right)^{1/6}\,, \tag{3.26}$$

$$f_{\rm sw} = 1.9\times10^{-2}\,{\rm mHz}\,\frac{1}{v_b}\frac{\beta}{H}\frac{T_n}{100{\rm GeV}}\left(\frac{g_\star}{100}\right)^{1/6}\,. \tag{3.27}$$

And $h_\star$, the reduced Hubble rate the time of the phase transition, is defined as,

$$h_\star = 16.5\times10^{-3}\,{\rm mHz}\,\left(\frac{T_n}{100GeV}\right)\left(\frac{g_\star}{100}\right)^{1/6}\,. \tag{3.28}$$

κ_v and $\kappa_{\rm turb}$ are the fractions of total energy going into respectively soundwaves and turbulence. In case of large bubble wall velocities, which do not runaway, κ_v can be estimated as [28],

$$\kappa_v = \frac{\alpha}{0.73+0.083\sqrt{\alpha}+\alpha}\,. \tag{3.29}$$

Following refs. [24, 28] the fraction of energy contained in turbulence is in general assumed to be small,

$$\kappa_{turb} = \epsilon\kappa_v, \quad \text{with} \quad \epsilon \approx 0.05\,. \tag{3.30}$$

Due to $\epsilon \ll 1$ it can in general be assumed that for non-runaway bubbles soundwaves will be the dominant contribution to the gravitational wave spectrum.

3.3.1 Fast transitions

The formulas for the soundwave contribution to the effective potential, as summarized above, are derived within large-scale simulations, they are therefore only valid in specific limits. Interpolation of these results to other cases is in principle not trivial. More

specifically, the equations for the gravitational wave contribution from soundwaves, as summarized above, are only valid for slow phase transitions, i.e. for transitions in which the soundwaves have enough time to produce the gravitational wave signals. This means that they are only valid for $\tau_{\rm sw} H > 1$ [99], with

$$\tau_{\rm sw} = (8\pi)^{\frac{1}{3}} \cdot \frac{\xi_w}{\overline{U}_f \beta} \,. \tag{3.31}$$

$\overline{U}_f$ is the root mean-square velocity of the plasma [24],

$$\overline{U}_f^2 = \frac{3}{\xi_w^3} \int_{c_s}^{\xi_w} \xi^2 \frac{v(\xi)^2}{1 - v(\xi)^2} \mathrm{d}\xi \,. \tag{3.32}$$

In this equation $v(\xi)$ is the velocity profile as a function of $\xi = r/t$, with r the distance from the centre of the bubble and t the time after nucleation. $c_s = \sqrt{1/3}$ is the speed of sound in a relativistic fluid. Following ref. [24] the velocity profile can be determined by solving the differential equation,

$$\begin{aligned} \frac{2v}{\xi} &= \frac{1 - \xi v}{1 - v^2} \left[\frac{1}{c_s^2} \frac{(\xi - v)}{(1 - \xi v)} - 1 \right] \partial_\xi v \,, \\ v(\xi_w) &= \frac{v_+ - v_-}{1 - v_+ v_-} \,. \end{aligned} \tag{3.33}$$

The boundary condition is determined by v_+ and v_-, which are respectively the plasma velocity in the symmetric phase and the broken phase with respect to the bubble wall velocity. In the case when the bubble wall moves faster then the sound speed we have $v_+ = \xi_w$. This situation is called detonation [91]. For detonation v_+ and v_- are related through,

$$v_+ = \frac{1}{1 + \alpha} \left[\left(\frac{v_-}{2} + \frac{1}{6 v_-} \right) + \sqrt{\left(\frac{v_-}{2} + \frac{1}{6 v_-} \right) + \alpha^2 + \frac{2}{3}\alpha - \frac{1}{3}} \right] \,. \tag{3.34}$$

Assuming the wall velocity reaches values close to the speed of light, i.e. the fluid outside of the bubbles moves into the bubble with $v_+ \sim 1$, v_- and $v(\xi_w)$ can be determined from eqs. (3.33) and (3.34). These can subsequently be used to solve eq. (3.33) to find the plasma velocity $\overline{U}_f$.

In the next chapter we will show that the first order phase transitions, as found in the effective models we are discussing, in general have large β/H, consequently, $\tau_{sw} H \sim \mathcal{O}(10^{-3})$. Thus, the phase transition completes before the soundwaves have had sufficient time to produce gravitational waves. Equation (3.22) is therefore expected to *overestimate* the produced gravitational wave signal. Following refs. [24, 92] this overestimation is taken into account by multiplying the energy density, as defined in eq. (3.22),

with an additional factor,

$$\Omega_{\rm sw}^{\rm fast} h^2 = \tau_{\rm sw} H \cdot \Omega_{\rm sw} h^2 \,. \tag{3.35}$$

Note that this reduction factor has not yet been determined within the actual simulations but is an estimate based on the reduction of the time the soundwaves have to produce gravitational waves. Large scale simulations in the case of $\tau_{\rm sw} H < 1$ are needed to get a better understanding of this effect.

For fast transitions the fraction of the energy which is stored in turbulent motion is expected to significantly increase, i.e. the estimate in eq. (3.30) likely underestimates the contribution of turbulence to the gravitational wave signal. Following ref. [92] this effect is taken into account by multiplying the energy density defined in eq. (3.23) by an extra factor,

$$\Omega_{\rm turb}^{\rm fast} h^2 = (1 - \tau_{\rm sw} H) \cdot \Omega_{\rm turb} h^2 \,. \tag{3.36}$$

Additionally $\epsilon = 1$ and thus $\kappa_{tb} = \kappa_v$.

In the next chapter we will show that due to the *reduction* of the soundwave contribution and the *increase* of the contribution from turbulence, both contributions now become comparable in size [1].

3.4 Gravitational wave experiments

Apart from some already operational experiments like LIGO and VIRGO [87] there are many proposed and/or planned experiments which aim to measure gravitational waves from both astrophysical sources as well as early cosmology. This includes signals from phase transitions in the early universe. See for example ref. [100] for a review. Without going into all the technical details we will give a short summary of some of these experiments with their main characteristics. The currently planned or operational gravitational wave experiments we will be discussing can in general be split into three groups: ground- and space-based interferometers and Pulsar Timing Arrays (PTAs). See ref. [100] for a more extensive review and details of experiments not mentioned here.

The best-known ground-based gravitational wave experiments are LIGO and VIRGO [87]. As mentioned, these are the two experiments which have been able to measure gravitational wave signals from binary black hole and neutron star mergers [86]. Both of these detectors are ground-based laser interferometer experiments, consisting out of two kilometre-scale perpendicular arms. Using strong lasers the distance between freely floating masses, i.e. test masses, at the end of each arm is precisely measured.

Thermal fluctuations are minimized by embedding the whole system in vacuum tubes. Gravitational waves will stretch and contract spacetime in perpendicular direction, thereby creating an, at least theoretically, measurable shift in the arm-lengths (see e.g. ref. [87]). Upgrades of both of these experiments are underway, called aLIGO and aVIRGO. Note that there are also plans for a so called *third-generation* ground-based interferometer, the Einstein Telescope [101, 102], unlike VIRGO and LIGO the Einstein telescope is planned to be underground, allowing for reduction in background noise. Furthermore, the Einstein telescope is planned to be triangular-shaped. Triangular-shaped detectors are an efficient way of measuring additional aspects of gravitational wave signals, like the for example the polarization, without the need to introduce multiple L-shaped detectors [102]. LISA and VIRGO as well as the Einstein Telescope are mainly sensitive in the $\sim$ 100Hz region, interesting for for example the binary mergers. Note that by using multiple L-shaped interferometers, located at different positions on earth, it is not only possible to measure gravitational wave signals, but it is also possible to pinpoint the source of these gravitational waves. Thus allowing for extremely interesting multi-messenger research by combining graviational wave signals with electromagnetic signals [85].

Additionally, there are multiple space-based experiments in various stages of research and development. The most notable of these is eLISA [37, 103, 104], which is planned to be a triangular-shaped interferometer, like the Einstein Telescope. Since the detector will be space-based there is no need for complex vacuum tubes which embed the lasers and test masses. The plan is for eLISA to have arm-lengths of about 2.5×10^6 km. Noise is expected to reduce drastically compared to standard ground-based interferometers. eLISA will be measuring signals in the mHz range [100], thus being interesting for galactic and extra-galactic binaries as well as possible gravitational wave signals from processes in the early universe like phase transitions [100, 104]. At the moment important research on the feasibility and technically challenges is being done with the LISA-pathfinder mission, which has shown that indeed very good sensitivities can be reached [104]. eLISA is expected to be operationally at some point in the 2030s.

Several other space-based detectors worth mentioning here are DECIGO [105, 106] and BBO [105], both of these will be similar to eLISA, but are planned to be sensitive to slightly larger frequencies (0.1 mHz) and have better sensitivities.

The last type of gravitational wave experiments are the Pulsar Timing Arrays. These experiments are based on the extremely precise measurement of pulses coming from a pulsar. Gravitational waves will affect the speed of light, thereby changing the arrival time of a pulse if the photons encounter a gravitational wave along the way. Due to

the well-known periodicity of pulsar any change in periodicity can in principle be detected, thus giving an indirect measure of the gravitational wave background [100]. Of all the experiments PTAs are in general sensitive to the lowest frequencies, namely to frequencies in the nHz range.

In order to determine if an experiment will be able to detect gravitational wave signals from phase transitions in a certain model, as calculated from eqs. (3.18), (3.22) and (3.23) for respectively the collisional, soundwave and turbulence contribution, the expected signal needs to be compared to the experimental sensitivity.

Following refs. [89, 100, 107], the sensitivity of an experiment is (partially) limited by the noise measured in the experiment. The noise can be defined either in terms of the characteristic strain h_n, the power spectral density amplitude, $S_n^{1/2}$, or the gravitational wave spectral energy density Ω_{noise}, these three definitions of the sensitivity are related through [100, 107],

$$\Omega_{\text{noise}}(f) = \frac{2\pi^2}{3H_0^2} f^3 S_n(f) \,, \tag{3.37}$$

$$h_n(f) = f^{1/2}[S_n(f)]^{\frac{1}{2}} \,. \tag{3.38}$$

The quantity which is usually plotted is Ωh^2, which has the advantage that it does not depend on the relatively badly known Hubble constant [89],

$$\Omega h^2 = \frac{2\pi^2}{3} f^3 S(f) \left(\frac{h}{H_0}\right)^2 \,, \tag{3.39}$$

with $H_0 = h \times 100$ km s^{-1} Mpc^{-1}

Given the power spectral density amplitude or the characteristic strain, which is the function usually given for an experiment, it is straightforward to change this into the spectral energy density. For each experiment the (design) sensitivity can be found in the literature (see e.g. ref. [107]). For a range of operational and planned experiments these sensitivity curves are shown in fig. 3.3.

An important quantity to determine the discovery potential of a signal for a given experiment is the signal-to-noise ratio (SNR), defined as,

$$\text{SNR} = \sqrt{2t_{\text{obs}} \int_{f_{\text{min}}}^{f_{\text{max}}} \mathrm{d}f \left[\frac{\Omega_{\text{GW}}(f)\, h^2}{\Omega_{\text{noise}}(f)\, h^2}\right]^2} \,. \tag{3.40}$$

Here t_{obs} is the time for which the experiment is operational, given in seconds. $\Omega_{\text{GW}}h^2$ and $\Omega_{\text{noise}}h^2$ are respectively the GW signal from the first order phase transition and the

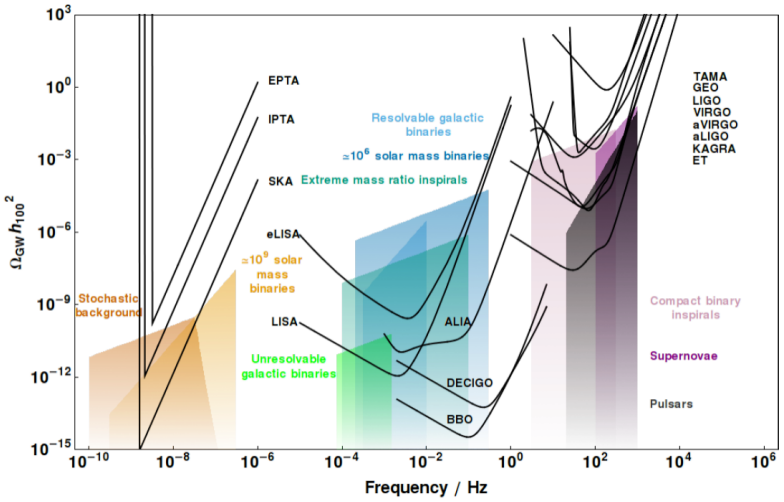

FIGURE 3.3: Sensitivity curves in terms of $\Omega_{\rm GW}h^2$ as a function of frequency, from ref. [89]

sensitivity of the experiment in terms of the energy density. The frequencies $f_{\rm min}$ and $f_{\rm min}$ are determined by the frequency band for which a given experiment is sensitive.

Note that when plotting sensitivities in terms of Ωh^2 the area for which the signal and the experimental sensitivity overlap does not straightforwardly correspond to the SNR [89].

Following ref. [93], we find the sensitivity curves of the experiments from refs. [105, 106, 108] for respectively the B-DECIGO, FP-DECIGO and BBO and LISA experiments. The sensitivity curves used in the following chapter assume 5 years of run-time ($t_{\rm obs} = 5$ years) and a threshold signal to noise ratio of 5.

This page was intentionally left blank.

Chapter 4

Gravitational wave signals from a strongly coupled dark sector

In chapter 2 we have derived equations for the effective potential of three effective low-energy models for QCD-like theories. Afterwards, in chapter 3, we showed how the effective potential can be used to derive the gravitational wave signals from a first order phase transition. In this chapter these results will be combined to derive the gravitational wave signal from a first order phase transition in a QCD-like theory.

The chapter is organized as follows: first we will discuss how the parameters in the three effective models, the (P)NJL model and the LSM, can be chosen such that the models give comparable results. Secondly, several sets of parameters will be given. These benchmark points will be subsequently used to determine the predicted gravitational wave spectra for each of the effective models. Afterwards we will show how these results can be extended straightforwardly to also determine the gravitational wave spectra of phase transitions at different energy scales. The chapter will end with a discussion of these results, highlighting the interesting aspects and discussing possible issues and improvements.

The results presented in this chapter are based on work done in collaboration with J.Kubo and A.Helmboldt, as presented in ref. [1].

4.1 Parameter choices

To compare the different effective models we will choose the parameters of each model such that the observables, i.e. the meson masses and the pion decay constant, match.

The NJL and the PNJL model each have two free parameters, G and G_D, while all other parameters are fixed as discussed in chapter 2. The meson masses are determined as summarized in chapter 2, eq. (2.28), whereas the pion decay constant f_π is given by [48, 109]:

$$f_\pi^2 = 4n_c M_c^2 I_0(v_\sigma) \,, \tag{4.1}$$

$$I_0(v_\sigma) = \int \frac{\mathrm{d}^4 k}{i(2\pi)^4} \frac{1}{(k^2 - M_c^2)^2} \,, \tag{4.2}$$

with M_c the constituent quark mass at the minimum; $M_c = M(v_\sigma)$. The pion decay constant is determined at zero temperature. Similar to the divergent integrals we encountered previously in the (P)NJL model, this integral is regularized using a four-dimensional Euclidean cut-off Λ. We set the cut-off scale to $\Lambda = 0.93$ GeV, such that the dark sector resembles real-world QCD closely [23].

It is clear that with two free parameters and four observables (the fifth observable m_π is per definition zero in the chiral limit), only two of the observables can be tuned to match experimental data, the other two observables will be *predictions* of the model. In the case of real world QCD, a 3-flavour NJL model will have more parameters; e.g. G_D, G, $m_u \approx m_d$ and m_s, but the number of observables is also much larger due to the produced mass splitting within the octets. In ref. [55] the mass spectrum of the pseudoscalar mesons is derived and it can be seen that the NJL model actually does a decent job in predicting meson masses. Given G and G_D we can thus uniquely determine the mesons masses as well as the pion decay constant. For the NJL model the mass spectrum for one set of parameters is shown in fig. 2.5. As mentioned previously, the gluon dynamics does not affect the zero temperature observables, the PNJL model therefore has the same mass spectrum as the NJL model.

On the other hand, the LSM has four free parameters in the chiral limit, c, λ_σ, λ_a and m^2. In principle this allows for each observable to be tuned separately. In order to ensure that the observables are the same in all three effective models, we first fix G and G_D. Given these parameters it is straightforward to derive the predicted mass spectrum and pion decay constant in the NJL and PNJL models. Finally, using these observables as input parameters for the LSM, the free parameters of the LSM can be calculated.

Working with parameter sets determined in the manner described above ensures that the mass spectra, as well as the pion decay constant, are the same. To allow for some variation in G and G_D we will in this chapter work with four sets of benchmark points, these benchmark points are chosen such that the phase transition is first order. We only consider small deviations from the parameters describing real-world QCD. Tables 4.1

benchmark point	(P)NJL model		Linear Sigma Model			
	$G[\,\mathrm{GeV}^{-2}]$	$G_D[\,\mathrm{GeV}^{-5}]$	$m^2[\,\mathrm{MeV}^2]$	λ_σ	λ_a	$c[\,\mathrm{MeV}]$
A	3.84	-90.65	-4.2×10^3	16.8	12.9	2369
B	3.99	-106.45	4.8×10^3	25.5	15.2	4091
C	4.00	-60.00	2.4×10^4	14.8	14.0	1196
D	5.00	-60.00	1.9×10^5	33.3	25.1	2176

TABLE 4.1: Model parameters corresponding to the meson masses in table 4.2. The UV cutoff scale of the (P)NJL model is set to $\Lambda = 930$ MeV. From ref. [1].

benchmark point	f_π [MeV]	m_π [MeV]	m_σ [MeV]	$m_{\eta'}$ [MeV]	m_a [MeV]
A	72	0	248	458	491
B	90	0	400	672	697
C	74	0	291	328	431
D	108	0	694	535	792

TABLE 4.2: Mass spectra and pion decay constant of the benchmark points presented in table 4.1. From ref. [1]

and 4.2 summarize the model parameters and the resulting meson masses and pion decay constant for each benchmark point and effective model.

Before discussing the predicted gravitational wave spectra, we will, for one of the benchmark points, show explicitly that indeed the phase transition in all three effective models is first order. This is done by determining the global minimum of the potential as a function of temperature, the results of this calculation are shown in fig. 4.1.

Several aspects of this figure are interesting to mention; First of all the global minimum for all three models is clearly discontinuous as a function of temperature. This signifies that indeed the phase transition is first order. Secondly, the NJL and PNJL model are equivalent for small temperatures. This is true by construction, since for small temperatures the temperature corrections to the effective potential will be subleading. At zero temperature any contribution from the gluon dynamics will completely disappear. A third interesting feature is that the gluon dynamics *increases* the critical temperature of the PNJL model with respect to the NJL model. Note that this observation agrees with literature, see e.g. ref. [58]. On a last note, fig. 4.1 shows that, for these effective models, not only the critical temperature but also the vacuum expectation value of σ is of similar magnitude but by no means equal. Considering the different origins of these effective models and different degrees of freedom contained within them this is perhaps not a surprise. Already from this result we can expect that these effective models will in

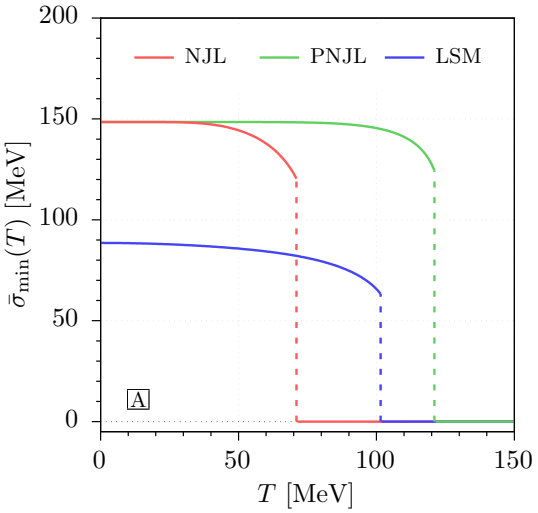

FIGURE 4.1: Global minimum of the effective potential, $\bar{\sigma}_{\min}$, for each of the low-energy effective models. Calculations have been done for benchmark point A of table 4.1. From ref. [1].

general not predict exactly the same gravitational wave signals. To determine the discrepancies between the predicted gravitational wave signals we will in the following section calculate the predicted signals for each of the effective models explicitly.

4.2 Chiral Phase Transition at $\mathcal{O}(100\ \mathbf{MeV})$

Using the benchmark points defined in table 4.1, the gravitational wave signal produced during a first order phase transition in each of the effective models can be determined. It is straightforward to show that for each benchmark point the phase transitions occurs around $T = 100$ MeV, thus implying that the hidden sector closely resembles real-world QCD.

We start by determining the effective action, $S_3(T)/T$, as a function of T, by solving the bounce equation with CosmoTransitions [96], as discussed in chapter 3. For benchmark point A these results are shown in fig. 4.2 for each effective model. Interestingly, the points can be seen to lie on a line which is approximated very well by:

$$\frac{S_3(T)}{T} \approx b\left(1 - \frac{T}{T_c}\right)^{-\gamma} \quad \text{for} \quad T \leq T_c\,. \tag{4.3}$$

Note that for $\gamma > 0$, this function has a pole at $T = T_c$. As discussed previously, this is exactly the behaviour the true minimized action should have since at $T = T_c$ both minima are equal and tunnelling will thus take an infinitely long time.

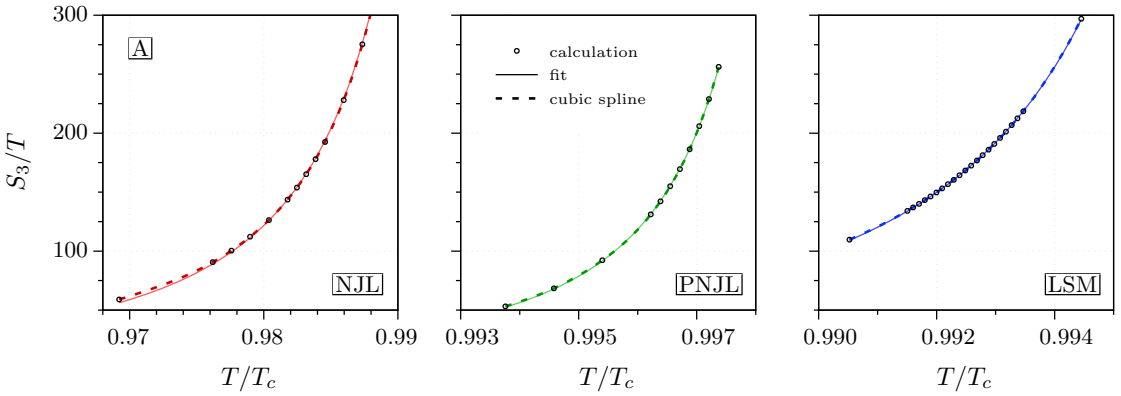

FIGURE 4.2: Minimized effective action $S_3[\sigma_0]/T$ as a function of the dimensionless temperature T/T_c for benchmark point A of table 4.2. The black circles correspond to the explicit calculations, whereas the continuous coloured lines correspond to the fit of the datapoints to eq. (4.3). The interpolating cubic spline is shown by the dashed coloured lines. From ref. [1].

BP	effective model	T_c [MeV]	T_n [MeV]	$g_\star \alpha$	$\frac{\beta}{H}$ [10^4]	γ	b
A	NJL	71.7	70.5	3.4	1.8	1.76	$1.3 \cdot 10^{-1}$
	PNJL	121.8	121.4	1.1	9.4	1.82	$5.0 \cdot 10^{-3}$
	LSM	101.8	101.0	0.8	4.4	1.86	$1.8 \cdot 10^{-2}$
B	NJL	107.1	106.4	2.6	4.3	1.80	$2.3 \cdot 10^{-2}$
	PNJL	140.5	140.2	2.0	13.8	1.87	$2.0 \cdot 10^{-3}$
	LSM	145.8	145.3	0.7	8.6	1.89	$4.6 \cdot 10^{-3}$
C	NJL	90.8	90.6	1.2	11.1	1.81	$4.0 \cdot 10^{-3}$
	PNJL	131.3	131.1	0.9	45.7	1.85	$2.4 \cdot 10^{-4}$
	LSM	100.5	99.9	1.1	5.7	1.87	$1.1 \cdot 10^{-2}$
D	NJL	180.3	180.3	0.4	162.6	1.92	$1.4 \cdot 10^{-5}$
	PNJL	198.3	198.3	0.3	244.9	1.86	$9.7 \cdot 10^{-6}$
	LSM	175.3	174.5	1.2	7.8	1.91	$5.0 \cdot 10^{-3}$

TABLE 4.3: Parameters characterizing the (hidden) chiral first order phase transition for each effective model and benchmark point from. $g_\star = 47.5$ throughout. From ref. [1]

The interpolation of $S_3(T)$ will be used to determine the nucleation temperature as well as β/H. The parameters b and γ are determined by fitting the results of explicit calculations to eq. (4.3). Additionally, α and the critical temperature can be determined as described in chapter 3. All these results are summarized in table 4.3, for each benchmark point and each effective model. As mentioned $g_\star = 47.5$, which corresponds to a dark sector with three fermion flavours and colours together with eight gluons.

Similarly to what we saw for benchmark point A, the critical temperature in the PNJL model is generally larger than that of the NJL model. On the other hand, the critical

temperature of the LSM can be both smaller and larger than those of the (P)NJL models. Furthermore, the nucleation temperature is rather close to the critical temperature. As discussed, this signifies a weak first order phase transition. The generically small values of $\alpha \sim 0.1$ concur with this observation. Note that the weak transition means that there will not be any significant supercooling or reheating [93], which justifies the use of the radiation energy density in the definition of the Hubble constant, eq. (3.6). Since the transition happens at a relatively large temperature and in the absence of supercooling or reheating, the use of S_3 instead of S_4 is also valid.

At last, note that the values of β/H obtained for the phase transitions in these effective models are, perhaps somewhat unexpectedly, rather large. Remember that β/H is actually *calculated* from the effective models and is not an estimate. This result is significantly different compared to previous work on this topic, see e.g. refs. [35–37, 110], where β/H was generally *estimated* to be around $\beta/H =\in [1, 100]$. In ref. [110] a value of $\beta/H \sim \mathcal{O}(1-100)$ is estimated as follows: starting from the definition of β/H

$$\frac{\beta}{H} = T_n \left. \frac{\mathrm{d}(S_3[\phi_0]/T)}{\mathrm{d}T} \right| , \tag{4.4}$$

the derivative can be expanded as,

$$\frac{\beta}{H} = \left(\frac{\mathrm{d}S_3}{\mathrm{d}T} - \frac{S_3}{T} \right)_{T=T_n} . \tag{4.5}$$

Neglecting the first term and using the definition of T_n, see eqs. (3.5) and (3.12), we can approximate β/H by

$$\frac{\beta}{H} \approx 4 \log \frac{M_{\mathrm{Pl}}}{T_n} . \tag{4.6}$$

Due to the logarithmic dependence on M_{Pl} and the large value of M_{Pl} this approximation will give $\beta/H \sim \mathcal{O}(100)$ for a large range of nucleation temperatures T_n. Thus explaining why an estimate of $\beta/H \sim 100$ is often used in the literature. However, from this argumentation we can also see why it fails for our models and benchmark points. As a result of the weak first order phase transition, with $T_n \sim T_c$, the derivative term in eq. (4.5) is expected to be large[1] and can therefore not be neglected. In for example ref. [111] β/H was also determined within a LSM as an effective model for some dark sector and also here a β/H value larger than the conservative estimate of $\mathcal{O}(100)$ was found. Note that for a strong first order phase transition with $T_n \ll T_c$ the estimate $\beta/H \sim \mathcal{O}(100)$ should remain valid for a large range of T_n.

Given the parameters describing the phase transition as summarized in table 4.3, it is now possible to determine the corresponding expected gravitational wave signal. The

[1] This is the case because $S_3(T)$ is expected to approach infinity for $T \to T_c$.

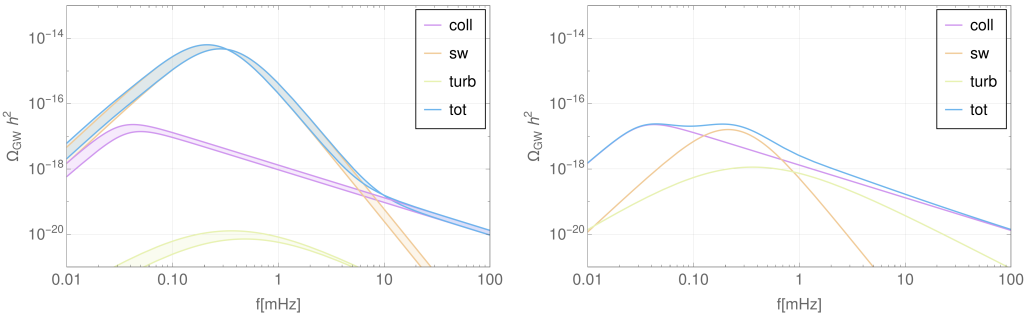

FIGURE 4.3: The contribution from bubble collisions, soundwaves and turbulence to the total gravitational wave spectrum. On the left without suppression(enhancement) factors for soundwaves(turbulence), on the right with this additional factor.

uncertainty in the bubble wall velocity v_w will be taken into account by determining a band of gravitational wave signals covering $0.75 \leq v_w \leq 1$. Note that the large β/H values calculated for the phase transition signify *fast* phase transitions, i.e. $\tau_{sw}H < 1$ with τ_{sw} defined in eq. (3.31). Since the validity of the suppression(enhancement) term for the sound(turbulence) contribution to the gravitational wave spectrum, i.e. eqs. (3.35) and (3.36), is not yet explicitly proven in simulations, we will calculate the gravitational wave spectrum both *with* and *without* the additional factor. The true signal will then likely lie somewhere between these two estimates.

In chapter 3 it was argued that the soundwave contribution is expected to be dominant since we are assuming the scalar has sizeable interactions with the plasma, thus resulting in a significant energy transfer from the bubble wall to the plasma and consequently resulting in a non-runaway scenario [28]. To explicitly show this, fig. 4.3 shows for benchmark point A of the NJL model the gravitational wave signal from each of the three contributions. On the left without the extra factor from fast transitions, i.e. eqs. (3.18), (3.22) and (3.23), on the right with this extra factor, i.e. eqs. (3.18), (3.35) and (3.36). With $\kappa = 1$ for the contribution from bubble wall collisions. For the right figure only the spectrum for $v_w = 1$ is shown while in the first figure a band is shown for $v_w = 0.75$ to $v_w = 1$. Since the gravitational wave signal which include effects from fast transitions is anyway strongly suppressed looking into bubble wall velocities $v_w < 1$ will only result in further suppression.

Although in the right plot of fig. 4.3 the contribution from collisions is shown, this contribution should probably not be taken seriously. Naively fast transitions should also affect the ability of bubbles to efficiently collide and produce gravitational waves, thus affecting the validity of the envelope approximation. The envelope approximation will thus likely *overestimate* the contribution of bubble collisions to the gravitational wave signal. Since already the envelope contribution gives a gravitational wave signal

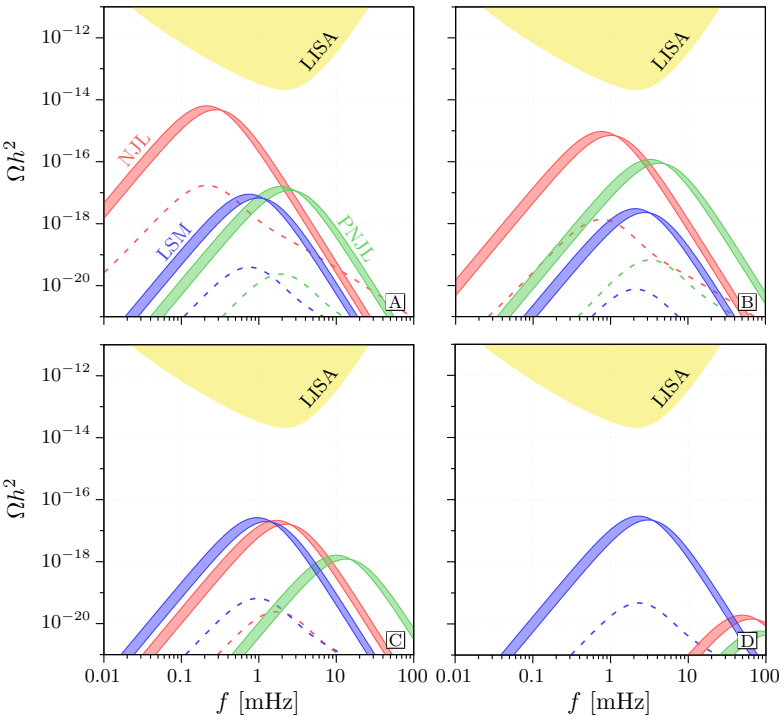

FIGURE 4.4: Predicted gravitational wave spectra for each of the benchmark points and models. Also shown is the power-law integrated sensitivity curve for the LISA experiment. The continuous bands show the GW signal without taking into account the additional factor due to the fast transition, whereas the dashed curves show spectra including this factor. From ref. [1].

which is only of the same order of magnitude as the other contributions we will in the following neglect the contribution from bubble collisions.

From fig. 4.3 we can thus conclude that for an order of magnitude estimate of the gravitational wave signals from first order phase transitions it is sufficient to only take into account the soundwave contribution, eq. (3.22), when the additional factor from fast transitions is not taken into account. When we do take this additional factor into account, we will determine both the soundwave and turbulence contribution eqs. (3.35) and (3.36), since these contributions are shown to be of the same order of magnitude.

For the four benchmark points and three effective models the predicted gravitational wave spectrum is shown in fig. 4.4. This figure also shows the power-law integrated sensitivity curve for the LISA experiment [105, 107], for a runtime of five years and a threshold SNR of 5. From fig. 3.3 it is clear that none of the other gravitational wave experiments will have sensitivities good enough to be able to measure the predicted signal.

Figure 4.4 shows that chiral phase transitions around 100 MeV correspond to a peak frequency of about 1 mHz, exactly in the range for which the LISA experiment is most sensitive. Unfortunately the large values of β/H result in suppressed gravitational wave signals. Taking into account the additional suppression as defined in eq. (3.35),

a possible detection from a chiral phase transition seems even further away. Note that the different effective models predict GW signals, which although qualitatively similar, do differ both in size and peak frequency by several orders of magnitude. Furthermore, the predicted GW spectrum also varies by several orders of magnitude depending on the choice of model parameters, i.e. the benchmark points. Note that by plotting the energy density, Ωh^2 the discovery potential, or signal-to-noise ratio, is no longer directly related to the overlapping area between signal and experiment [89]; however it still holds that the further these two are apart the less likely it is for an experiment to detect the signal. We will later give results for the signal-to-noise ratios to give a more quantitative measure of how likely it is for the LISA experiment, or any other experiment, to detect gravitational wave signals from the hidden chiral phase transition.

4.3 Chiral Phase Transition at higher scales

So far the effective QCD-like models we considered describe dark sectors which contain physics at a scale of about $\mathcal{O}(100\,\mathrm{MeV})$, similar to the real QCD theory embedded in the standard model. However, there is in principle nothing which limits these QCD-like dark sectors to this energy scale. QCD-like dark sectors could just as easily contain physics at (much) higher energy scales.

Scaling up the results of the $\mathcal{O}(100\,\mathrm{MeV})$ dark sector is pretty straightforward and, as we will see, does not require a complete recalculation of all quantities needed to derive the gravitational wave spectra. In e.g. ref. [23] the rescaling of a QCD-like NJL model is also discussed. We consider a rescaling with ξ for which the observables of the three effective models, as summarized in table 4.2, are rescaled as follows;

$$m_i \to \xi \cdot m_i \quad \text{and} \quad f_\pi \to \xi \cdot f_\pi \,. \tag{4.7}$$

The rescaling of these observables is achieved by rescaling all dimensionful model parameters as:

$$\begin{aligned} G \to G/\xi^2, \quad G_D \to G_D/\xi^5, \quad \Lambda \to \xi \cdot \Lambda, \\ T_{\mathrm{glue}} \to \xi \cdot T_{\mathrm{glue}}, \quad m^2 \to \xi^2 \cdot m^2, \quad c \to \xi \cdot c \,. \end{aligned} \tag{4.8}$$

Since the critical temperature is completely determined by the model parameters through the effective potential, it will also rescale in the same way, $T_c \to \xi \cdot T_c$. Correspondingly, the dimensionless quantity $\frac{S_3}{T}(T/T_c)$ will remain unchanged by rescaling. There is thus no need to again solve the equations of motions for these rescaled dark sectors explicitly.

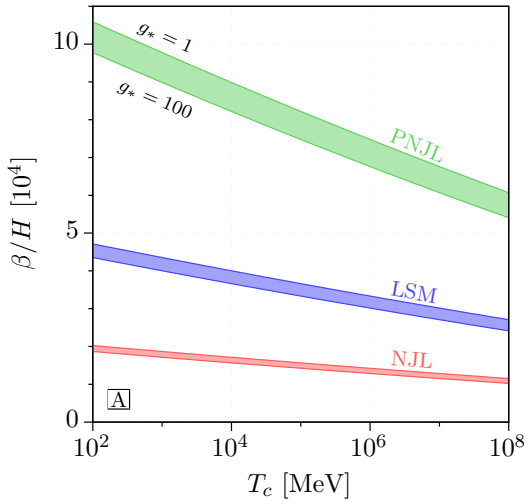

FIGURE 4.5: β/H, the inverse duration of the phase transition as a function of T_c, the critical temperature. Determined for benchmark point A. The band shows the dependence of β/H on $g_\star$, the effective number of degrees of freedom. For our model $g_\star = 47.5$. The lower edge corresponds to $g_\star = 100$ while the upper edge corresponds to $g_\star = 1$. From ref. [1].

The nucleation temperature on the other hand does not exactly rescale like $T_n \to \xi \cdot T_n$. Looking back at the definition of the nucleation temperature given in eq. (3.15), it is clear that M_{Pl}, although being a dimensionful quantity, will not change under rescaling since it is not determined by a model but fixed to a specific value. Consequently, T_n does not exactly scale according to its dimensionality, the discrepancy is however small due to the logarithmic dependence of eq. (3.15) on M_{Pl}.

Since the potential is a smooth function in T, a small deviation in the scaling $T_n \to \xi \cdot T_n$ is not expected to impact α significantly. α, being a dimensionless constant, will thus remain approximately unchanged during rescaling. β/H on the other hand is expected to be rather sensitive to small changes in T_n, due to the pole $S_3(T)$ has at $T = T_c$. We thus expect the dimensionless β/H to change non-negligibly due to rescaling. By using S_3/T and solving eq. (3.15) to find the nucleation temperature, it is possible to find β/H as a function of the scale. In fig. 4.5 β/H is shown as a function of T_c for the different effective models and for benchmark point A. The dependence of β/H on $g_\star$ is shown by the depicted bands. Furthermore, note that $T_c = 100$ MeV corresponds to approximately $\xi = 1$ while $T_c = 10$TeV corresponds to approximately $\xi = 10^5$. Note that the changes in β/H and T_n/T_c are not significant enough to change anything in the discussion on which contribution is the most relevant or change the issue of the phase transition being relatively fast.

Given the dependence of T_n, α and β/H on the rescaling parameter ξ it is now possible to determine the gravitational wave spectrum for any ξ. This will be done in exactly the same manner as for fig. 4.4. Note that due to the redshift, the peak frequencies for all contributions scale with approximately T_n and will thus also scale linearly

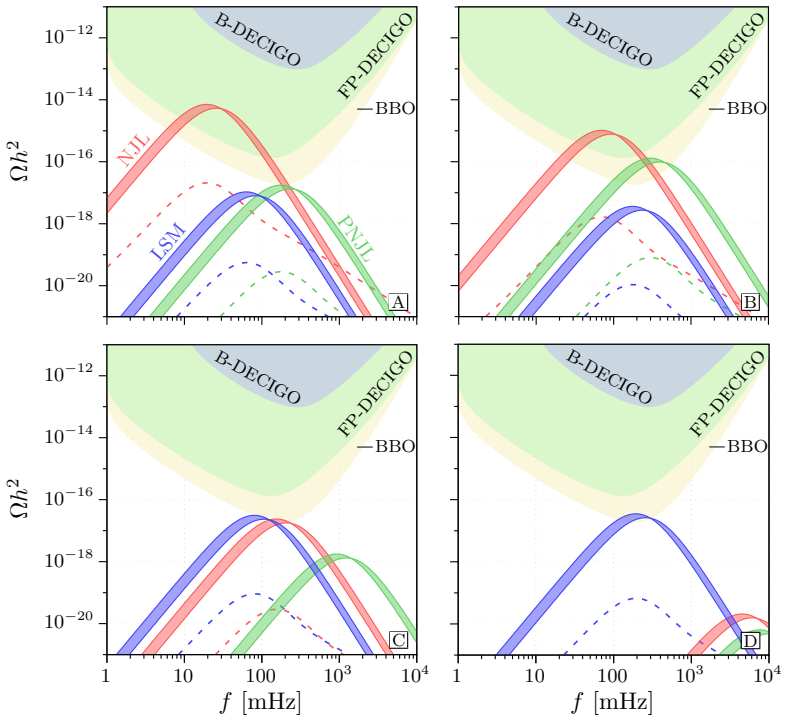

FIGURE 4.6: Predicted gravitational wave spectra for each of the benchmark points and effective models, rescaled with $\xi = 100$. Also shown are the power-law integrated sensitivity curves for the DECIGO and BBO experiments. See text and caption of fig. 4.4 for more details. From ref. [1].

with ξ. For $\xi > 1$ the predicted gravitational wave spectrum will therefore shift to larger frequencies. Thus resulting in signals which, for large enough ξ, will be in the range of experiments like B-DECIGO, FP-DECIGO and BBO, see fig. 3.3. The power law-integrated sensitivity curves for these experiments are again determined for a runtime of 5 years and a threshold SNR of 5. Strain noise power spectral densities for these three experiments can be found in refs. [106], [108] and [105] respectively. Note that other experiments like LIGO or the Einstein Telescope, although sensitive to frequencies of about $1 - 1000$ Hz, have sensitivities which are insufficient to detect the predicted gravitational wave signal, see fig. 3.3.

Figures 4.6 to 4.8 show the predicted gravitational wave spectrum for each of the benchmark points and effective models for respectively $\xi = 100$, $\xi = 10^3$ and $\xi = 10^5$, corresponding to dark sectors with chiral phase transitions occurring at scales between 10 GeV and 10 TeV. Note that changing the scale of the model has almost no effect on the magnitude of the GW signal, only on the position of the peak.

These figures show that, in contrast to the $\mathcal{O}(100\,\text{MeV})$ chiral phase transition, which produces an insufficient GW signal, the scaled up hidden sectors have a much better chance of producing measurable GW signals. This is mainly due to the increased sensitivity of DECIGO and BBO compared to eLISA. Unfortunately, also here, when taking

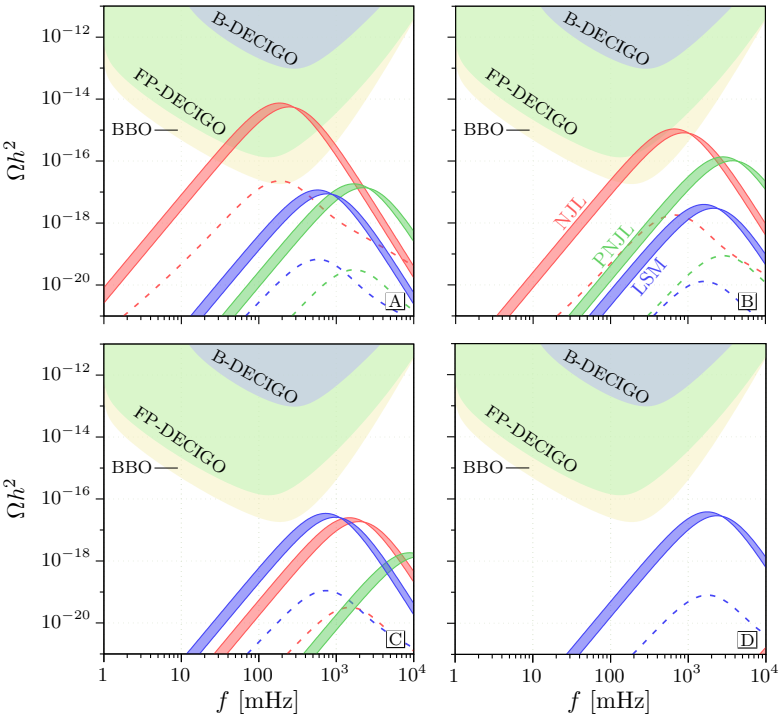

FIGURE 4.7: Predicted gravitational wave spectra for each of the benchmark points and effective models, rescaled with $\xi = 10^3$. Also shown are the power-law integrated sensitivity curves for the DECIGO and BBO experiments. See text and caption of fig. 4.4 for more details. From ref. [1].

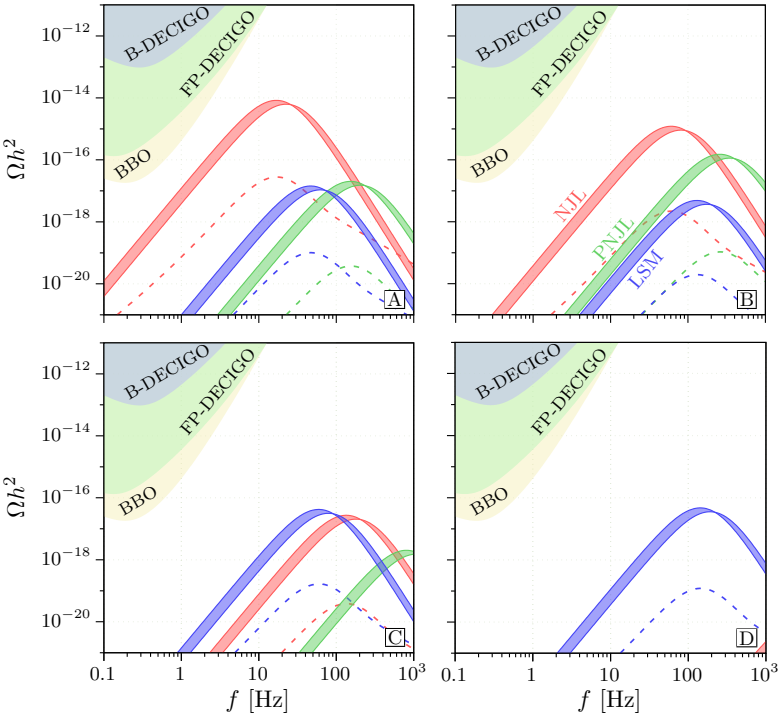

FIGURE 4.8: Predicted gravitational wave spectra for each of the benchmark points and effective models, rescaled with $\xi = 10^5$. Also shown are the power-law integrated sensitivity curves for the DECIGO and BBO experiments. See text and caption of fig. 4.4 for more details. From ref. [1].

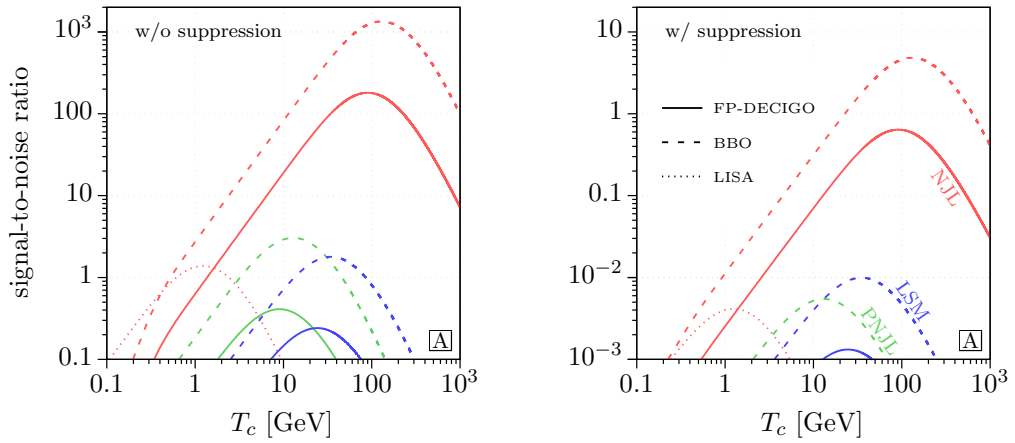

FIGURE 4.9: Signal-to-noise ratio as a function of the critical temperature for benchmark point A. On the left the SNR for which suppression of the soundwave contribution is ignored. On the right with suppression factor. From ref. [1].

into account the additional factor due to the fast phase transition, predicted gravitational wave signals become highly suppressed, thus reducing the chance of detection.

Instead of plotting the energy densities of the gravitational wave signal it is more instructive to determine the signal-to-noise ratio (SNR), eq. (3.40). Of all the benchmark points used benchmark point A has the largest signals, we therefore use this benchmark point to determine the SNR, this is shown in fig. 4.9. As mentioned the SNR gives us a quantitative measure of the discovery potential. In this figure, the SNR is plotted as a function of the critical temperature of the scaled-up effective models, both for the case when the likely soundwave suppression from fast phase transition is taken into account and for the case where this effect is ignored. Signal-to-noise ratios for the three experiments which are most sensitive in the relevant frequency band, i.e. LISA, FP-DECIGO and BBO, are shown.

Figure 4.9 illustrates again the qualitative picture already discussed; measuring a signal from a first order phase transition in a hidden QCD-like sector seems rather unlikely. Although, we have to keep in mind that there is a large uncertainty coming from the choice of effective model and the choice of model parameters as well as the way in which a possible suppression from fast phase transitions is implemented.

4.4 Discussion

Looking back at the two main questions posed in the introduction;

(1) Do different low-energy effective models have similar effective potentials and/or predict similar gravitational wave signals?

(2) Can these GW signals be measured in current or future experiments?

we are now in a position to answer these questions.

Figure 4.1 shows that even though the three effective models predict the chiral phase transition to be first order, they do not generally predict exactly the same critical temperature or vacuum expectation value. The order of magnitude of these quantities is however similar. We can thus conclude that although the qualitative behaviour of each of the models is the same, quantitatively there are $\mathcal{O}(1)$ differences between the predictions of the effective models.

This overall picture carries over to the determination of the quantities related to bubble nucleation, i.e. α, β/H and T_n. Although all similar in magnitude, the discrepancies are also of $\mathcal{O}(1)$, or, in the case of the inverse duration of the phase transition, β/H, even larger. These results were summarized in table 4.3. Consequently there are also large quantitative differences between the gravitational wave spectra predicted by the effective models, see e.g. fig. 4.4.

Thus, the answer to the first question is only partially confirmative; yes low-energy effective models do describe similar effective potentials with critical temperatures of the same order of magnitude. However, the magnitude as well as the peak frequency of the gravitational wave spectra can differ by multiple orders of magnitude. Within each model there is also a large variation in predicted gravitational wave spectra depending on the choice of the model parameters.

The second question unfortunately cannot be answered conclusively either. Due to the large variation in magnitude of the gravitational wave signal depending on both the effective model used and the choice of model parameters it is unclear if a signal will be within detectable range of (future) experiments like LISA, BBO and DECIGO. Note that the discovery potential of such a hidden chiral phase transition seems most favourable for QCD-like models with critical temperatures around the 100 GeV scale.

However all is not lost. To end the discussion on a more positive note I would here like to discuss how these results can proof useful and what could be done to improve on this analysis.

First of all the discrepancy between the models clearly shows that work remains to be done on the effective models describing low-energy QCD, which is in itself a useful conclusion. In order to address and possibly minimize this discrepancy between the effective models one could for example, in the LSM, include the renormalization of the vacuum contributions instead of neglecting these terms. Additionally it is an option to add terms from higher order loop diagrams to the effective potential. One could for example add sunset diagrams to the effective potential of the LSM, however, since these additional diagrams are supposed to be subleading, they should not have a significant effect on for example the critical temperature. By using different, better, renormalization schemes the determination of the effective potential of the (P)NJL model could also be improved, see e.g. ref. [54] for a discussion on renormalization schemes for the NJL model. Furthermore, it is also possible to extend the effective QCD models to include vector mesons.

With the advancement of computational methods, it has also become feasible to calculate properties of QCD on the lattice. Lattice calculations have the advantage that they calculate the full QCD theory from first principles, meaning no effective low-energy models are needed. When the moment comes that these type of calculations can determine for example the effective potential with sufficient precision, one could determine the quantities relevant for bubble nucleation and the gravitational wave spectrum from first principles. Considering the inherent uncertainty involved in choosing effective models, this might be the preferred route to take towards understanding the dynamics of strongly coupled (hidden) theories. Recently in ref. [41] a first calculation in this direction was presented.

Furthermore, when a stochastic background is measured by the GW experiments and its shape points towards the existence of a first order phase transitions[2], these measurements can be used to constrain the possible hidden sectors. Since hidden sectors by construction only interact weakly with the Standard Model conventional experiments like collider experiments will in principle not be able to constrain the parameter space of a hidden sector significantly. The detection of gravitational waves from a first order phase transition thus provides a unique complementary route for investigating physics at high energy scales, like for example hidden sectors.

Hereby part A of this thesis is concluded and we continue with another interesting Standard Model extension, namely scalar extensions. As mentioned in the introduction, the dynamics of (first order) phase transitions in scalar extensions is rather well

[2]Note that there are other stochastic backgrounds, from for example unresolved binaries, which however are not expected to have the same distinct shape as the signals from a first order phase transition. See e.g. ref. [112].

known. This will allow us to hopefully constrain scalar extensions further once gravitational waves from first order phase transitions are detected. In part B another aspect of scalar extensions, also related to physics in the early Universe, will be discussed. To be precise, we will investigate how a scalar can affect the Baryon Asymmetry of the Universe (BAU).

Part B

Effect of a scalar on leptogenesis via oscillations

Chapter 5

Leptogenesis via oscillations

In this chapter some solutions to one of the prominent problems of the Standard Model, its inability to explain the Baryon Asymmetry of the Universe (BAU), will be discussed. The chapter is organized as follows; we will start with a quick reminder of what the BAU is before giving a limited overview of some of the many mechanisms which can explain the BAU. The main focus of this chapter will be on a rather elegant minimalistic way to produce the BAU, namely leptogenesis via oscillations; generally called ARS leptogenesis after the authors of the first paper discussing the mechanism [29]. ARS leptogenesis will be discussed in one of its simplest implementations: the νMSM [30, 113, 114].

After discussing standard ARS leptogenesis and its implementation in the νMSM, we will, in chapter 6, discuss how a scalar extension affects this framework.

5.1 The BAU and its possible production mechanisms

Within the Standard Model of particle physics all elementary particles have a partner with opposite charge, the anti-particles. We observe that the number of baryons today exceeds the number of anti-baryons by multiple orders of magnitude, i.e., there exists a non-zero baryon asymmetry. This asymmetry can be measured indirectly from for example the Cosmic Microwave Background (CMB) or Big Bang Nucleosynthesis (BBN) and has been determined to be [115],

$$Y_{\Delta B} = \frac{n_B - n_{\bar{B}}}{s} \approx 8.75 \times 10^{-11} \, . \tag{5.1}$$

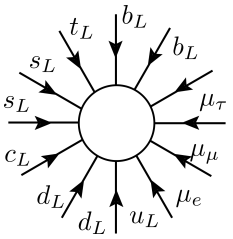

FIGURE 5.1: An example of an electroweak sphaleron interaction.

Here the entropy s is defined as $s = \frac{2\pi^2}{45} g_\star T^3$ and $g_\star$ is the number of relativistic degrees of freedom in the thermal bath. In the early Universe, before electroweak symmetry breaking, $g_\star = 106.75$ for the Standard Model, see e.g. ref. [116].

Although the baryon asymmetry could in principle be set by the initial conditions of the Universe, this explanation is unsatisfactory for multiple reasons; An asymmetry this small would require an extreme fine-tuning in the early Universe. Therefore, it would be more natural that the early Universe started out in a state with equal numbers of particles and anti-particles [115]. Fine-tuning, although not forbidden or impossible, is at the very least somewhat unlikely. Secondly, in order to explain, for example, the observed flatness of the Universe it has been proposed that the early Universe has gone through a period of fast exponential expansion, called inflation. Any initial baryon asymmetry would have been completely diluted during this time [115].

Thus, starting from the hypothesis that the BAU does not result from some fine-tuned initial condition of the Universe, we must conclude that processes in the early Universe are responsible for the observed non-zero BAU. In the 1960s Sakharov proposed three conditions which need to be fulfilled in order to create a Baryon asymmetry [117];

(1) C and CP violation, such that particles behave differently from anti-particles,

(2) Violation of baryon number,

(3) Processes in the early Universe need to take place out of equilibrium, since otherwise interactions producing baryons will be balanced by the inverse interaction.

Note that baryon number does not need to be violated directly, first producing a non-zero lepton asymmetry is in general sufficient. Electroweak sphaleron interactions will then partially transform the lepton asymmetry into a baryon asymmetry. These interactions are of a non-perturbative nature and each interaction involves one particle of each left-handed fermion doublet. Sphaleron interactions are thus 12-fermion interactions, i.e., they involve 9 quark doublets – one for each colour and generation – and 3 lepton doublets. An example of a sphaleron interaction is shown in fig. 5.1.

From the diagram it is clear that sphaleron interactions violate baryon and lepton number as:

$$\Delta B = \Delta L = 3 \,. \tag{5.2}$$

Thus, the electroweak sphaleron interactions *conserve* $B - L$ while $B + L$ is violated.

In general only a fraction of the total lepton asymmetry is transformed into a baryon asymmetry [118]. In ref. [118, 119] this conversion factor c_{sph} is derived as follows; The temperatures we are interested in are all above the electroweak phase transition thus hypercharge is unbroken, consequently sphaleron dynamics needs to conserve hypercharge. From the Standard Model interactions, which are in thermal equilibrium in the early universe, the following conditions for the chemical potentials of the SM particles can be determined [120],

$$\begin{aligned} N_f(3\mu_q + \mu_L) &= 0 \,, \\ N_f(2\mu_q - \mu_u - \mu_d) &= 0 \,, \\ N_f(\mu_q + 2\mu_u - \mu_d - \mu_L - \mu_e + \frac{2}{N_f}\mu_H) &= 0 \,, \\ N_f(\mu_q - \mu_H - \mu_d) &= 0 \,, \\ N_f(\mu_q - \mu_u + \mu_H) &= 0 \,, \\ N_f(\mu_L - \mu_H - \mu_e) &= 0 \,. \end{aligned} \tag{5.3}$$

With μ_q, μ_L, μ_u, μ_d, μ_e and μ_H the chemical potentials of respectively the quark doublet, the lepton doublet, the right handed up and down quarks, the right handed electrons and the Higgs doublet. N_f is the number of flavours. The first condition comes from the electroweak sphaleron interactions and the second from the QCD (strong) sphaleron interactions. These QCD sphaleron interactions are similar to the electroweak ones, but instead of the SU(2) doublets the coloured triplets, i.e., the quarks, participate. Furthermore, the third condition in eq. (5.3) ensures hypercharge conservation. The last three conditions are derived from the Yukawa interactions in thermal equilibrium. Note that above the electroweak scale all gauge bosons have zero chemical potential, they therefore do not appear in these equations.

Note that electroweak sphalerons only couple to the left-handed doublets, not to right-handed particles. This means that a baryon asymmetry can be produced even if the lepton asymmetry in the left-handed plus right-handed sector is zero. In order to create a non-zero baryon asymmetry it is sufficient that the lepton asymmetry in the left-handed sector itself is non-zero [121]. Since QCD sphalerons couple to both left-handed and right-handed quarks they will not play a role in converting a lepton asymmetry into a baryon asymmetry.

Solving the equations listed in eq. (5.3), the baryon and lepton asymmetry can be determined as,

$$B = N_f(2\mu_q + \mu_u + \mu_d)) = 4N_f\mu_q \,, \tag{5.4}$$

$$L = N_f(2\mu_l + \mu_e)) = -\frac{(9N_f + 14N_f^2)\mu_q}{1 + 2N_f} \,, \tag{5.5}$$

$$B - L = \frac{(13N_f + 22N_f^2)\mu_q}{1 + 2N_f} \,. \tag{5.6}$$

Since sphaleron transitions conserve $B - L$ it is now possible to determine the conversion factor: The early Universe started out in a symmetric state with $B = L = 0$, interactions subsequently produce a certain lepton asymmetry. The baryon asymmetry remains zero till sphaleron interactions become efficient around the electroweak scale, thus,

$$(B - L)_{init} = -L_{init} \,. \tag{5.7}$$

Employing $B - L$ conservation we thus have,

$$\begin{aligned} (B - L)_{init} &= (B - L)_{fin} \,, \\ -L_{init} &= B_{fin} - L_{fin} \,, \end{aligned} \tag{5.8}$$

with B_{fin} and L_{fin} defined in eq. (5.6). From these equations the conversion factor c_{sph} is determined to be,

$$c_{sph} = B_{fin}/L_{init} = -28/79 \,, \tag{5.9}$$

for $N_f = 3$. Thus, although a significant fraction of the lepton asymmetry is converted into a baryon asymmetry, the thermal equilibrium condition will forbid full conversion.

Note that sphaleron interactions are mainly efficient above the electroweak scale. After electroweak symmetry breaking sphaleron interactions are exponentially suppressed. Thus, in order for sphalerons to transform a lepton asymmetry into a baryon asymmetry the lepton asymmetry needs to be produced *before* the electroweak phase transition, i.e., at temperatures above $T \sim T_{EW} = 140$ GeV [18, 122].

Within the Standard Model the three Sakharov conditions could all have been fulfilled [115]; baryon number is violated via the electroweak sphaleron processes, whereas CP violation is contained within the CKM matrix which parametrizes the quark mixing. The last condition, departure from thermal equilibrium, can be fulfilled if the electroweak phase transition is sufficiently strong first order. As discussed in part A of this thesis, a first order phase transition occurs via the nucleation of bubbles. Interactions of particles in the plasma with the bubble walls can fulfill the out of thermal

equilibrium condition [18]. However, precise measurements of the Standard Model parameters have shown that both the first and third condition are likely not fulfilled. The CKM matrix only contains a very small amount of CP violation which is not enough to produce a sufficient BAU of $\mathcal{O}(10^{-11})$ and the size of the Higgs mass predicts the electroweak phase transition to be a crossover. The Standard Model, with parameters determined from experiment, can thus not explain the observed baryon asymmetry of the universe. The non-zero BAU determined in experiments is therefore one of the strongest hints for the necessity of a Standard Model extension.

Many Standard Model extensions can be and have been developed which incorporate the three Sakharov conditions and consequently can produce a sufficient BAU. Some of these models are for example GUT baryogenesis [123], thermal leptogenesis [122], resonant leptogenesis [124], Dirac leptogenesis [121], electroweak baryogenesis [18] and ARS leptogenesis [29]. See for example extensive reviews by A.D. Dolgov [125, 126] for a more complete list of baryogenesis mechanisms.

Within *GUT baryogenesis* [123] the BAU is produced in the very early Universe when the electroweak and strong interactions are assumed to be unified, i.e. the Universe is described by a Grand Unified Theory (GUT). When heavy bosons decay out of equilibrium, a baryon asymmetry could be produced. Note that in general GUTs predict proton decay, which has not been observed as of today. This has resulted in very strong limits on the lifetime of the proton, in ref. [42] a lower limit for the proton lifetime of about $\tau \sim 10^{30}$ years is given. It appears difficult to explain the correct BAU as well as predict protons with a long enough lifetime within GUT models, see e.g. [115].

In models with *thermal* [122] or *resonant leptogenesis* [127] the Standard Model is extended with additional sterile neutrinos. By including loop effects it can be shown that the out of equilibrium decay of sterile neutrinos produces a large lepton asymmetry. Through sphaleron interactions this asymmetry can be converted into a baryon asymmetry. In the case of the simplest thermal leptogenesis models a lower bound for the sterile neutrino mass of the order of $M_N \sim 10^9$ GeV was determined [128]. On the other hand, for resonant leptogenesis, where two of the sterile neutrinos are almost degenerate, the lepton asymmetry is resonantly enhanced. Therefore, the lower bound for the sterile neutrino mass can be drastically reduced to $M_N \sim 1$ TeV [124]. The relatively small sterile neutrino masses required in resonant leptogenesis compared to thermal leptogenesis have the additional advantage that current experiments should be able to detect effects from these TeV scale particles in the near future.

In models with *Dirac leptogenesis* [121] the observation that sphalerons only couple to the left handed particles is used. As a consequence, it is sufficient if the left-handed sector has a non-zero lepton asymmetry such that sphaleron processes can convert this

into a non-zero baryon asymmetry. Note that this is even true in the limiting case where the total lepton number in the left- and right-handed sector combined is zero. For lepton number to remain stored within the left handed sector it is required that left and right-handed sectors do not equilibrate, which is the case as long as Yukawa couplings are small. In the simplest toy-model the asymmetry in each sector would be produced through CP violating decays of heavy scalars into sterile neutrinos and leptons.

In *electroweak baryogenesis* [18] the electroweak phase transition is made first order through the addition of one or more extra scalars. The first order phase transitions will make sure the third Sakharov condition is fulfilled through interactions between the bubble and the plasma. The enhanced scalar sector can also incorporate additional sources of CP violation [115]. Electroweak Baryogenesis is interesting from an experimental point of view due to the possibly large gravitational wave signals produced during the first order phase transition. One such experiment, the space-based LISA interferometer, was partially developed with exactly this goal in mind [28], thus being in an ideal position to investigate the plausibility of electroweak baryogenesis.

As mentioned, the baryogenesis mechanism which is the main focus of this chapter is *leptogenesis via oscillations*, also called ARS leptogenesis [29]. In its simplest implementation, called the νMSM [113], the Standard Model is extended by three sterile neutrinos. Lepton asymmetry production will then occur through oscillations between the lepton sector and the sterile neutrinos. Note that, similar to Dirac leptogenesis [121], we will be interested in the lepton asymmetry produced in the left-handed sector. Also in this mechanism the total lepton asymmetry is zero. With these three sterile neutrinos it is possible to explain the BAU as well as the dark matter abundance [30, 113]. This makes the addition of sterile neutrinos a rather economical way of solving multiple of the currently known problems of the Standard Model.

All of these models, as well as many of the models not mentioned here, have interesting aspects regarding their ability to explain not only the BAU but also one or more of the other problems of the Standard Model, like for example the existence of small but non-zero neutrino masses or Dark Matter. However, each of these models also encounters its own problems regarding its ability to produce measurable signals as well as staying within limits from precision measurements, like for example proton decay measurements. Precision experiments as well as collider experiments and gravitational wave experiments will be needed to shed light on which of these models is able to describe the BAU in the most plausible way.

In the remainder of this chapter the mechanism of ARS leptogenesis will be explained and discussed by means of the νMSM. We will show that it is indeed possible to produce a sufficient amount of baryon asymmetry. We will closely follow the work from T.Asaka et al. presented in ref. [114]. In the next chapter we will then discuss an extension of the νMSM with an additional scalar, to determine if and how this additional scalar could affect leptogenesis via oscillations.

5.2 ARS leptogenesis and the νMSM

Within the framework of ARS leptogenesis [29] the Standard Model is extended by multiple sterile neutrinos, N_I. However, contrary to thermal and resonant leptogenesis where the additional sterile neutrinos are heavy, here the sterile neutrinos will be light with masses around the GeV scale. This also means that in the early universe, before electroweak symmetry breaking, the sterile neutrinos will be relativistic. The three Sakharov conditions are then fulfilled as follows [29]; CP is violated through oscillations within the sterile neutrino sector and oscillations between the active and sterile neutrino sectors. The sterile neutrinos are assumed to be only weakly interacting with the active sector, thus resulting in interactions which are out of thermal equilibrium. The sphalerons will subsequently break baryon symmetry. Note that within the ARS mechanism the total lepton number remains zero, however, the active and sterile sector separately do obtain non-zero lepton asymmetry. Due to the chiral properties of the subsequent sphaleron interaction a non-zero baryon number can be produced even though the total lepton asymmetry in the sterile neutrinos plus Standard Model sector is zero. For this mechanism to produce a non-zero lepton asymmetry at least one of the sterile neutrinos species needs to remain out of equilibrium with the active sector till the sphaleron freeze-out temperature.

5.2.1 Model

One of the simplest models in which the ARS leptogenesis can be employed is the νMSM [30]. In this model the Standard Model is extended by three sterile neutrinos. We assume that the lightest sterile neutrinos is almost fully decoupled from the system and can therefore be neglected. Note that approximate decoupling requires that one of the Yukawa couplings is much smaller than the others. Although this could be seen as fine-tuning, there is enough freedom within the model and the experimental data to achieve this. The νMSM will thus be described by a neutrino sector containing three active neutrinos and two sterile neutrinos. Working with only two sterile neutrinos has

as an advantage that the model contains less parameters, compared to a model with three sterile neutrinos. Thus making it easier to deal with as well as making it more predictable. A second advantage is that the third decoupled neutrino could be an ideal Dark Matter candidate [30]. The Lagrangian describing the sterile neutrinos and its interactions with the SM particles is given by:

$$\mathcal{L} = -F_{\alpha I}\bar{L}_{\alpha}\Phi N_{R_I} - \frac{M_I}{2}\bar{N}^c_{R_I}N_{R_I} + (h.c). \,. \tag{5.10}$$

The first term describes the Yukawa interaction between the lepton L, the Higgs boson Φ and the sterile neutrino N_R. Note that all dynamics which will be discussed here takes place at temperatures above the electroweak scale, electroweak symmetry is thus unbroken. The second term is the explicit mass term for the sterile neutrinos. The indices are given as $I = 2,\ 3$ and $\alpha = e,\ \mu,\ \tau$. It is in general always possible to diagonalize either the mass matrix of the active neutrinos or the mass matrix of the sterile neutrinos, here we choose to do the latter.

The Yukawa matrix F is a 3×2 matrix, which through the Casas-Ibarra parametrization is defined as [114, 129, 130],

$$\begin{aligned} F =& \frac{i}{\langle\Phi\rangle} U\sqrt{D_\nu}\Omega\sqrt{D_N} \quad \text{with} \\ \langle\Phi\rangle =& \frac{246}{\sqrt{2}}, \quad D_N = \ \text{diag}(M_2, M_3) \quad \text{and} \quad D_\nu = \ \text{diag}(m_1, m_2, m_3)\ . \end{aligned} \tag{5.11}$$

The matrices U and Ω are defined as,

$$U = \begin{pmatrix} c_{12}c_{13} & s_{12}c_{13} & s_{13}e^{-i\delta} \\ -c_{23}s_{12} - s_{23}c_{12}s_{13}e^{i\delta} & c_{23}c_{12} - s_{23}s_{12}s_{13}e^{i\delta} & s_{23}c_{13} \\ s_{23}s_{12} - c_{23}c_{12}s_{13}e^{i\delta} & -s_{23}c_{12} - c_{23}s_{12}s_{13}e^{i\delta} & c_{23}c_{13} \end{pmatrix} \times \text{diag}\left(1, e^{i\eta}, 1\right) \ ,$$

$$\Omega = \begin{pmatrix} 0 & 0 \\ \cos\omega & -\sin\omega \\ \xi\sin\omega & \xi\cos\omega \end{pmatrix} \ .$$

Normal ordering is assumed throughout. The mass matrices D_N and D_ν are respectively the sterile neutrino and active neutrino mass matrix. And the sterile neutrino masses M_2 and M_3 are conveniently parametrized as $M_{2/3} = M \mp \Delta M/2$. Note that the sterile neutrino masses are required to be highly degenerate in order for the ARS mechanism to work with only two sterile neutrinos [29]. It turns out that this degeneracy is closely related to the mass degeneracy which results in the resonant enhancement of lepton asymmetry production from non-relativistic sterile neutrino decays [124]. See

for example refs. [131, 132] for an extensive discussion on the similarities between resonant leptogenesis and ARS leptogenesis. Additionally, note that extensions in which three sterile neutrino flavours are included allow for much weaker fine-tuning, which is for example discussed in ref. [133].

The mixing angles and active neutrino masses can be determined from neutrino oscillation experiments, these parameters are for example summarized in the Review of Particle Physics from the Particle Data Group [42],

m_1	m_2	m_3	$\sin^2\theta_{12}$	$\sin^2\theta_{13}$	$\sin^2\theta_{23}$
0 eV	8.68×10^{-3} eV	5.03×10^{-2} eV	0.307	0.0218	0.545

(5.12)

The lightest active neutrino mass is set to zero following the assumption that the lightest sterile neutrino is almost completely decoupled from the active sector.

Following ref. [114] the remaining parameters are set to $\xi = 1$, $\omega = \pi/4$, $\delta = 7\pi/4$ and $\eta = \pi/3$. The model thus only has two free parameters which are not yet specified, the sterile neutrino mass M and the mass splitting ΔM.

5.2.2 Kinetic equations

Given the Lagrangian for the νMSM model, eq. (5.10), kinetic equations can be used to characterize interactions of the Standard Model particles with the sterile neutrinos in order to determine how particle densities evolved in the early Universe [134]. Kinetic equations not only track the particle densities, i.e. the diagonal parts of the density matrix, but also track off-diagonal elements such that mixing between particles is taken into account.

For a system of leptons and sterile neutrinos the most general kinetic equation is given by [113],

$$i\frac{\mathrm{d}\rho}{\mathrm{d}t} = [H,\rho] - \frac{i}{2}\{\Gamma^d,\rho\} + \frac{i}{2}\{\Gamma^p, 1-\rho\}\ . \tag{5.13}$$

In this equation $[\ ,\ ]$ denotes the commutator, while $\{\ ,\}$ denotes the anti-commutator. H is the effective Hamiltonian,

$$H = k + H^0 + H_{int}, \tag{5.14}$$

with Γ^d and Γ^p the destruction and production rate, respectively. Note that within the commutator the momentum term k drops out and thus does not affect the kinetic equations.

The density matrix ρ is a block matrix containing all particle densities and mixing terms, in our case the densities and mixing terms of the three leptons, two sterile neutrinos and their anti-particles. The density matrix can be simplified using the fact that all off-diagonal blocks of the block matrix ρ are negligible [113]. Due to the large mass difference between active leptons and sterile neutrinos their mixing will be small. Furthermore, since we assume all particles to be relativistic and the Yukawa couplings to be small the mixing between particle and anti-particle is also negligible. We are thus left with only the block diagonal components of ρ,

$$\rho = \begin{pmatrix} \rho_L & 0 & 0 & 0 \\ 0 & \rho_{\bar{L}} & 0 & 0 \\ 0 & 0 & \rho_N & 0 \\ 0 & 0 & 0 & \rho_{\bar{N}} \end{pmatrix} . \tag{5.15}$$

The density matrices for the leptons and anti-leptons are given by ρ_L and $\rho_{\bar{L}}$, which are 3×3 matrices. The off-diagonal entries of the density matrices of the (anti-)leptons can be neglected since the oscillations within the active sector are small.

In the early Universe the leptons are in thermal equilibrium with the thermal bath, which allows us to write the density matrix of the (anti-)leptons as,

$$\rho_L = N_D \rho_{eq}(k) A \quad \text{and} \quad \rho_{\bar{L}} = N_D \rho_{eq}(k) A^{-1} , \tag{5.16}$$

with $N_D = 2$, corresponding to the fact that the leptons are part of a doublet. The matrix A is a diagonal matrix containing the chemical potentials for each lepton flavour, $A = \text{diag}(e^{\mu_{\nu_e}}, e^{\mu_{\nu_\mu}}, e^{\mu_{\nu_\tau}})$. The equilibrium density is approximated by the Maxwell-Boltzmann distribution, which for relativistic particles is given by: $\rho_{eq} = e^{-k/T}$. The sterile neutrino densities ρ_N and $\rho_{\bar{N}}$ are 2×2 matrices; each density matrix corresponds to sterile neutrinos of one of the helicity states.

Since all off-diagonal block entries in the density matrix ρ can be neglected, the full density matrix ρ can be approximated by a block-diagonal matrix. The kinetic equation as defined in eq. (5.13) can thus also be split into separate kinetic equations for the (anti-)leptons and sterile neutrinos. The kinetic equation for sterile neutrinos is given by,

$$\frac{d\rho_N}{dt} = -i[H_N, \rho_N] - \frac{1}{2}\{\Gamma_N^d, \rho_N\} + \Gamma_N^p \rho_N , \tag{5.17}$$

with $H_N = H_N^0 + V_N$, the effective Hamiltonian. $[H_N^0]_{IJ} = \sqrt{k_N^2 + M_I^2}\delta_{IJ}$ for $I = 2, 3$. V_N is the effective potential, as a result of interaction with the plasma. Γ_N^d and Γ_N^p are the destruction and production rates for sterile neutrinos, respectively. The last term in the kinetic equation was simplified by assuming Boltzmann statistics, i.e. $\rho_N = e^{-k/T}$.

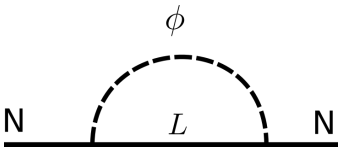

FIGURE 5.2: Diagram contributing to the effective potential of the sterile neutrino V_N.

For relativistic particles in a thermal bath the dominant momentum mode is $k \sim T$, which results in $\rho_N < 1$. Thus, ρ_N can be neglected in the second anti-commutator of eq. (5.13).

Similarly, the kinetic equation for ρ_L can be written as,

$$\frac{\mathrm{d}\rho_L}{\mathrm{d}t} = -\frac{1}{2}\{\Gamma^d_\nu, \rho_L\} + N_D \Gamma^p_\nu \,. \tag{5.18}$$

Note that because ρ_L is diagonal the commutator does not affect lepton production and therefore has been removed from the kinetic equation. Again the second anti-commutator has been simplified. Γ^d_ν and Γ^p_ν are the destruction and production rates of the active neutrinos, respectively. The factor of N_D is added to take into account that $\rho_L = \rho_\nu + \rho_e$, i.e., ρ_L is the density of the doublet. A similar equation holds for the anti-leptons.

To determine the full kinetic equations we thus need to determine the effective potential of the sterile neutrinos and the destruction and production rates for active and sterile neutrinos.

Effective potential

Following ref. [113] we determine the effective potential of the sterile neutrinos, V_N, from the interactions of the sterile neutrinos with the thermal bath of leptons and Higgs bosons. The dominant interaction is shown in fig. 5.2. Note that the effective potential is related to the thermal mass. In e.g. ref. [135, 136] the effective potential is determined within the real-time formalism, which was introduced briefly in appendix A.

Employing the standard Feynman rules from the real-time formalism, the 1-loop diagram shown in fig. 5.2 is given by,

$$-iR\Sigma L = (-iF^\dagger)(-iF) N_D \int \frac{d^4p}{(2\pi)^4} D_{11}(p-k) R S_{11}(p) L \,. \tag{5.19}$$

Here the factor $N_D = 2$ accounts for the fact that doublets are running in the loop. Using the definitions of the propagators as given in eq. (A.8) we can determine the self

energy, which is given by the real part of the 1-loop diagram,

$$\Sigma_{\text{self}} = -iN_D F^\dagger F \int \frac{d^4p}{(2\pi)^4} \left[\frac{i}{(p-k)^2}(-2\pi\delta(p^2)\not{p} n_F(|p_0|)) + 2\pi\delta((p-k)^2) n_B(|p_0 - k_0|)\frac{i\not{p}}{p^2}) \right] , \tag{5.20}$$

$$\Sigma_{\text{self}} = N_D F^\dagger F \int \frac{d^4p}{(2\pi)^4} \frac{\delta(p^2)}{(p+k)^2} \left[\not{p} n_F(|p_0|) + (\not{p} + \not{k}) n_B(|p_0|) \right] , \tag{5.21}$$

where in the second line a change of variables was done to simplify the integral, to be precise, in the first term we change $p \to -p$ and in the second term $p \to p + k$. For the derivation of these equations we assume the chemical potentials and the masses to be zero throughout. Note that the self-energy consists out of two separate terms; one for which the sterile neutrino interacts with the fermion in the thermal bath, the other one for which the interaction is with the Higgs boson in the thermal bath, thus,

$$\Sigma_{\text{self}} = \Sigma^{(F)}_{\text{self}} + \Sigma^{(B)}_{\text{self}} . \tag{5.22}$$

The self energy is further simplified by realizing that we are only interested in the contributions of $\mathcal{O}(T^2)$, all contributions of $\mathcal{O}(T)$ or less are sub-leading. The contribution from the $\not{k}$ term will therefore be ignored.

In order to calculate the integral in the thermal bath, Lorentz invariance is imposed such that Σ_{self} can be parametrized as, $\Sigma^{(B/F)}_{\text{self}} = a^{(B/F)}\not{k} + b^{(B/F)}\not{u} = V^{(B/F)}_\mu \gamma^\mu$. Here the velocity vector is $u_\mu = (1, 0)$ and the 4-momentum is $k_\mu = (\omega, \kappa)$.

The fermion contribution to the effective potential is then found by calculating $V^{(F)}_\mu k^\mu$ and $V^{(F)}_\mu u^\mu$,

$$\begin{aligned} V^{(F)}_\mu k^\mu &= a^{(F)}(\omega^2 - \kappa^2) + b^{(F)}\omega \\ &= N_D F^\dagger F \int \frac{d^4p}{(2\pi)^4} \frac{\delta(p^2)}{(p+k)^2}(p \cdot k) n_F(|p_0|) \\ &= \frac{N_D F^\dagger F T^2}{48} + \mathcal{O}(T) + \dots , \end{aligned} \tag{5.23}$$

and similarly,

$$\begin{aligned} V^{(F)}_\mu u^\mu &= a^{(F)}\omega + b^{(F)} \\ &= \frac{N_D F^\dagger F T^2}{96} I + \mathcal{O}(T) + \dots , \end{aligned} \tag{5.24}$$

with,

$$I = \log \left| \frac{\omega + \kappa}{\omega - \kappa} \right| . \tag{5.25}$$

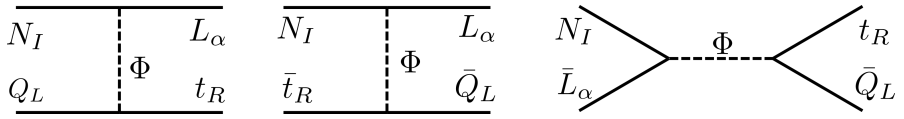

FIGURE 5.3: Feynman diagrams for the $2 \to 2$ interactions contributing to the destruction rate Γ_N^d in the kinetic equations.

The integrals were performed using the following identity for the Dirac delta function,

$$\delta(p^2) = \delta(p_0^2 - \bar{p}^2) = \frac{1}{2|\bar{p}|}\left(\delta(p_0 + |\bar{p}|) + \delta(p_0 - |\bar{p}|)\right) . \tag{5.26}$$

Similarly for the bosonic terms,

$$\begin{aligned} V_\mu^{(B)} k^\mu &= a^{(B)}(\omega^2 - \kappa^2) + b^{(B)}\omega \\ &= N_D \frac{F^\dagger F T^2}{24} + \mathcal{O}(T) , \end{aligned} \tag{5.27}$$

$$\begin{aligned} V_\mu^{(B)} u^\mu &= a^{(B)}\omega + b^{(B)} \\ &= N_D \frac{F^\dagger F T^2}{48} I + \mathcal{O}(T) . \end{aligned} \tag{5.28}$$

Combining everything we get the following equations for a and b,

$$a = a^{(B)} + a^{(F)} = -N_D \frac{F^\dagger F T^2}{16\kappa^2}\left(1 - \frac{\omega}{2k} I\right) , \tag{5.29}$$

$$b = b^{(B)} + b^{(F)} = +N_D \frac{F^\dagger F T^2}{16\kappa}\left(\frac{\omega}{\kappa} + \frac{1}{2}\left(1 - \frac{\omega^2}{2\kappa^2}\right) I\right) . \tag{5.30}$$

The effective potential for the sterile neutrinos is then defined as [136],

$$V_N = b(\kappa, \kappa) = \frac{N_D T^2}{16 k_N} F^\dagger F , \tag{5.31}$$

where $k_N = \kappa$, the momentum of the sterile neutrino.

Destruction and production rates

Several diagrams contribute to the destruction and production rate of the sterile neutrinos, the dominant diagrams for the sterile neutrino destruction rate are the $2 \to 2$ scatterings as shown in fig. 5.3. Similar diagrams contribute to the other production and destruction rates. The diagrams involving the top quark are the dominant contributions due to the $\mathcal{O}(1)$ coupling of the top quark to the Higgs. All other quarks couple much weaker to the Higgs boson. Note that the sterile neutrino decay and inverse decay contributions to the destruction and production rate are subdominant because they

are in the relativistic limit suppressed by a factor M/T compared to scattering processes [29].

From the Feynman diagrams the following decay and production rates in a thermal bath can be derived [114],

$$\Gamma_N^d = \Gamma_N^{d,eq} + \delta\Gamma_N^d \quad \text{and} \quad \Gamma_N^p = \Gamma_N^{p,eq} + 2\delta\Gamma_N^p \,. \tag{5.32}$$

With

$$\begin{aligned}
\Gamma_N^{d,eq} &= 3\gamma_N^d(k_N)F^\dagger F \quad , \quad \Gamma_N^{p,eq} = \rho^{eq}\Gamma_N^{d,eq} \,, \\
\gamma_N^d(k_N) &= \frac{N_C N_D h_t^2}{64\pi^3}\frac{T^2}{k_N} \,, \\
\delta\Gamma_N^d &= \gamma_N^d F^\dagger(A^{-1}-1)F \quad \text{and} \quad \delta\Gamma_N^p = \gamma_N^d \rho^{eq} F^\dagger(A-1)F \,.
\end{aligned}$$

The A^{-1} dependence seen in for example the decay rate comes from the s-channel contribution as depicted in the third diagram of fig. 5.3. The destruction rate of the sterile neutrinos determined from this Feynman diagram will be dependent on the density of the anti-leptons in the thermal bath, as defined in eq. (5.16). Thus when integrating over all leptons in the thermal bath a factor of A^{-1} will remain. Note that this does not hold for the t-channel diagrams, because Pauli-blocking factors, which normally need to be included in decay and production rates in a thermal bath, are neglected, i.e. , we assume $(1 \pm \rho_i) \sim 1$.

For this derivation all particle masses have been neglected, which is a valid assumption in the relativistic limit. Note that for $\mu_i = 0 \rightarrow A = 1$ and the terms $\delta\Gamma_N^{(d/p)} = 0$. These terms are thus only relevant when the chemical potentials of the leptons are non-zero, i.e., when there is a non-zero lepton asymmetry within each flavour. N_C denotes the number of colours, which for all calculations is taken as $N_C = 3$ and h_t is the Yukawa coupling between the Higgs boson and the top quark, we take $h_t = 1$.

Similarly for the destruction and production rate of the active neutrinos [114],

$$\Gamma_\nu^d = \Gamma_\nu^{d,eq} + \delta\Gamma_\nu^d \quad \text{and} \quad \Gamma_\nu^p = \Gamma_\nu^{p,eq} + 2\delta\Gamma_\nu^p \,. \tag{5.33}$$

With

$$\Gamma_\nu^{d,eq} = 3\gamma_\nu^d(k_L)FF^\dagger \quad , \quad \Gamma_\nu^{p,eq} = \rho^{eq}\Gamma_\nu^{d,eq} \,, \tag{5.34}$$

$$\gamma_\nu^d(k_L) = \frac{N_C h_t^2}{64\pi^3}\frac{T^2}{k_L} \,, \tag{5.35}$$

and

$$\begin{aligned}\delta\Gamma_\nu^d &= \gamma_\nu^d(k_L)\int \frac{\mathrm{d}k_N k_N}{T^2}\left[F\left(\rho_{\tilde{N}}^T(k_N)-\rho^{eq}(k_N)\right)F^\dagger\right] ,\\ \delta\Gamma_\nu^p &= \gamma_\nu^d(k_L)\rho^{eq}(k_L)\left[\int_0^{k_L}\frac{\mathrm{d}k_N}{k_L}\frac{1-\rho^{eq}(k_N)}{\rho^{eq}(k_N)}\left(F\left(\rho_N(k_N)-\rho^{eq}(k_N)\right)F^\dagger\right)\right.\\ &\quad\left.+\int_{k_L}^{\infty}\frac{\mathrm{d}k_N}{k_L}\frac{1-\rho^{eq}(k_L)}{\rho^{eq}(k_L)}\left(F\left(\rho_N(k_N)-\rho^{eq}(k_N)\right)F^\dagger\right)\right] .\end{aligned} \tag{5.36}$$

Note that, similar to the production and destruction rates for the sterile neutrinos the terms $\delta\Gamma_\nu^{(d/p)}$ will be equal to zero, if $\rho_N = \rho^{eq}$.

Full kinetic equations

Combining all of the above equations the following kinetic equation for the sterile neutrinos is obtained [114],

$$\frac{d\rho_N}{dt} = -i[H_N^0 + V_N, \rho_N] - \frac{1}{2}\{\Gamma_N^{d,eq}, \rho_N - \rho_{eq}\} + 2\delta\Gamma_N^p - \frac{1}{2}\{\delta\Gamma_N^d, \rho_N\} . \tag{5.37}$$

The corresponding kinetic equation for the other helicity state, $\rho_{\bar{N}}$, can be found straightforwardly by taking the conjugate of this expression, i.e., $A \to A^{-1}$ and $F \to F^*$.

Instead of defining kinetic equations for the lepton and anti-lepton densities separately, it is more convenient to look at the chemical potential of the active neutrino μ_{ν_α}, with $\alpha = e,\ \mu,\ \tau$. Due to thermal equilibrium ρ_L and $\rho_{\bar{L}}$ are related via the chemical potential, see eq. (5.16), it is thus unnecessary to solve kinetic equations for each density separately. Using eq. (5.16) it is straightforward to show that the chemical potential and the densities are related through,

$$\rho_{L_\alpha} - \rho_{\bar{L}_\alpha} = 2N_D\cosh(\mu_{\nu_\alpha})\rho^{eq} , \tag{5.38}$$

$$\frac{\mathrm{d}(\rho_{L_\alpha} - \rho_{\bar{L}_\alpha})}{\mathrm{d}t} = 2N_D\rho^{eq}\cosh(\mu_{\nu_\alpha})\frac{\mathrm{d}\mu_{\nu_\alpha}}{\mathrm{d}t} . \tag{5.39}$$

To remove the dependence of these equations on the active neutrino momentum k_L the left- and right-hand side of this equation can be integrated over k_L,

$$\begin{aligned}\int \mathrm{d}k_L k_L^2\frac{\mathrm{d}(\rho_{L_\alpha} - \rho_{\bar{L}_\alpha})}{\mathrm{d}t} &= \int \mathrm{d}k_L k_L^2 2N_D\rho^{eq}(k_L)\cosh(\mu_{\nu_\alpha})\frac{d\mu_{\nu_\alpha}}{dt}\\ &= 4T^3N_D\cosh(\mu_{\nu_\alpha})\frac{d\mu_{\nu_\alpha}}{dt} .\end{aligned} \tag{5.40}$$

Note that by definition the chemical potential is independent of k_L.

Combining all of the above the kinetic equations for the chemical potentials μ_{ν_α} are determined to be [114],

$$\begin{aligned}\frac{d\mu_{\nu_\alpha}}{dt} =& -\gamma_\nu^d(T)[F.F^\dagger]_{\alpha\alpha}\tanh(\mu_{\nu_\alpha}) \\ &+\frac{\gamma_\nu^d(T)}{4}\int_0^\infty \frac{dk_N k_N}{T^2}\left(\left(1+\frac{2}{\cosh(\mu_{\nu_\alpha})}\right)\left[F.\rho_N.F^\dagger - F^*.\rho_{\bar{N}}.F^T\right]_{\alpha\alpha}\right. \\ &\left.-\tanh(\mu_{\nu_\alpha})\left[F.\rho_N.F^\dagger + F^*.\rho_{\bar{N}}.F^T\right]_{\alpha\alpha}\right)\,,\end{aligned} \tag{5.41}$$

Note that, like in eq. (5.40), also the kinetic equations of eq. (5.16) have been integrated over k_L to remove the dependence on the momentum k_L. The kinetic equations are thus only dependent on the sterile neutrino momentum k_N.

The kinetic equations for the sterile neutrinos and leptons given in eqs. (5.37) and (5.41) are rather complicated coupled integro-differential equations. These equations can only be solved numerically, which is computationally time consuming. In ref. [114] the full momentum dependent solutions to these kinetic equations are discussed. In the following we will employ some simplifications in order to deal with these kinetic equations more efficiently.

First of all we will do a change of variables,

$$x = k_N/T \quad \text{and} \quad z = T_{EW}/T\,, \tag{5.42}$$

such that the particle densities become comoving densities, i.e., the expansion of the universe is automatically taken into account. T_{EW} is given by the temperature of electroweak symmetry breaking, which coincides approximately with the temperature of sphaleron freeze-out and is defined as $T_{EW} \sim 140\,\text{GeV}$. Changing variables in such a way also changes the time derivative. The time derivative in terms of the momentum p and the temperature T in an expanding Universe is given by,

$$\frac{\mathrm{d}}{\mathrm{d}t} = \frac{\partial}{\partial t} - Hp\frac{\partial}{\partial p}\,, \tag{5.43}$$

with H the Hubble constant, which, in a radiation dominated Universe, is defined as,

$$H = \frac{1}{2t} = \frac{T^2}{M_0}\,. \tag{5.44}$$

Here $M_0 = 7.12\times 10^{17}$ GeV. Applying the change of variable as defined above the time derivative is related to the derivative in terms of the dimensionless quantity z as,

$$\frac{\mathrm{d}}{\mathrm{d}t} = \frac{T_{EW}^2}{M_0 z}\frac{\mathrm{d}}{\mathrm{d}z}\,. \tag{5.45}$$

Apart from this change of variables the kinetic equations will be simplified by making the following assumptions [114]:

- We use Boltzmann statistics throughout, such that the equilibrium density is given by the Maxwell-Boltzmann distribution $\rho_{eq} = \mathrm{e}^{-k/T}$.
- All momentum dependence of the particle densities for the sterile neutrinos will be approximately contained in the equilibrium density, i.e. $\rho_N(k) = R_N \rho_{eq}(k)$. Here R_N, like A for the leptons, is momentum *independent*. Equivalently for the sterile neutrinos with opposite helicity, $\rho_{\bar{N}}(k) = R_{\bar{N}} \rho_{eq}(k)$. Note that the leptons and anti-leptons also have densities which are proportional to the equilibrium density.
- To remove all remaining momentum dependence in the kinetic equations all momentum dependent terms will be replaced by their thermal averages. Assuming particles follow the Maxwell-Boltzmann distribution, the thermal average of an operator $\mathcal{O}$ is defined as,

$$\langle \mathcal{O} \rangle = \frac{\int \mathrm{d}k k^2 \mathcal{O} \mathrm{e}^{-k/T}}{\int \mathrm{d}k k^2 \mathrm{e}^{-k/T}} \,. \tag{5.46}$$

  Considering that all terms in the kinetic equations are exactly or approximately inversely proportional to the momentum, i.e., $\sim 1/k$, taking the thermal average corresponds to $k = 2T$. In the case of H_N^0 the choice $k = 2T$ only corresponds to the thermal average in the approximation $k \gg M$, the relativistic limit. An added advantage of the choice $k = 2T$ is that, like the full momentum dependent kinetic equations, these thermal averaged kinetic equations still conserve the total lepton number.

These assumptions have shown to give results which can differ substantially from the full momentum dependent calculation [114, 137]. However as an order of magnitude estimation these simplifications suffice. Furthermore, in the next chapter we will be interested in comparing the predicted BAU in the νMSM with that predicted in its scalar extension. We are thus only interested in the relative change of the produced baryon asymmetry due to the addition of scalar interactions.

All of these assumptions simplify the kinetic equations considerably to,

$$\begin{aligned}\frac{dR_N}{dz}\frac{T_{EW}^2}{M_0 z} =& -i[\langle H_N^0\rangle + \langle V_N\rangle, R_N] - \frac{3}{2}\langle\gamma_N^d\rangle\{F^\dagger.F, R_N - 1\} + 2\langle\gamma_N^d\rangle F^\dagger.(A-1).F \\ & - \frac{\langle\gamma_N^d\rangle}{2}\{F^\dagger.(A^{-1}-1).F, R_N\}\,, \qquad (5.47)\\ \frac{d\mu_{\nu_\alpha}}{dz}\frac{T_{EW}^2}{M_0 z} =& -\gamma_\nu^d(T)[F.F^\dagger]_{\alpha\alpha}\tanh(\mu_{\nu_\alpha}) \\ & + \frac{\gamma_\nu^d(T)}{4}\left(\left(1+\frac{2}{\cosh(\mu_\alpha)}\right)\left[F.R_N.F^\dagger - F^*.R_{\bar N}.F^T\right]_{\alpha\alpha}\right. \\ & \left. - \tanh(\mu_\alpha)\left[F.R_N.F^\dagger + F^*.R_{\bar N}.F^T\right]_{\alpha\alpha}\right)\,, \qquad (5.48)\end{aligned}$$

with $T(z) = T_{EW}/z$.

Assuming we start out in a state without lepton asymmetry and with zero sterile neutrino densities, the initial conditions supplied to these kinetic equations will be: $R_N(0) = R_{\bar N}(0) = \mu_{\nu_\alpha}(0) = 0$.

Solving the kinetic equations, R_N, $R_{\bar N}$ and μ_i can be determined as a function of z. The lepton asymmetry in each sector and the total baryon asymmetry, $Y_{\Delta L_i}$ and $Y_{\Delta B}$, are then determined by,

$$\begin{aligned}Y_{\Delta N_I} =& \frac{1}{s}\int\frac{d^3k}{(2\pi)^3}(\rho_N - \rho_{\bar N})_I = \frac{1}{s}\int\frac{d^3k}{(2\pi)^3}\rho^{eq}(R_N - R_{\bar N})_I = \frac{45}{2\pi^4}(R_N - R_{\bar N})_I\,, \qquad (5.49)\\ Y_{\Delta L_\alpha} =& \frac{1}{s}\int\frac{d^3k}{(2\pi)^3}(\rho_L - \rho_{\bar L})_\alpha = \frac{1}{s}\int\frac{d^3k}{(2\pi)^3}N_D\rho^{eq}(A - A^{-1})_\alpha = \frac{45N_D}{\pi^4}\sinh\mu_\alpha\,, \qquad (5.50)\\ Y_{\Delta L_{tot}} =& \sum_\alpha Y_{\Delta L\alpha}\,, \qquad (5.51)\\ Y_{\Delta N_{tot}} =& \sum_I Y_{\Delta N I}\,, \qquad (5.52)\\ Y_{\Delta B} =& c_{sph}Y_{\Delta L_{tot}}\,. \qquad (5.53)\end{aligned}$$

The entropy s is defined below eq. (5.1) and the number of relativistic degrees of freedom in the thermal bath is given by $g_\star = 106.75$ for the Standard Model before the electroweak phase transition. Note that sterile neutrinos are not expected to affect this value much, since in our case the sterile neutrinos are never thermalized. $Y_{\Delta N_I}$ and $Y_{\Delta L_\alpha}$ are the lepton asymmetry in the sterile and lepton sector, respectively.

In the last equation c_{sph} is the sphaleron conversion factor, which, as derived in the introduction of this chapter, is given by $c_{sph} = -28/79$ for the Standard Model [18].

5.2.3 Timescales

In ARS leptogenesis several timescales play a role, the interplay between these timescales determines how much, if any, lepton asymmetry will be produced. In the νMSM we distinguish between the following timescales: sphaleron freeze-out, sterile neutrino equilibration and the oscillation timescale [137].

As discussed, in order for a lepton asymmetry to be transformed to a baryon asymmetry, the lepton asymmetry needs to be produced before sphaleron freeze-out, set by $T_{sph} \sim T_{EW} \to z_{sph} = 1$.

The second timescale, the sterile neutrino equilibration, is important because equilibration of sterile neutrinos with the thermal bath will result in equilibration of the lepton asymmetry between sectors. Since the total lepton asymmetry in the combined sectors is zero, the final baryon asymmetry will undergo significant washout. The sterile neutrino equilibration timescale can be determined approximately by comparing the Hubble constant with for example the sterile neutrino destruction rate,

$$\begin{aligned} \langle \Gamma_N^d \rangle &= H \,, \\ \frac{3N_C N_D h_t^2}{64\pi^3} F^\dagger F \frac{T}{2} &= \frac{T^2}{M_0} \,, \\ T_{eq} &= \frac{3N_C N_D h_t^2 M_0}{128\pi^3} F^\dagger F \,. \end{aligned} \tag{5.54}$$

We here ignore the flavour effects, since they – although important for the exact dynamics – are only sub-leading in the production.

The last relevant timescale is that of the sterile neutrino oscillations. From the Lagrangian defined in eq. (5.10) it is clear that each sterile neutrino species, N_2 and N_3, has a slightly different mass and coupling to the thermal bath. Consequently, when sterile neutrinos propagate through the thermal bath a phase shift between each sterile neutrino species will develop. This phase shift is crucial in the eventual production of the lepton asymmetry because a non-zero phase shift also results in each species interacting differently with the active neutrino sector. The oscillation timescale, t_{osc}, is defined as the time it takes to build up an $\mathcal{O}(1)$ phase shift [137],

$$\begin{aligned} \Delta\phi &= \int_0^{t_{osc}} ([H_N]_{33} - [H_N]_{22}) \mathrm{d}t \stackrel{!}{=} 1 \\ &\simeq \int_0^{t_{osc}} \frac{\Delta M^2}{4T} \mathrm{d}t \stackrel{!}{\simeq} 1 \,, \end{aligned} \tag{5.55}$$

where in the last line we have assumed $k \ll M$ and $k = 2T$ and neglected contribution of V_N to the mass splitting. ΔM^2 is defined as $\Delta M^2 = M_3^2 - M_2^2$. For sterile neutrino

masses $M_{2,3} = M \mp \frac{\alpha}{2} M$. Equation (5.55) can then be solved as

$$t_{osc} = \left(\frac{3\sqrt{2}\sqrt{M_0}}{\Delta M^2} \right)^{2/3} ,$$

or equivalently,

$$\begin{aligned} z_{osc} &= T_{EW}/T_{osc} \quad \text{with} \\ T_{osc} &= \sqrt{\frac{M_0}{2}} \left(\frac{\Delta M^2}{3\sqrt{2M_0}} \right)^{1/3} . \end{aligned} \tag{5.56}$$

Here we used the definitions of the Hubble constant and z to change the time variable into more useful quantities.

Results

We can now solve the kinetic equations, which we will at first do for $M_N = 10\,\text{GeV}$ and $\delta M_N = \alpha M_N$ with $\alpha = 10^{-8}$. For this choice of parameters the oscillation timescale is given by $z_{osc} = 0.028$ and the timescale of sterile neutrino equilibration is approximately given by $T_{eq} \sim 30\,\text{GeV}$, thus $z_{eq} \sim 5$. For this choice of variables we therefore have $z_{osc} < z_{sph} < z_{eq}$. ARS leptogenesis is thus expected to be efficient in producing a lepton asymmetry and subsequently, through sphalerons, a finite BAU.

Note that when solving the kinetic equations numerically we solve from a finite initial value of $z = 10^{-7}$ up to $z = 1$ with the initial conditions approximated by $R_N(10^{-7}) = R_{\bar{N}}(10^{-7}) = \mu_{\nu_\alpha}(10^{-7}) = 0$.

Solving the kinetic equations and subsequently looking at the evolution of some quantities as a function of z, we can see how the timescales play a role in the dynamics. The evolution of some interesting quantities is shown in fig. 5.4. In these plots the oscillation timescale z_{osc} is depicted by the dashed vertical lines.

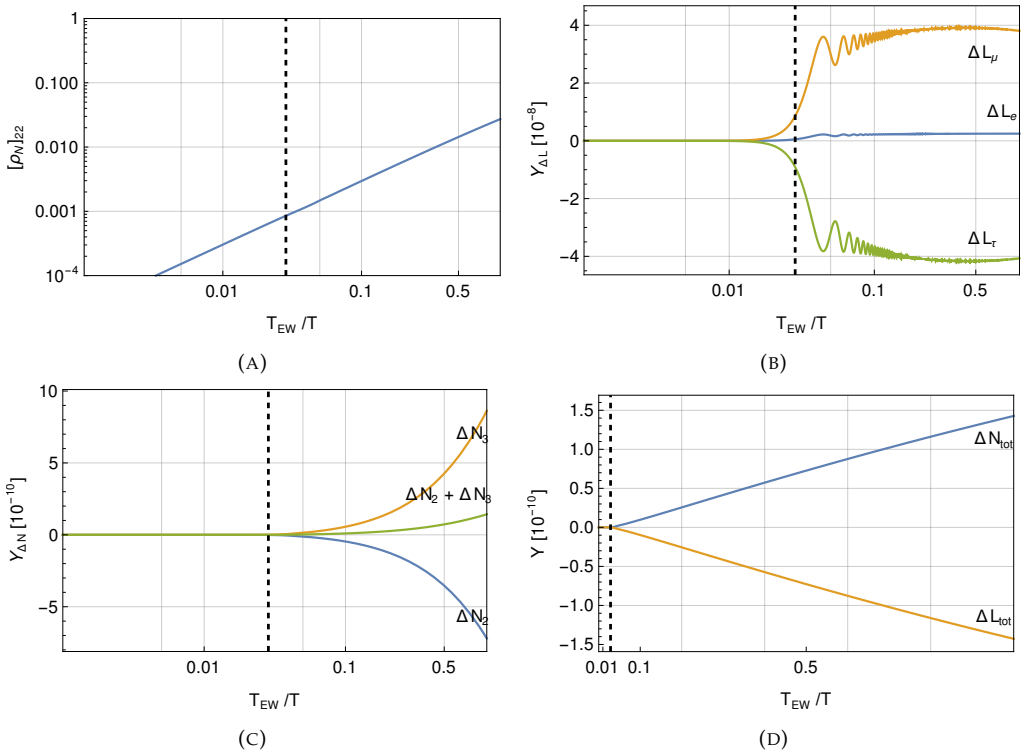

FIGURE 5.4: Solutions to the kinetic equations of the νMSM. Note that in the plots different scales are used for the x- and y-axis. See text for more details on the plots.

In plot (A) the sterile neutrino density ρ_{N_2} is shown, it is clear that the sterile neutrino density does not reach values close to the equilibrium density, which is given by $\rho^{eq} = e^{-k/T} \sim 0.14$ for $k = 2T$. Thereby showing that at least for this case the sterile neutrinos have not equilibrated with the Standard Model thermal bath yet. This is in line with our result that $z_{eq} > 1$.

In plot (B) the lepton asymmetry in the active sector is shown per flavour. Note that the production of asymmetry only starts after some time, which coincides approximately with z_{osc}. Furthermore one sees that the oscillations very quickly become so fast that they effectively average out.

In plot (C) the lepton asymmetry for each helicity of the sterile neutrinos is depicted. Here, like for the leptons, we see that the asymmetry production only starts after z_{osc}.

In the last plot, plot (D), the total lepton asymmetry in each sector is shown. Again we see that the asymmetry is only produced after some initial time. Note that the total lepton asymmetry in both sectors together is equal to zero, i.e, no net asymmetry is produced. This is checked explicitly in the numerical computations. However, since sphalerons couple only to the left-handed particles and not to the right-handed sterile neutrinos, it is sufficient to have a lepton asymmetry in the lepton sector in order to produce a BAU. Note also that in plot (D) no efficient washout of the lepton asymmetry

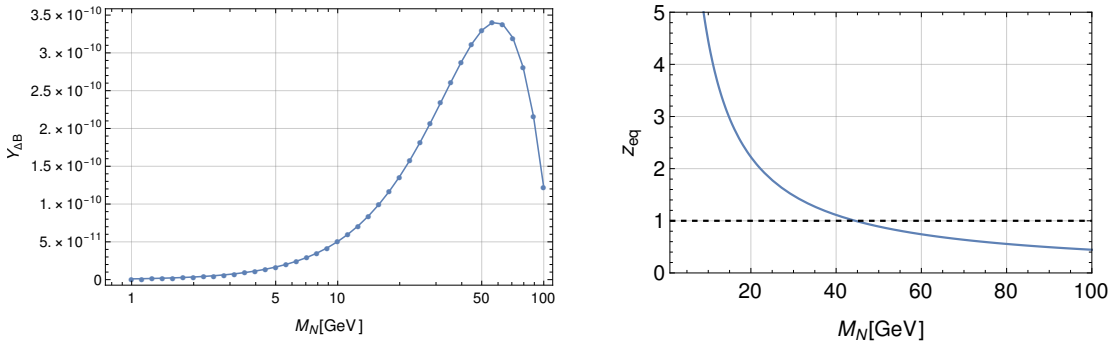

(A) (B)

FIGURE 5.5: *Left:* baryon asymmetry as a function of sterile neutrino mass M_N. *Right:* sterile neutrino equilibration, as defined through eq. (5.54), as a function of the sterile neutrino mass M_N. See text for more details.

can be observed, since $z_{eq} > 1$ and consequently sterile neutrinos have not equilibrated with the Standard Model thermal bath this is to be expected.

From the solution of the kinetic equations a BAU of $Y_{\Delta B} = 5.05 \times 10^{-11}$ is determined. This value is about a factor of 4 smaller than that stated in ref. [114] in which a BAU of $Y_{\Delta B} = 2.73 \times 10^{-10}$ is given. This change is the result of using more recent neutrino parameters, as summarized in ref. [42].

Similar calculations can be done for different choices of the sterile neutrino mass, but before doing that, in order to optimize the calculation further, the kinetic equations will be simplified once more. As we can see from plot (B) in fig. 5.4 as well as eq. (5.55) the oscillation frequency increases as a function of z. Due to these fast oscillations at later times their effect averages out after some point. We can use this to simplify numerically solving the kinetic equations by only solving the full differential equations till $z = Nz_{osc}$. The remaining dynamics till $z = 1$ will then be determined by only solving the diagonal parts of the kinetic equations [137]. We have explicitly calculated the baryon asymmetry for several choices of N,

N	10	20	30
$Y_{\Delta B}$	4.97×10^{-11}	5.04×10^{-11}	5.06×10^{-11}

. (5.57)

Note that large N results in reduced speed in solving the kinetic equations numerically. To have both good precision and a reasonable speed we therefore choose $N = 20$ such that $Y_{\Delta B}$ can be determined accurately up to 1%.

In plot (A) of fig. 5.5 the baryon asymmetry as a function of the sterile neutrino mass M_N is shown, throughout $\alpha = 10^{-8}$. The figure shows that the total baryon asymmetry is maximized at a certain mass, $M_N \sim 60\,\text{GeV}$. This peak can be explained as follows; increasing the sterile neutrino mass increases the active-sterile coupling through

the Casas-Ibarra parametrization, eq. (5.11). Consequently, the amount of asymmetry exchanged between the sectors increases, thus explaining why initially increasing M_N results in an increased asymmetry production. However, for a certain mass the Yukawa coupling becomes so large that the sterile neutrinos will equilibrate, resulting in washout of the produced baryon asymmetry. In plot (B) of fig. 5.5 the approximate equilibration rate is shown as a function of the sterile neutrino mass, the dashed line corresponds to equilibration at electroweak symmetry breaking. Note that the peak in plot (A) of fig. 5.5 corresponds to the sterile neutrino mass for which these two effects balance each other.

5.3 Discussion

We thus see that sterile neutrino oscillations can efficiently produce a lepton asymmetry, which through the sphalerons is transformed into a baryon asymmetry. Note that this does require a rather fine-tuned mass-splitting with $\alpha \sim 10^{-8}$. In for example ref. [133] the assumption of a decoupled lightest sterile neutrino was removed. It was shown that a model with three sterile neutrinos participating in the ARS mechanism allows for enough freedom in the extra parameters to alleviate the finetuning in the mass splitting of the sterile neutrinos.

There are multiple reasons why a further extension of the νMSM could be interesting. Even if neutrino masses, dark matter and leptogenesis can be explained by a minimal SM extension as used in the νMSM, there are still problems with the Standard Model. Some of these problems are for example the unknown nature of Dark Energy, but also problems of a more fundamental nature, like the hierarchy problem and the randomness of all the SM parameters. Additionally there is also an increasing list of experimental results which hint towards the existence of new physics. These anomalies include for example the flavour anomalies [17], the $(g-2)$ muon anomaly [16] and many others.

From a top-down approach the inclusion of sterile neutrinos might seem somewhat arbitrary, they are not needed for the consistency of the model. On the other hand, in many GUT models the theory at lower scales, after symmetry breaking, will apart from the Standard Model symmetries, have residual gauge symmetries. One of these symmetries can for example be the $\mathrm{U}(1)_{B-L}$ symmetry, see e.g. ref. [138]. In order for anomalies to cancel in the presence of a $\mathrm{U}(1)_{B-L}$ symmetry the existence of sterile neutrinos is required, thus explaining their inclusion into a Standard Model extension [139]. In case of a $\mathrm{U}(1)_{B-L}$ symmetry sterile neutrinos would not be allowed to have an explicit

mass term, however, through an interaction of a scalar the sterile neutrinos can obtain a mass when the scalar undergoes spontaneous symmetry breaking.

Additionally, in models where conformal symmetry is imposed on the Lagrangian, such that all explicit mass terms are forbidden, non-zero sterile neutrino mass could also require the existence of additional scalars [140]. Conformally symmetric models are interesting due to their ability to produce mass scales in a theory which on the classical level does not contain mass scales [20]. These theories therefore do not suffer from the hierarchy problem.

Considering the arguments above, it is thus not unreasonable to expect the existence of on or more additional scalars. These scalars can in principle couple to sterile neutrinos, which could consequently affect ARS leptogenesis. In the next chapter the question of how scalars affect ARS leptogenesis will be investigated.

Chapter 6

Scalar extension of the νMSM

In this chapter the framework of ARS leptogenesis, as implemented in the νMSM, will be extended to include an additional scalar. The goal of this chapter is to show when and how scalars affect the dynamics of leptogenesis via oscillations and to hopefully find a region of parameter space where the inclusion of a scalar can enhance the produced baryon asymmetry.

Extensions of the νMSM have for example also been discussed in refs. [141, 142], however in these papers the additional scalar is usually assumed to be non-thermal such that it is not expected to have a significant impact on the leptogenesis mechanism.

The chapter will start with a description of the model, afterwards the effects of the scalar on the kinetic equations will be discussed. In the remainder of the chapter the consequences of these changes for the baryon asymmetry will be shown. We will end with a discussion on how to interpret these results and how to possibly extend this framework further to obtain more interesting dynamics. This chapter is based on work in collaboration with O.Fischer and M.Lindner, which will soon be published [2].

6.1 Model

Many Standard Model extension include one or more new scalars. Without going into the details of a UV complete model, which could for example be related to a $U(1)_{B-L}$ symmetric model [143] or a conformal model [144], we will here look into an effective theory where the only relevant new dynamics is assumed to be that of the scalar. The Majorana mass term in eq. (5.10) will be replaced by a scalar interaction such that the

Yukawa terms in the Lagrangian are given by,

$$\mathcal{L}_Y = -F_{\alpha i}\bar{L}_\alpha \Phi N_i - \frac{1}{2}Y_{ij}S\bar{N}_i^c N_j + (h.c.)\ . \tag{6.1}$$

Here L_α, N_I, and Φ are again the lepton doublet, the sterile neutrino and the Higgs doublet, with $\alpha = e,\ \mu,\ \tau$ and $I = 2,\ 3$. The scalar singlet field is denoted by S. The matrix Y corresponds to the interaction strength of the sterile neutrinos with the new scalar. In the basis where the sterile neutrino mass matrix is diagonalized the Yukawa coupling Y is a diagonal matrix.

The scalar potential will be defined as,

$$V(S,\Phi) = -\frac{1}{2}\mu_S^2 S^2 - \mu_\Phi^2 \Phi^\dagger\Phi + \frac{1}{4}\lambda_S S^4 + \lambda_H(\Phi^\dagger\Phi)^2 + \frac{1}{2}\lambda_{SH}\Phi^\dagger\Phi S^2\ . \tag{6.2}$$

Several cases for the dynamics of the scalar S can be distinguished:

(A) Non-thermalized and $\langle S\rangle = 0$,

(B) Non-thermalized and $\langle S\rangle \neq 0$,

(C) Thermalized and $\langle S\rangle = 0$,

(D) Thermalized and $\langle S\rangle \neq 0$.

Cases (A) and (C) would not be able to explain neutrino masses via the see-saw mechanism as parametrised by the Casas-Ibarra parametrisation, eq. (5.11), unless an explicit mass term for sterile neutrino is included in the Lagrangian. This could be an interesting situation which, however, is not discussed further here.

Case (B), on the other hand, is able to explain neutrino masses, however, because the scalar is assumed to be non-thermalized, it will not affect the dynamics much for two reasons: A non-thermalized scalar will not produce a large sterile neutrino abundance through its decay and secondly, it will not affect thermal masses of the other particles. Note that for late symmetry breaking close to the electroweak scale ARS leptogenesis will effectively be turned off, without sterile neutrino masses and mass differences the whole mechanism stops working. The dynamics of case (B) seems thus straightforward; for early symmetry breaking the model will simply be reduced to the νMSM, while for late symmetry breaking the ARS mechanism will be turned off.

Of these four cases the interesting one, which can explain both the non-zero neutrino masses and can possibly have a non-trivial effect on ARS leptogenesis, is thus case (D).

A thermalized scalar which obtains a non-zero vev, v_s^0 will have the following effects on the sterile neutrinos and its kinetic equations:

The most obvious effect is the inclusion of sterile neutrino mass from the vacuum expectation value:

$$M_I(z) = Y_{II} \cdot v_s(z) \ , \tag{6.3}$$

with $v_s(z)$ the temperature dependent vacuum expectation value. In order to take into account that before symmetry breaking $v_S^0 = 0$ we define $v_s(z)$ as,

$$v_s(z) = v_s^0 \, \Theta(z - z_c) \ , \tag{6.4}$$

with z_c corresponding to the critical temperature at which the scalar undergoes symmetry breaking. $\Theta(z)$ is the Heaviside step function. To avoid overly complicating the model with many extra parameters we choose $z_c = T_{EW}/v_S^0$, i.e. the temperature at which the symmetry breaks is equal to the vacuum expectation value.

When numerically solving the kinetic equations the step function will be approximated by an exponentially function,

$$v_S(z) = v_S^0 \cdot \frac{1}{\mathrm{e}^{-2k(z - T_{EW}/v_S^0)} + 1} \ . \tag{6.5}$$

This function is equal to the Θ-function for $k \to \infty$, we choose $k = 10^5$.

Another important effect is that the sterile neutrino will obtain an additional contribution to the effective potential, or equivalently, a thermal mass, from interactions with the scalar in the thermal bath. The relevant diagram is shown in fig. 6.1. In the derivation below eq. (5.19) the effective potential of the sterile neutrinos from interactions with the Higgs boson and lepton doublet was derived. A similar calculation can be done to determined the effective potential of the sterile neutrinos from interactions with the scalars in the thermal bath and gives,

$$V_N^S = \frac{2}{3} \frac{T^2}{16 k_N} Y \cdot Y \ . \tag{6.6}$$

The additional factor $2/3$ is included because the fermionic contribution to the effective potential is negligible, due to the fact that sterile neutrinos are not thermalized. Furthermore, the factor N_D is not present because no doublets are participating in this interaction. Note that thermal contributions to the sterile neutrino mass will not affect the masses which are used as input in the Casas-Ibarra parametrization eq. (5.11). This equation uses masses as measured today, i.e., the zero temperature masses.

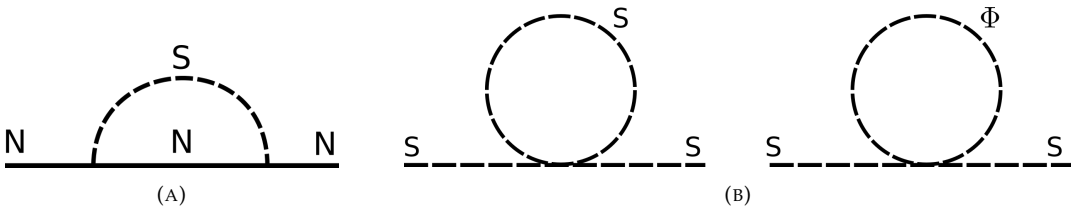

FIGURE 6.1: In (A) the Feynman diagram contributing to the effective potential of the sterile neutrino V_N is shown. In (B), the two diagrams contributing to the thermal mass of the scalar.

The last new contribution to the dynamics due to the presence of scalar interactions is the scalar decay into sterile neutrinos. In the limit of light sterile neutrinos this decay rate can be defined as [145, 146]

$$\Gamma_S = \frac{Y.Y}{16\pi}\frac{1}{\rho^{eq}(x)}\frac{M_S(z)^2}{T_{EW}}\frac{z}{x^2}\int_{y_0}^{\infty} n_s(y)\mathrm{d}y \,, \tag{6.7}$$

with $M_S(z)$ the thermal mass of the scalar z and $n_s(y) = \mathrm{e}^{-y}$, the equilibrium density of the scalars. Furthermore the limit in the integral y_0 is defined as $y_0 = x + \frac{z^2}{4x}\frac{M_s^2(z)}{T_{EW}^2}$. This term basically takes into account energy conservation and Boltzmann or phase-space suppression of the scalar particle number for large scalar masses. Note that inverse decay has been neglected, eq. (6.7) is therefore only valid for $\rho_N < 1$. Furthermore, this equation is only valid for $2M_N(z) < M_S(z)$, such that the decay is kinematically allowed.

To determine the thermal mass of the scalar $M_S(z)$ we look at the Feynman diagrams. At one loop two diagrams contribute to the thermal mass of the scalar, these are shown in fig. 6.1. In appendix A the scalar thermal mass in derived within the imaginary time formalism. Following similar steps one can also determine the thermal mass from interactions with the Higgs boson. The total contribution to the scalar thermal mass, from both the scalars and Higgs bosons in the plasma is given by,

$$M_S(T)^2 = 2\lambda_S(v_S(T))^2 + \frac{1}{4}\lambda_S T^2 + \frac{1}{6}\lambda_{SH}T^2 \,. \tag{6.8}$$

Combining all of the above we can conclude that the kinetic equations of the leptons μ_{ν_α} will not be affected by the new scalar, thus, the second equation in eq. (5.48) is unchanged. The kinetic equations for the sterile neutrinos changes as,

$$\begin{aligned}\frac{dR_N}{dz}\frac{T_{EW}^2}{M_0 z} =& -i[\langle H_N^0\rangle + \langle V_N\rangle + \langle V_N^S\rangle, R_N] - \frac{3}{2}\langle\gamma_N^d\rangle\{F^\dagger.F, R_N - 1\} + 2\langle\gamma_N^d\rangle F^\dagger.(A-1).F \\ & - \frac{\langle\gamma_N^d\rangle}{2}\{F^\dagger.(A^{-1}-1).F, R_N\} + \frac{1}{\rho^{eq}(2T)}\Gamma_S \,,\end{aligned} \tag{6.9}$$

with $[H_N^0]_{II} = \sqrt{k_N^2 + M_{N_I}^0}$ and $M_{N_I}^0 = Y_{II}v_S(z)$, the sterile neutrino mass from scalar

symmetry breaking. The term Γ_S takes into account the additional sterile neutrino production from scalar decay and is defined in eq. (6.7). The additional $\rho^{eq}(2T)$ factor is added because the kinetic equations are in terms of R_N not ρ_N, we substituted $k = 2T$. Note that every scalar decay produces one sterile neutrino of each helicity, the kinetic equation for $R_{\bar{N}}$ is therefore changed in the same way.

Time scales

In chapter 5 it was discussed that three timescales are relevant for the dynamics of leptogenesis in the νMSM: the sphaleron freeze-out, the oscillation time scale and the sterile neutrino equilibration rate. Whereas the sphaleron freeze-out does not change the oscillation time is affected due to the changes to the Hamiltonian. Starting from the same definition as given in eq. (5.55) and substituting eqs. (6.3) and (6.6) the oscillation timescale changes as,

$$\begin{aligned}\Delta\phi &= \int_0^{t_{osc}} ([H_N]_{33} - [H_N]_{22})\mathrm{d}t \stackrel{!}{=} 1 \\ &\simeq \int_0^{t_{osc}} \frac{\Delta M(z)^2}{4T}\mathrm{d}t \stackrel{!}{\simeq} 1 \,,\end{aligned} \tag{6.10}$$

with

$$\Delta M^2(z) = (Y_{33}^2 - Y_{22}^2) \cdot \left(v_s(z)^2 + \frac{2}{3}\frac{T^2}{8} \right) \,. \tag{6.11}$$

Note that again the contribution from V_N has been neglected. For large v_s^0, and thus early breaking since $T_c = v_s^0$ this equation reduces to eq. (5.55) for $T < T_c$.

The timescale of equilibration of sterile neutrinos from the interaction with the active sector z_{eq} is not changed, however an extra equilibration rate is present in this model due to the scalar decay (eq. (6.7)) and inverse decay.

6.2 Effect on BAU production

The model has several free parameters; the Yukawa coupling Y_2 and Y_3, the scalar vev v_S^0, the scalar coupling λ_S and the scalar-Higgs coupling λ_{SH}. Similar to the sterile neutrino masses in the νMSM, we will parametrize Y_2 and Y_3 as,

$$Y_{2/3} = Y \mp \alpha/2 \,, \tag{6.12}$$

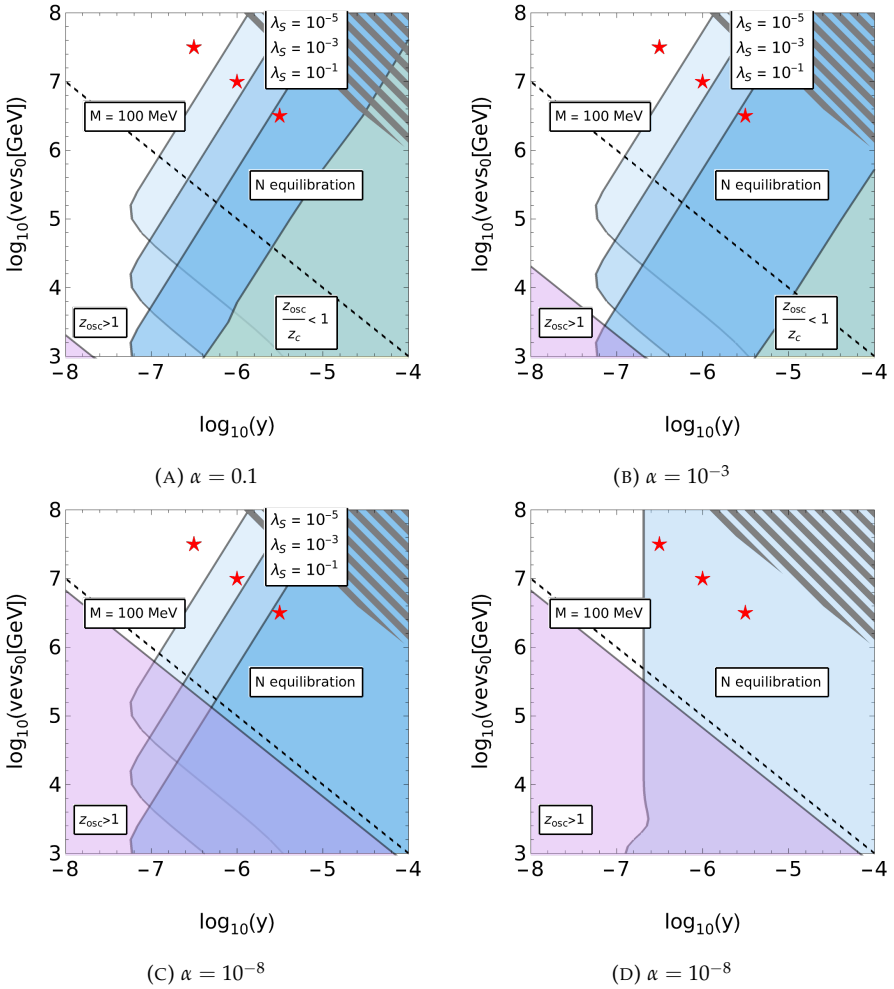

(A) $\alpha = 0.1$ (B) $\alpha = 10^{-3}$

(C) $\alpha = 10^{-8}$ (D) $\alpha = 10^{-8}$

FIGURE 6.2: Parameter space as a function of the parameters Y and v_S^0. See text for more details. Adapted from ref. [2].

such that the zero temperature relative mass splitting in this model and the νMSM are both defined by α.

The parameter λ_{SH} is only relevant for thermalizing the scalar with the Standard Model thermal bath. In for example ref. [147] it is stated that for $\lambda_{SH} \sim 10^{-4}$ the scalar will be thermalized at $T_S \sim 10^6$ GeV. Taking a slightly more conservative choice $\lambda_{SH} = 10^{-3}$ we can assume the scalar will be thermalized for the timescales we are interested in. Note that after electroweak symmetry breaking the scalar and the Higgs boson will mix because both particles will have obtained a vev. Searches for new scalars in collider experiments have given limits on the allowed mixing of the Higgs with a new scalar, however for large scalar masses these limits are rather weak [148]. It is thus not expected to influence the choice $\lambda_{SH} = 10^{-3}$ in the parameter space we are interested in.

To develop some intuition about how each parameter affects the timescales and to determine which parameters warrant closer attention we can have a look at fig. 6.2. This

figure shows the dependence of some of the limits and timescales on these parameters. In the following we will define sterile neutrino equilibration as the values of Y, λ_S and v_S^0 for which sterile neutrino production from eq. (6.7) exceeds $\rho_N > 0.15$ at $z = 1$. Equilibration of sterile neutrinos from interactions with the scalar will occur somewhere around the border of the region defined by the condition. Note that another reason for requiring small sterile neutrino densities is that it ensures that inverse decay can indeed be ignored.

In plot (A), (B) and (C) of fig. 6.2 the blue regions are the regions for which sterile neutrino equilibration occurs due to scalar decay, for several choice of λ_S. Other timescales shown in these three figures are the region where $z_{osc} > 1$ (the pink area) and the region for which $z_{osc}/z_c < 1$ (the green/yellow area). Furthermore the line $M_N = 100$ MeV is shown, this corresponds approximately to the lower limit sterile neutrinos are allowed to have in order not to change Big Bang Nucleosynthesis predictions considerably, see e.g. [149, 150]. Note that the grey-hashed area corresponds to the region where the sterile neutrino mass exceeds 100 GeV. In this region the assumption that the sterile neutrinos are relativistic starts to break down, the framework developed for the ARS leptogenesis mechanism will not be valid here. Lastly these figures show three red stars which denote the three benchmark points which will be used later on.

Plot (D) differs from the other three plots as follows; instead of producing limits on sterile neutrino equilibration from scalar decay for different values of λ_S we fix the zero temperature scalar mass to $M_S^0 = 10$ TeV such that $\lambda_S = {}^{(M_s^0)^2}/_{2(v_S^0)^2}$. In plot (D) we set $\alpha = 10^{-8}$.

From the plots in fig. 6.2 different areas can be distinguished:

Sterile neutrino equilibration: within the blue areas sterile neutrinos are expected to equilibrate before or at electroweak symmetry breaking. In this region inverse decays, which have so far been neglected, will become relevant. As a result sterile neutrinos will decohere. We thus expect that any asymmetry previously produced will undergo significant washout in this region.

Slow oscillations: the pink areas denote regions for which $z_{osc} > 1$, this means that the sterile neutrinos will not have developed a $\mathcal{O}(1)$ relative phase shift before electroweak symmetry breaking. As discussed before, almost no asymmetry production is expected in the pink regions.

Thermal oscillations: the yellow/green areas correspond to $z_{osc}/z_c < 1$. This area could be rather interesting because the phase difference from sterile neutrino oscillations is produced before the symmetry breaking of the scalar. Thus, the produced oscillation

Points	v_S^0	y	$Y_{\Delta B}$
A	$10^{7.5}$	$10^{-6.5}$	5.04×10^{-11}
B	10^{7}	10^{-6}	4.96×10^{-11}
C	$10^{6.5}$	$10^{-5.5}$	1.46×10^{-11}

TABLE 6.1: Selected benchmark points. The produced baryon asymmetry for each point is also listed. Throughout $\alpha = 10^{-8}$, $\lambda_{SH} = 10^{-3}$ and $\lambda_S = 10^{-2}$.

timescale is dominated by the *thermal* mass of the sterile neutrino and not the *zero temperature* mass. This would offer a profound difference from the νMSM dynamics. We observe however that this region in general coincides with sterile neutrino equilibration, thus no significant asymmetry will be produced. Note that only for large relative mass splitting α there is a region in which the blue area does not fully overlap with the yellow area. However, ARS leptogenesis with two sterile neutrinos requires that the sterile neutrino masses are strongly degenerate, thus, also here we do not expect significant lepton asymmetry production. The overlap between yellow and blue regions is probably not fully unexpected; for the thermal mass of the sterile neutrino to dominate over the zero temperature mass the yukawa coupling Y needs to be large, at the same time this will of course also result in large scalar decay rates.

Successful leptogenesis: we are thus left with the white region in these plots. In these regions all timescales conspire such that it is in principle possible to produce sufficient lepton asymmetry. Note that for this to happen the mass difference must be small, we therefore choose $\alpha = 10^{-8}$ in all calculations which will follow. In the next section this region will be further investigated.

6.3 Results

We will continue our discussion on efficient lepton asymmetry production by calculating the produced asymmetry for three benchmark points: A, B and C, as defined in table 6.1. Note that these three points correspond to the red stars in fig. 6.2. In order to compare our results to the results calculated within the νMSM these points are chosen to have a zero temperature sterile neutrino mass given by $M_N^0 = 10\,\text{GeV}$. Furthermore, these points have been selected such that they are respectively far away, close to and in the blue region. We thus chose points which have increasing sterile neutrino production from scalar decay.

We can show that each point indeed corresponds to increasing sterile neutrino production by comparing the total sterile neutrino production with the production from

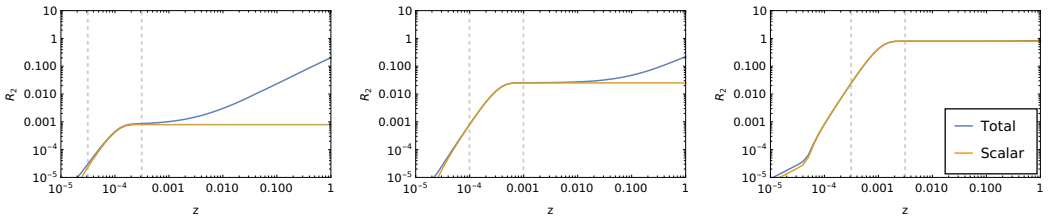

(A) (B) (C)

FIGURE 6.3: Sterile neutrino density $R_N(z)$ for the benchmark points A, B and C. The orange lines correspond to the sterile neutrino production from only the scalar decays, the blue lines correspond to the total sterile neutrino production. See text for more details. From ref. [2]

just scalar decay as defined in eq. (6.7). Results are shown in fig. 6.3. These figures show that indeed the sterile neutrino production increases for benchmark points closer to the blue area. Note that for benchmark point C the sterile neutrino production is completely dominated by scalar decays. The vertical grey dashed lines in these plots correspond $z = z_S$ and $z = 10z_S$, where z_S is determined by solving $M_S(z_S) = T(z_S)$. This shows that the main sterile neutrino production from scalar decay occurs when the scalar thermal mass is approximately equal to the temperature.

From the results summarized in table 6.1 we see that for point A the baryon asymmetry is the same as the baryon asymmetry determined within the νMSM for $M_N = 10$ GeV. For the points B and C the total baryon asymmetry is reduced. From this we can make the preliminary conclusion that additional sterile neutrino production reduces the produced baryon asymmetry, even for moderate production.

To extend this analysis further the baryon asymmetry as a function of the scalar vev has been determined. Results are shown in fig. 6.4. On the left for fixed scalar self coupling $\lambda_S = 10^{-3}$ and three different sterile neutrino masses M_N. And on the right for fixed sterile neutrino mass, $M_N = 10\,\text{GeV}$, and three choices of λ_S. The results in this figure confirm our suspicion that increasing sterile neutrino production from scalar decay only reduces the produced baryon asymmetry. Note that in the limit of negligible production, i.e., for large v_S^0 the produced baryon asymmetry is equivalent to that predicted by the νMSM.

As a final plot we will show a comparison between the baryon asymmetry of the νMSM and the baryon asymmetry of the scalar extension, as a function of the sterile neutrino mass M_N^0. Looking back at plot (C) in fig. 6.2 we can, for $1\,\text{GeV} < M_N^0 < 100\,\text{GeV}$ select points (v_S^0, Y) such that they are on a line parallel to the boundary of the blue areas in fig. 6.2. This line can be parametrized as:

$$\log(v_S^0) = 2\log(Y) + L_i\,, \tag{6.13}$$

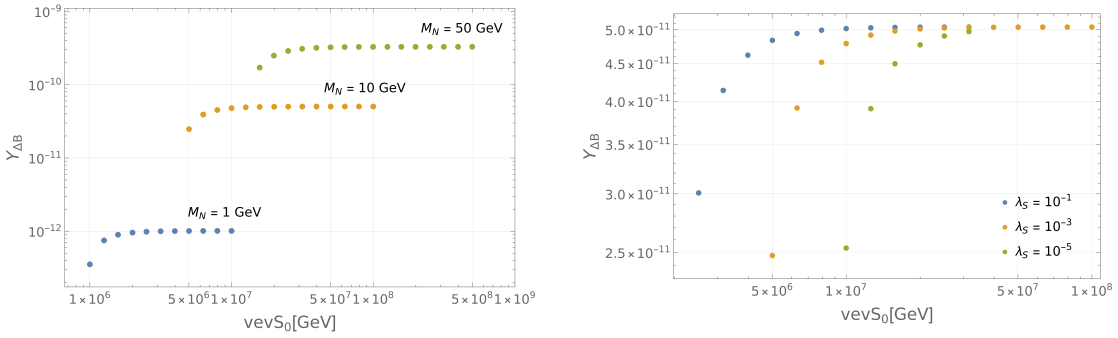

FIGURE 6.4: Baryon asymmetry as a function of the scalar vev v_S^0. On the left for several choices of M_N and on the right for several choices of λ_S. For these plots $\lambda_{SH} = 10^{-3}$ and $\alpha = 10^{-8}$. From ref. [2].

We choose $L_i = 20,\ 18.5,\ 17.5$, corresponding to parallel lines far away, close to, and inside the blue area, respectively. We fix $\lambda_{SH} = 10^{-3}$, $\lambda_S = 10^{-2}$ and $\alpha = 10^{-8}$. Results are shown in fig. 6.5. Similar to previous results, these results show that additional sterile neutrino production mainly affects ARS leptogenesis by reducing the total baryon asymmetry. Note that the peak for which the production is maximized shifts, for increasing sterile neutrino production, to slightly smaller values of M_N^0. This is likely related to the additional equilibration rate of the sterile neutrinos with the thermal bath due to scalar interactions. Furthermore, these results show that for negligible scalar decay the produced baryon asymmetry in the scalar extension is equal to the baryon asymmetry produced in the νMSM, which is exactly what we would expect.

6.4 Discussion

We have seen that in general one thermalized scalar will, through sterile neutrino production from scalar decays, *reduce* the produced baryon asymmetry. This result seems independent of the chosen parameters. The question posed in the introduction, *"can a scalar enhance the baryon asymmetry production in ARS leptogenesis?"*, therefore has to be answered negatively – one thermalized scalar is not able to enhance baryon asymmetry production.

This result, although at first sight somewhat disappointing can still proof useful. If (when) collider searches, or other experiments like gravitational wave experiments, find evidence for the existence of a heavy thermalized scalar the results presented in this chapter will help constrain the possible parameter space for which ARS leptogenesis will be able to explain the observed BAU.

Furthermore we see that in the νMSM with small mass splitting and $M_N \sim 60$ GeV the predicted BAU is actually larger than that observed in experiments. A thermalized

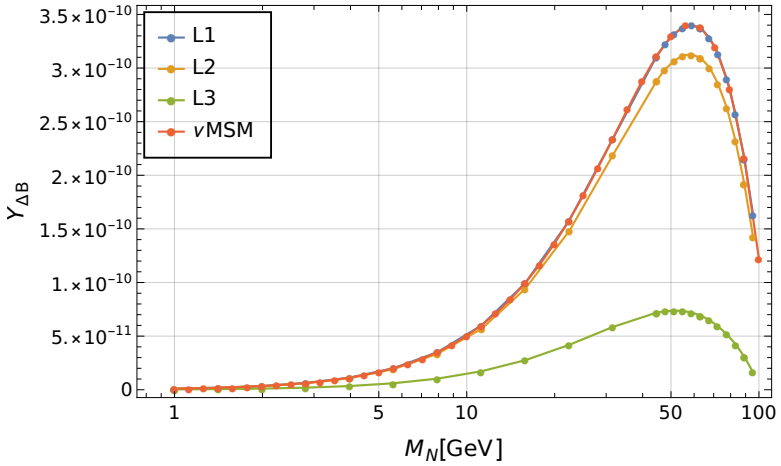

FIGURE 6.5: Baryon asymmetry production as a function of the sterile neutrino mass M_N^0, compared to results obtained for the νMSM. See text for more details. From ref. [2].

scalar which couples sufficiently strong to the sterile neutrinos to reduce the produced BAU, but not strong enough to fully thermalize them, could help alleviate this difference between prediction and observation. Note that there are also many parameters within the νMSM, for example the parameters in eq. (5.11), which one could tune to obtain the same effect. From fig. 6.2 we can also see that the existence of a thermalized scalar with large Yukawa coupling to the sterile neutrinos would rule out leptogenesis via oscillations. Thus, showing that another mechanism or further Standard Model extensions are required to explain the BAU.

In future work it would be interesting to look into Standard Model extensions with multiple scalars. If all new scalars are thermalized with similar vacuum expectation values the results discussed above should not be affected qualitatively. However a combination of a thermalized scalar with vacuum expectation value and a (non)-thermalized scalar without a vacuum expectation value could be interesting since it would break the link between the zero temperature sterile neutrino masses, the thermal sterile neutrino masses and sterile neutrino production from scalar decay. Breaking this link could provide an interesting change to the timescales discussed.

This concludes our discussion on leptogenesis via oscillations and the effect an extra scalar has on this mechanism. In the next chapter this thesis will be wrapped up with a conclusion and discussion to place the results obtained in part A and part B in perspective.

This page was intentionally left blank.

Chapter 7

Conclusion and Discussion

In this thesis we have discussed two distinct Standard Model extensions; a scalar extension and an extension with a strongly coupled dark sector. Each of these extensions has the property that they could be rather weakly coupled to the Standard Model particles, therefore making it difficult to discover signatures of these models in conventional experiments. Luckily, with the advancement of gravitational wave experiments, another window into these theories has opened up.

In part A we have seen that phase transitions in strongly coupled hidden sectors, although quantitatively well understood, are qualitatively not yet as well understood. This is mainly due to the lack of calculations from first principles as a result of the theory being non-perturbative. Consequently, possible gravitational wave signals produced by these hidden sectors are difficult to predict in a reliable manner. With the first detection of gravitational wave signals from a first order phase transition hopefully rapidly approaching, this is somewhat of a problem. Without a reliable prediction of gravitational wave signals, experimental results will not be able to help put limits on hidden sectors, or ideally, proof the existence of a strongly coupled hidden sector. Note that this last point is anyway somewhat hard to achieve because gravitational wave signals mainly depend on a set of macroscopic quantities. Many different underlying SM extensions can produce similar sets of macroscopic quantities, which will make it difficult if not completely impossible to trace gravitational wave signals back to a specific model.

To alleviate this uncertainty somewhat we employed low-energy effective models to approximate the full dynamics of a strongly coupled hidden sector. By using the NJL

model, the PNJL model and the LSM we have been able to calculate the effective potentials as well as the predicted gravitational wave signals, without resorting to approximations as made in previous work. Results show that the peak frequency and signal strength of the GW signals predicted by the effective models can sometimes differ by several orders of magnitude. Additionally, due to the fast phase transitions, predicted gravitational wave signals appear to be rather weak. We have seen that future experiments like DECIGO and BBO are most sensitive to phase transitions in strongly coupled hidden sector which occur around 100 GeV.

These results show that in order for gravitational wave experiments to be of any value towards constraining strongly coupled hidden sectors we need to first understand their phase transitions better. This requires either better effective models, by for example taking into account more diagrams when calculating the effective potential, or the use of lattice calculations. Ideally, lattice calculations could in the future allow us to calculate the phase transition dynamics from first principles, without resorting to effective models.

For a scalar extension the situation is much better understood. Many scalar extensions have been discussed in the literature which result in the electroweak phase transition being first order. This will consequently result in a possibly measurable gravitational wave signal. Once gravitational wave experiments find proof of a first order phase transition it should thus be possible to partially constrain the parameters of these scalar extension. It is therefore interesting to look into other effects an additional scalar has on the Standard Model physics and determine how a scalar can contribute to solving one or more of the many issues the Standard Model has. In particular, in part B we looked into the effect a scalar has on *leptogenesis via oscillations*. The aim of leptogenesis via oscillations, or any other baryogenesis mechanism, is to explain why our universe seems to consist out of mainly baryons and not an equal number of baryons and anti-baryons.

We have shown that a Standard Model extension with one thermalized singlet scalar in general reduces the predicted baryon asymmetry. This reduction is the result of additional sterile neutrino production from scalar decays. A region for which the asymmetry can be enhanced has so far not been found. These results can be used as an additional constraint on a possible scalar extension. More research still has to be done on further scalar extensions, with enough freedom in a scalar sector it might be expected that a region in parameter space can be found for which the produced baryon asymmetry will actually be enhanced. However, explicit calculations are needed to answer this question definitively.

Overall, this thesis has shown that the prospect of detecting first order phase transitions through gravitational wave experiments leads to many interesting avenues to investigate. On the one hand a lot of work remains to be done on calculating gravitational wave signals from Standard Model extension in a reliable and precise manner. On the other hand, once proof of a phase transition is found, this can be used to constrain for example scalar extensions. We have also shown how such scalar extension can be connected to other issues of the Standard Model.

The coming decades will hopefully proof to be an interesting time in particle physics, with many experimental advances in neutrino experiments, collider experiments and gravitational wave experiments.

This page was intentionally left blank.

Appendix A

Thermal QFT and Thermal masses

Unlike particles travelling in vacuum, a particle travelling through a thermal medium will interact with this medium. Standard Quantum Field Theory (QFT) only describes physics at zero temperature in the vacuum. In order to describe physics in a thermal bath one needs Thermal QFT. See for e.g. refs. [57, 151] for more details on Thermal Quantum Field Theory.

Within Thermal QFT there are two main ways in which one can derive thermal effects, the *real time formalism* and the *imaginary time formalism*. In principle these two formalisms are equivalent, however, the imaginary time formalism is only valid in equilibrium. On the other hand, the real-time formalism can also be used to describe non-equilibrium processes [151].

In this Appendix both formalisms will be briefly introduced. In order to get a better understanding of the real and imaginary time formalism we will go through the explicit example of deriving the effective potential, or equivalently the thermal mass, of a scalar in a thermal bath.

A.1 Imaginary time formalism

This formalism was first developed by Matsubara [152]. Within the imaginary time formalism the time variable is exchanged by imaginary time $t \to -i\tau$. For finite temperature τ is a periodic variable: $0 \leq \tau \leq \beta$ and $\beta = 1/T$. It is subsequently possible to use all the standard Feynman techniques, in momentum space, with the following

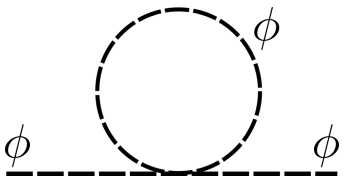

FIGURE A.1: One-loop diagram contributing to the thermal mass of a scalar ϕ.

changes to the scalar propagator and the momentum integration over loop momenta:

$$iD_F(k) \to \tilde{\Delta} = \frac{1}{\omega_n^2 + \omega_k^2}\,, \tag{A.1}$$

$$\int \frac{\mathrm{d}^4 k_E}{(2\pi)^4} \to T\sum_n \int \frac{\mathrm{d}^3 k}{(2\pi)^3}\,. \tag{A.2}$$

For a scalar $\omega_n = n\pi T$ with $n = 0, \pm 1, \pm 2 \ldots$, while for a fermion $\omega_n = (n+1)\pi T$ with $n = 0, \pm 1, \pm 2 \ldots$. The frequency ω_k is defined as $\omega_k^2 = \vec{k}^2 + m^2$

For a scalar self-interaction $\mathcal{L}_{int} = -\frac{1}{4!}\lambda\phi^4$, the one-loop diagram responsible for the thermal mass is shown in fig. A.1.

Following the standard Feynman rules with the changes as given in eqs. (A.1) and (A.2) the two-point function of this diagram is [57]:

$$G_2 = -\Delta m^2 = T\sum_n \int \frac{d^3k}{(2\pi)^3} \frac{-\lambda}{4!} 4 \times 3 \times \frac{1}{k^2 + m^2 + \omega_n^2}\,, \tag{A.3}$$

with $\omega_n = 2\pi n T$ and $n = 0, \pm 1, \pm 2 \ldots$.

Using the residue theorem the sum is equivalent to an integral in complex space, with the contour enclosing all poles $\omega = 2\pi n T$;

$$\begin{aligned} T\sum_n \frac{1}{\omega_n^2 + \epsilon_k^2} &\overset{!}{=} -\frac{1}{2\pi i}\oint \mathrm{d}\omega \frac{1}{\omega^2 - \epsilon_k^2}\frac{1}{2}\coth(\omega/2T) \\ &= -\frac{1}{2\pi i}(2\pi i)\mathrm{Res}\frac{1}{2}\frac{e^{\omega/2T} + e^{-\omega/2T}}{\omega^2 + \epsilon_k^2}\frac{1}{e^{\omega/2T} + e^{-\omega/2T}} \\ &= -\frac{1}{2}\sum_n \lim_{\omega \to 2\pi i n T}\frac{g(\omega)}{h(\omega)} \\ &= T\sum_n \frac{1}{\omega_n^2 + \epsilon_k^2}\,, \end{aligned} \tag{A.4}$$

where we have used L'Hôpital's rule to calculate the limit. Futhermore, $\epsilon_k^2 = k^2 + m^2$. Instead of doing the sum we can now simply calculate the integral using complex integration, this is done by deforming the contour such that it encircles not the poles on the imaginary axis but the poles $\omega = \pm\epsilon_k$; using again the Residue theorem the sum

is thus given by:

$$-\frac{1}{2\pi i}\oint \mathrm{d}\omega \frac{1}{\omega^2-\epsilon_k^2}\frac{1}{2}\coth(\omega/2T) = -\mathrm{Res}\frac{1}{(\omega+\epsilon_k)(\omega-\epsilon_k)}\frac{1}{2}\coth(\omega/2T)$$
$$= \frac{1}{2\epsilon_k}\coth(\epsilon_k/2T)\ . \tag{A.5}$$

Using the above relation the two point function can thus be written as:

$$-\Delta m^2 = -\frac{\lambda}{2}\int \frac{\mathrm{d}^3k}{(2\pi)^3}\frac{1}{2\epsilon_k}\coth(\epsilon_k/2T)\ . \tag{A.6}$$

Through the equality $\coth(\epsilon_k/2T) = 1+2n_B(\epsilon_k)$, this integral can be split up in a divergent zero temperature contribution and a finite, temperature dependent, contribution. $n_B(\epsilon_k)$ is the Bose-Einstein distribution function for scalars; $n_B(\epsilon_k) = \frac{1}{e^{\epsilon_k/T}-1}$. The zero temperature contribution can be dealt with using renormalization.

The finite temperature part can be approximated for high temperatures $m \ll T$ as [57]:

$$\Delta m_T^2 = \frac{\lambda}{2}\int \frac{\mathrm{d}^3k}{(2\pi)^3}\frac{1}{\epsilon_k}n_B(\epsilon_k) \sim \frac{\lambda}{24}T^2\ . \tag{A.7}$$

A.2 Real time formalism

Instead of the imaginary time formalism the real time formalism can also be used to calculate Feynman diagrams at finite temperature. Within the real time formalism the thermal bath is taking into account by changing the propagators of scalars and fermions as,

$$\begin{aligned}
iD_{11}(k) &= \frac{i}{k^2-m^2} + n_B(|k_0|)2\pi\delta(k^2-m^2)\ ,\\
iS_{11}(k) &= (\not{k}+m)\left(\frac{i}{k^2-m^2} - n_F(|k_0|)2\pi\delta(k^2-m^2)\right)\ ,\\
n_B(|k_0|) &= (e^{|k_0|/T}-1)^{-1} = \Theta(k_0)(e^{k_0/T}-1)^{-1} + \Theta(-k_0)(e^{-k_0/T}-1)^{-1}\ ,\\
n_F(|k_0|) &= (e^{|k_0|/T}+1)^{-1} = \Theta(k_0)(e^{k_0/T}+1)^{-1} + \Theta(-k_0)(e^{-k_0/T}+1)^{-1}\ .
\end{aligned} \tag{A.8}$$

Note that in the real time formalism there is also a second branch of propagators, see for example textbooks on thermal quantum field theory like ref. [57]. However, for the one-loop propagators we want to determine in this thesis these propagators are not relevant and we will thus not discuss them here.

Similar to the real-time formalism, we look at a scalar self-interaction $\mathcal{L}_{int} = -\frac{1}{4!}\lambda\phi^4$. The one-loop diagram responsible for the thermal mass is shown in fig. A.1. The two point function from this Feynman diagrams is given as,

$$\begin{aligned} G_2 &= \frac{(-i\lambda)}{2}\int \frac{\mathrm{d}^4k}{(2\pi)^4} iD_{11}(k) \\ &= \frac{-i\lambda}{2}\int \frac{\mathrm{d}^4k}{(2\pi)^4}\left(\frac{i}{k^2-m^2} + n_B(|k_0|)2\pi\delta(k^2-m^2)\right) . \end{aligned} \tag{A.9}$$

The first term corresponds to the divergent zero-temperature loop contribution to the scalar mass, while the second term is the finite temperature contribution. Integrating over k_0 we obtain,

$$\begin{aligned} G_2 = -i\Delta m_T^2 &= \frac{-i\lambda}{2}\int \frac{\mathrm{d}^3k}{(2\pi)^3}\int \mathrm{d}k_0 n_B(k_0)\delta(k_0^2 - \vec{k}^2 - m^2) \\ \Delta m_T^2 &= \frac{\lambda}{2}\int \frac{\mathrm{d}^3k}{(2\pi)^3}\frac{1}{\epsilon_k} n_B(\epsilon_k) , \end{aligned} \tag{A.10}$$

with $\epsilon_k^2 = k^2 + m^2$. This is exactly the same thermal mass as derived within the imaginary time formalism, eq. (A.7).

Appendix B

CJT formalism

We will here go through the steps needed to obtain the CJT effective potential for a simple ϕ^4 scalar field theory, extending the formalism to multiple scalar fields is for example done in ref. [72]. The Lagrangian for this toy model is given by:

$$\mathcal{L} = \frac{1}{2}(\partial_\mu \phi)(\partial^\mu \phi) - \frac{1}{2}m^2\phi^2 - \frac{\lambda}{24}\phi^4 \,. \tag{B.1}$$

Following ref. [72], this potential is shifted around the classical field ϕ_{cl}, i.e. $\phi \to \phi + \phi_{cl}$. Assuming fluctuations are small, only terms linear in ϕ are kept, thus giving a classical potential:

$$U(\phi_{cl}) = \frac{1}{2}m^2\phi_{cl}^2 + \frac{\lambda}{24}\phi_{cl}^4 \,. \tag{B.2}$$

Within the CJT formalism the effective potential is defined in terms of the classical field ϕ and the full propagator G as [74, 75]:

$$V_{\text{CJT}}[\phi_{cl}, G] = U(\phi_{cl}) + \tfrac{1}{2}\int_k \log G^{-1}(k) + \tfrac{1}{2}\int_k \left[\Delta^{-1}(k;\bar{\sigma})G(k) - 1\right] + V_2[\phi_{cl}, G(k)] \,. \tag{B.3}$$

The finite temperature integral is defined as

$$\int_k f(k) := T\sum_{n=-\infty}^{\infty}\int \frac{\mathrm{d}^3\vec{k}}{(2\pi)^3}\, f(\omega_n, \vec{k}) \,, \tag{B.4}$$

with Δ^{-1} the tree-level propagator of the meson,

$$\Delta^{-1}(k;\phi_{cl}) = k^2 + m_{\text{eff}}^2(\phi_{cl}) \,. \tag{B.5}$$

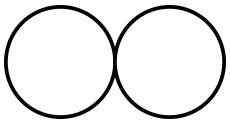

FIGURE B.1: Double bubble diagram contributing to the 2PI potential.

m_{eff} is the effective (zero temperature) mass; $m_{\text{eff}}^2 = m^2 + \frac{1}{2}\lambda\phi_{cl}^2$. The term V_2 is the 2PI effective potential and it thus in principle contains all two-particle-irreducible (2PI) diagrams. In practice it is ofcourse not possible to calculate this exactly, since it would require the inclusion of infinitely many diagrams. In the following V_2 is approximated using the Hartree-Fock approximation [76, 77], which was also used in refs. [72–75]. Within this approximation the only diagram(s) taken into account to determine V_2 is(are) the double bubble diagram(s). Since our toy model only contains one field there is only one diagram contributing to V_2. This double bubble diagram is shown in fig. B.1.

Within the Hartree-Fock approximation V_2 is thus given by:

$$V_2[\phi_{cl}, G(k)] = \frac{1}{8}\lambda \left[\int_k G(\phi_{cl}; k)\right]^2 . \tag{B.6}$$

Note that the propagator used in this equation is the full propagator G. The physical value of $G = G_0$ is determined by minimizing the CJT effective potential, as given in eq. (B.3), with respect to the full propagator G. This minimization results in a gap equation, or alternatively called a fixed point equation, from which G_0 can be determined self consistently:

$$G^{-1}(k;\phi_{cl}) = \Delta^{-1}(k;\phi_{cl}) + \hat{\Pi}[\phi_{cl}, G(k;\phi)] \quad \text{with} \quad \hat{\Pi}[\bar{\sigma}, \hat{G}(k;\bar{\sigma})] := 2\frac{\delta V_2[\phi_{cl}, G(k)]}{\delta G(k)} . \tag{B.7}$$

Note that both the left- and right-hand side of this equation depend on G. Additionally it is also clear that for $V_2 = 0$ the effective potential, eq. (B.3), corresponds to the one-loop particle irreducible effective potential [1]. From this gap-equation G_0 can be determined as the true propagator, in the Hartree-Fock approximation. Using G_0 to calculate the effective potential will then give us an effective potential is term of the classical field ϕ. This is the CJT effective potential.

Substituting V_2, as determined within the Hartree-Fock approximation, in the gap equation we obtain:

$$G^{-1}(k;\phi_{cl}) = k^2 + m^2 + \frac{1}{2}\lambda\phi_{cl}^2 + \frac{1}{2}\lambda\int_k G(\phi_{cl};k) \tag{B.8}$$

$$M(\phi_{cl})^2 = m^2 + \frac{1}{2}\lambda\phi_{cl}^2 + \frac{1}{2}\lambda\int_k \frac{1}{k^2 + M(\phi_{cl})^2} \tag{B.9}$$

Where in the second line we have assumed the full propagator can be written as $G^{-1} = k^2 + M^2$, with M the temperature dependent effective mass [69]. The solution of the second equation gives the physical meson masses M_0. Note that M_0 is not momentum dependent. Putting everything into eq. (B.3), the CJT effective potential in the Hartree-Fock approximation is defined as:

$$\begin{aligned} V_{\text{CJT}}^{HF}[\phi_{cl}] =& \frac{1}{2}m^2\phi_{cl}^2 + \frac{\lambda}{24}\phi_{cl}^4 + \tfrac{1}{2}\int_k \log(k^2+M_0^2) \\ & - \tfrac{1}{2}\left(M_0^2 - m^2 - \frac{1}{2}\lambda\phi_{cl}^2\right)\int_k\left[\frac{1}{k^2+M_0^2}\right] + \frac{1}{8}\lambda\left[\int_k \frac{1}{k^2+M_0^2}\right]^2 \\ =& \frac{1}{2}m^2\phi_{cl}^2 + \frac{\lambda}{24}\phi_{cl}^4 + \tfrac{1}{2}\int_k \log(k^2+M_0^2) - \tfrac{1}{4}\left(M_0^2 - m^2 - \frac{1}{2}\lambda\phi_{cl}^2\right)\int_k\left[\frac{1}{k^2+M_0^2}\right], \end{aligned} \tag{B.10}$$

where in the last equality the gap equation was used to simplify the expression.

These integrals can be calculated within the imaginary time formalism [57], see also appendix A. The second integral is calculated to be,

$$\begin{aligned} \int_k \frac{1}{k^2+M_0^2} &= T\sum_n \int \frac{\mathrm{d}^3k}{(2\pi)^3}\frac{1}{k^2+\omega_n^2+M_0^2} \\ &= \frac{T}{2\pi^2}\int \mathrm{d}k k^2\left[\sum_n \frac{1}{k^2+\omega_n^2+M_0^2}\right] \\ &= \frac{1}{2\pi^2}\int \mathrm{d}k k^2 \frac{1}{2\sqrt{k^2+M_0^2}}\left(1+\frac{2}{\mathrm{e}^{\sqrt{k^2+M_0^2}/T}-1}\right) \\ &= \frac{T^2}{4\pi^2}\int \mathrm{d}x x^2 \frac{1}{\sqrt{x^2+R^2}}\left(1+\frac{2}{\mathrm{e}^{\sqrt{x^2+R^2}}-1}\right) \\ &\equiv \frac{T^2}{2\pi^2} I_B(R^2)\,, \end{aligned} \tag{B.11}$$

with $x = k/T$ and $R^2 = M_0^2/T^2$. Note that in the final line of this equation we have removed the vacuum contributions, following refs. [73, 74] this was shown to not impact the results qualitatively.

The other integral can be straightforwardly derived using,

$$\int_k \frac{1}{k^2+M_0^2} = \int_k \frac{d}{dM_0^2}\log(k^2+M_0^2) \tag{B.12}$$

thus,

$$\begin{aligned}\int_k \log(k^2+M_0^2) &= \int \mathrm{d}M_0^2 \int_k \frac{1}{k^2+M_0^2} \\ &= \frac{T^4}{2\pi^2}\int \mathrm{d}R^2 I_B(R^2) \\ &= \frac{T^4}{\pi^2}\int \mathrm{d}x x^2 \log\left(1-\mathrm{e}^{-\sqrt{x^2+R^2}}\right) \\ &\equiv \frac{T^4}{\pi^2} J_B(R^2)\end{aligned} \tag{B.13}$$

where again variables are changed as $x = k/T$ and $R^2 = M_0^2/T^2$. Also in this integral the vacuum contributions have been neglected.

Combining everything the following CJT effective potential for a single scalar is obtained,

$$V_{\mathrm{CJT}}^{HF}[\phi_{cl}] = \frac{1}{2}m^2\phi_{cl}^2 + \frac{\lambda}{24}\phi_{cl}^4 + \frac{T^4}{2\pi^2}\left(J_B(R^2) - \frac{1}{4}(R^2-r^2)I_B(R^2)\right) \tag{B.14}$$

with $r^2 = m_{\mathrm{eff}}^2/T^2$.

Publications

[1] Alexander J. Helmboldt, Jisuke Kubo, and Susan van der Woude. Observational prospects for gravitational waves from hidden or dark chiral phase transitions. *Phys. Rev. D*, 100(5):055025, 2019. doi: 10.1103/PhysRevD.100.055025

[2] Oliver Fischer, Manfred Lindner, and Susan van der Woude. Robustness of ARS Leptogenesis in Scalar Extensions. 2021. arXiv: 2110.14499 [hep-ph]

References

[1] Alexander J. Helmboldt, Jisuke Kubo, and Susan van der Woude. Observational prospects for gravitational waves from hidden or dark chiral phase transitions. *Phys. Rev. D*, 100(5):055025, 2019. doi: 10.1103/PhysRevD.100.055025.

[2] Oliver Fischer, Manfred Lindner, and Susan van der Woude. Robustness of ARS Leptogenesis in Scalar Extensions. 2021. arXiv: 2110.14499 [hep-ph].

[3] Georges Aad et al. Observation of a new particle in the search for the Standard Model Higgs boson with the ATLAS detector at the LHC. *Phys. Lett. B*, 716:1–29, 2012. doi: 10.1016/j.physletb.2012.08.020.

[4] Serguei Chatrchyan et al. Observation of a New Boson at a Mass of 125 GeV with the CMS Experiment at the LHC. *Phys. Lett. B*, 716:30–61, 2012. doi: 10.1016/j.physletb.2012.08.021.

[5] Albert Einstein. The Foundation of the General Theory of Relativity. *Annalen Phys.*, 49(7):769–822, 1916. doi: 10.1002/andp.200590044.

[6] Clifford M. Will. The Confrontation between General Relativity and Experiment. *Living Rev. Rel.*, 17:4, 2014. doi: 10.12942/lrr-2014-4.

[7] B. P. Abbott et al. Observation of Gravitational Waves from a Binary Black Hole Merger. *Phys. Rev. Lett.*, 116(6):061102, 2016. doi: 10.1103/PhysRevLett.116.061102.

[8] B. P. Abbott et al. Tests of General Relativity with the Binary Black Hole Signals from the LIGO-Virgo Catalog GWTC-1. *Phys. Rev. D*, 100(10):104036, 2019. doi: 10.1103/PhysRevD.100.104036.

[9] Leandros Perivolaropoulos and Foteini Skara. Challenges for ΛCDM: An update. 5 2021.

[10] E. Komatsu et al. Seven-Year Wilkinson Microwave Anisotropy Probe (WMAP) Observations: Cosmological Interpretation. *Astrophys. J. Suppl.*, 192:18, 2011. doi: 10.1088/0067-0049/192/2/18.

[11] P. A. R. Ade et al. Planck 2015 results. XIII. Cosmological parameters. *Astron. Astrophys.*, 594:A13, 2016. doi: 10.1051/0004-6361/201525830.

[12] Jonathan L. Feng. Dark Matter Candidates from Particle Physics and Methods of Detection. *Ann. Rev. Astron. Astrophys.*, 48:495–545, 2010. doi: 10.1146/annurev-astro-082708-101659.

[13] Bernard Carr, Florian Kuhnel, and Marit Sandstad. Primordial Black Holes as Dark Matter. *Phys. Rev. D*, 94(8):083504, 2016. doi: 10.1103/PhysRevD.94.083504.

[14] Joshua Frieman, Michael Turner, and Dragan Huterer. Dark Energy and the Accelerating Universe. *Ann. Rev. Astron. Astrophys.*, 46:385–432, 2008. doi: 10.1146/annurev.astro.46.060407.145243.

[15] Shin'ichi Nojiri and Sergei D. Odintsov. Introduction to modified gravity and gravitational alternative for dark energy. *eConf*, C0602061:06, 2006. doi: 10.1142/S0219887807001928.

[16] G. W. Bennett et al. Final Report of the Muon E821 Anomalous Magnetic Moment Measurement at BNL. *Phys. Rev. D*, 73:072003, 2006. doi: 10.1103/PhysRevD.73.072003.

[17] Elena Graverini. Flavour anomalies: a review. *J. Phys. Conf. Ser.*, 1137(1):012025, 2019. doi: 10.1088/1742-6596/1137/1/012025.

[18] V. A. Kuzmin, V. A. Rubakov, and M. E. Shaposhnikov. On the Anomalous Electroweak Baryon Number Nonconservation in the Early Universe. *Phys. Lett. B*, 155:36, 1985. doi: 10.1016/0370-2693(85)91028-7.

[19] L. Verde, T. Treu, and A. G. Riess. Tensions between the Early and the Late Universe. *Nature Astron.*, 3:891, 7 2019. doi: 10.1038/s41550-019-0902-0.

[20] Sidney R. Coleman and Erick J. Weinberg. Radiative Corrections as the Origin of Spontaneous Symmetry Breaking. *Phys. Rev.*, D7:1888–1910, 1973. doi: 10.1103/PhysRevD.7.1888.

[21] Carlo Marzo, Luca Marzola, and Ville Vaskonen. Phase transition and vacuum stability in the classically conformal B-L model. 2018.

[22] Taeil Hur and P. Ko. Scale invariant extension of the standard model with strongly interacting hidden sector. *Phys. Rev. Lett.*, 106:141802, 2011. doi: 10.1103/PhysRevLett.106.141802.

[23] Martin Holthausen, Jisuke Kubo, Kher Sham Lim, and Manfred Lindner. Electroweak and Conformal Symmetry Breaking by a Strongly Coupled Hidden Sector. *JHEP*, 12:076, 2013. doi: 10.1007/JHEP12(2013)076.

[24] John Ellis, Marek Lewicki, and José Miguel No. On the maximal strength of a first-order electroweak phase transition and its gravitational wave signal. *JCAP*, 1904(04):003, 2019. doi: 10.1088/1475-7516/2019/04/003.

[25] Chiara Caprini et al. Detecting gravitational waves from cosmological phase transitions with LISA: an update. *JCAP*, 03:024, 2020. doi: 10.1088/1475-7516/2020/03/024.

[26] Stefano Profumo, Michael J. Ramsey-Musolf, and Gabe Shaughnessy. Singlet Higgs phenomenology and the electroweak phase transition. *JHEP*, 08:010, 2007. doi: 10.1088/1126-6708/2007/08/010.

[27] Riccardo Apreda, Michele Maggiore, Alberto Nicolis, and Antonio Riotto. Gravitational waves from electroweak phase transitions. *Nucl. Phys. B*, 631:342–368, 2002. doi: 10.1016/S0550-3213(02)00264-X.

[28] Chiara Caprini et al. Science with the space-based interferometer eLISA. II: Gravitational waves from cosmological phase transitions. *JCAP*, 1604(04):001, 2016. doi: 10.1088/1475-7516/2016/04/001.

[29] Evgeny K. Akhmedov, V. A. Rubakov, and A. Yu. Smirnov. Baryogenesis via neutrino oscillations. *Phys. Rev. Lett.*, 81:1359–1362, 1998. doi: 10.1103/PhysRevLett.81.1359.

[30] Takehiko Asaka, Steve Blanchet, and Mikhail Shaposhnikov. The nuMSM, dark matter and neutrino masses. *Phys. Lett. B*, 631:151–156, 2005. doi: 10.1016/j.physletb.2005.09.070.

[31] Yonit Hochberg, Eric Kuflik, Tomer Volansky, and Jay G. Wacker. Mechanism for Thermal Relic Dark Matter of Strongly Interacting Massive Particles. *Phys. Rev. Lett.*, 113:171301, 2014. doi: 10.1103/PhysRevLett.113.171301.

[32] Yonit Hochberg, Eric Kuflik, Hitoshi Murayama, Tomer Volansky, and Jay G. Wacker. Model for Thermal Relic Dark Matter of Strongly Interacting Massive Particles. *Phys. Rev. Lett.*, 115(2):021301, 2015. doi: 10.1103/PhysRevLett.115.021301.

[33] Hooman Davoudiasl and Rabindra N. Mohapatra. On Relating the Genesis of Cosmic Baryons and Dark Matter. *New J. Phys.*, 14:095011, 2012. doi: 10.1088/1367-2630/14/9/095011.

[34] Yang Bai and Pedro Schwaller. Scale of dark QCD. *Phys. Rev.*, D89(6):063522, 2014. doi: 10.1103/PhysRevD.89.063522.

[35] Pedro Schwaller. Gravitational Waves from a Dark Phase Transition. *Phys. Rev. Lett.*, 115(18):181101, 2015. doi: 10.1103/PhysRevLett.115.181101.

[36] Chiara Caprini, Ruth Durrer, and Xavier Siemens. Detection of gravitational waves from the QCD phase transition with pulsar timing arrays. *Phys. Rev.*, D82: 063511, 2010. doi: 10.1103/PhysRevD.82.063511.

[37] Pierre Binetruy, Alejandro Bohe, Chiara Caprini, and Jean-Francois Dufaux. Cosmological Backgrounds of Gravitational Waves and eLISA/NGO: Phase Transitions, Cosmic Strings and Other Sources. *JCAP*, 1206:027, 2012. doi: 10.1088/1475-7516/2012/06/027.

[38] Guy D. Moore, Kari Rummukainen, and Anders Tranberg. Nonperturbative computation of the bubble nucleation rate in the cubic anisotropy model. *JHEP*, 04:017, 2001. doi: 10.1088/1126-6708/2001/04/017.

[39] Guy D. Moore and Kari Rummukainen. Electroweak bubble nucleation, nonperturbatively. *Phys. Rev.*, D63:045002, 2001. doi: 10.1103/PhysRevD.63.045002.

[40] Oliver Gould, Jonathan Kozaczuk, Lauri Niemi, Michael J. Ramsey-Musolf, Tuomas V. I. Tenkanen, and David J. Weir. Nonperturbative analysis of the gravitational waves from a first-order electroweak phase transition. 2019.

[41] Wei-Chih Huang, Manuel Reichert, Francesco Sannino, and Zhi-Wei Wang. Testing the dark SU(N) Yang-Mills theory confined landscape: From the lattice to gravitational waves. *Phys. Rev. D*, 104(3):035005, 2021. doi: 10.1103/PhysRevD.104.035005.

[42] P. A. Zyla et al. Review of Particle Physics. *PTEP*, 2020(8):083C01, 2020. doi: 10.1093/ptep/ptaa104.

[43] Gerard 't Hooft. Symmetry Breaking Through Bell-Jackiw Anomalies. *Phys. Rev. Lett.*, 37:8–11, 1976. doi: 10.1103/PhysRevLett.37.8.

[44] Gerard 't Hooft. Computation of the Quantum Effects Due to a Four-Dimensional Pseudoparticle. *Phys. Rev.*, D14:3432–3450, 1976. doi: 10.1103/PhysRevD.18.2199.3,10.1103/PhysRevD.14.3432.

[45] Frank R. Brown, Frank P. Butler, Hong Chen, Norman H. Christ, Zhi-hua Dong, Wendy Schaffer, Leo I. Unger, and Alessandro Vaccarino. On the existence of a phase transition for QCD with three light quarks. *Phys. Rev. Lett.*, 65:2491–2494, 1990. doi: 10.1103/PhysRevLett.65.2491.

[46] M. A. Stephanov. QCD phase diagram: An Overview. *PoS*, LAT2006:024, 2006. doi: 10.22323/1.032.0024.

[47] Robert D. Pisarski and Frank Wilczek. Remarks on the Chiral Phase Transition in Chromodynamics. *Phys. Rev.*, D29:338–341, 1984. doi: 10.1103/PhysRevD.29.338.

[48] S. P. Klevansky. The Nambu–Jona-Lasinio model of quantum chromodynamics. *Rev. Mod. Phys.*, 64:649–708, 1992. doi: 10.1103/RevModPhys.64.649.

[49] Tetsuo Hatsuda and Teiji Kunihiro. QCD phenomenology based on a chiral effective Lagrangian. *Phys. Rept.*, 247:221–367, 1994. doi: 10.1016/0370-1573(94)90022-1.

[50] Yoichiro Nambu and G. Jona-Lasinio. Dynamical Model of Elementary Particles Based on an Analogy with Superconductivity I. *Phys. Rev.*, 122:345–358, 1961. doi: 10.1103/PhysRev.122.345.

[51] Yoichiro Nambu and G. Jona-Lasinio. Dynamical Model of Elementary Particles Based on an Analogy with Superconductivity II. *Phys. Rev.*, 124:246–254, 1961. doi: 10.1103/PhysRev.124.246. [,141(1961)].

[52] Teiji Kunihiro and Tetsuo Hatsuda. A Selfconsistent Mean Field Approach to the Dynamical Symmetry Breaking: The Effective Potential of the Nambu-Jona-Lasinio Model. *Prog. Theor. Phys.*, 71:1332, 1984. doi: 10.1143/PTP.71.1332.

[53] Mariano Quiros. Finite temperature field theory and phase transitions. In *Proceedings, Summer School in High-energy physics and cosmology: Trieste, Italy, June 29-July 17, 1998*, pages 187–259, 1999.

[54] Manuel Reichert, Francesco Sannino, Zhi-Wei Wang, and Chen Zhang. Dark Confinement and Chiral Phase Transitions: Gravitational Waves vs Matter Representations. 9 2021.

[55] S. Klimt, Matthias F. M. Lutz, U. Vogl, and W. Weise. GENERALIZED SU(3) NAMBU-JONA-LASINIO MODEL. Part. 1. MESONIC MODES. *Nucl. Phys. A*, 516:429–468, 1990. doi: 10.1016/0375-9474(90)90123-4.

[56] Mayumi Aoki, Hiromitsu Goto, and Jisuke Kubo. Gravitational Waves from Hidden QCD Phase Transition. *Phys. Rev.*, D96(7):075045, 2017. doi: 10.1103/PhysRevD.96.075045.

[57] Ashok K. Das. *Finite Temperature Field Theory*. World Scientific, New York, 1997. ISBN 978-981-02-2856-9, 978-981-4498-23-4.

[58] Kenji Fukushima and Vladimir Skokov. Polyakov loop modeling for hot QCD. *Prog. Part. Nucl. Phys.*, 96:154–199, 2017. doi: 10.1016/j.ppnp.2017.05.002.

[59] Kenji Fukushima. Chiral effective model with the Polyakov loop. *Phys. Lett.*, B591:277–284, 2004. doi: 10.1016/j.physletb.2004.04.027.

[60] Simon Roessner, Claudia Ratti, and W. Weise. Polyakov loop, diquarks and the two-flavour phase diagram. *Phys. Rev.*, D75:034007, 2007. doi: 10.1103/PhysRevD.75.034007.

[61] Kenji Fukushima. Phase diagrams in the three-flavor Nambu–Jona-Lasinio model with the Polyakov loop. *Phys. Rev.*, D77:114028, 2008. doi: 10.1103/PhysRevD.77.114028,10.1103/PhysRevD.78.039902. [Erratum: Phys. Rev.D78,039902(2008)].

[62] Bernd-Jochen Schaefer, Jan M. Pawlowski, and Jochen Wambach. The Phase Structure of the Polyakov–Quark-Meson Model. *Phys. Rev.*, D76:074023, 2007. doi: 10.1103/PhysRevD.76.074023.

[63] C. Ratti, Simon Roessner, M. A. Thaler, and W. Weise. Thermodynamics of the PNJL model. *Eur. Phys. J. C*, 49:213–217, 2007. doi: 10.1140/epjc/s10052-006-0065-x.

[64] Jisuke Kubo and Masatoshi Yamada. Scale and confinement phase transitions in scale invariant $SU(N)$ scalar gauge theory. *JHEP*, 10:003, 2018. doi: 10.1007/JHEP10(2018)003.

[65] Murray Gell-Mann and M Levy. The axial vector current in beta decay. *Nuovo Cim.*, 16:705, 1960. doi: 10.1007/BF02859738.

[66] Y. Meurice. Linear sigma model for multiflavor gauge theories. *Phys. Rev.*, D96 (11):114507, 2017. doi: 10.1103/PhysRevD.96.114507.

[67] L. Dolan and R. Jackiw. Gauge Invariant Signal for Gauge Symmetry Breaking. *Phys. Rev.*, D9:2904, 1974. doi: 10.1103/PhysRevD.9.2904.

[68] John M. Cornwall, R. Jackiw, and E. Tomboulis. Effective Action for Composite Operators. *Phys. Rev.*, D10:2428–2445, 1974. doi: 10.1103/PhysRevD.10.2428.

[69] G. Amelino-Camelia and So-Young Pi. Selfconsistent improvement of the finite temperature effective potential. *Phys. Rev.*, D47:2356–2362, 1993. doi: 10.1103/PhysRevD.47.2356.

[70] G. Amelino-Camelia. Selfconsistently improved finite temperature effective potential for gauge theories. *Phys. Rev.*, D49:2740–2751, 1994. doi: 10.1103/PhysRevD.49.2740.

[71] Giovanni Amelino-Camelia. On the CJT formalism in multifield theories. *Nucl. Phys.*, B476:255–274, 1996. doi: 10.1016/0550-3213(96)00374-4.

[72] Nicholas Petropoulos. Linear sigma model and chiral symmetry at finite temperature. *J. Phys.*, G25:2225–2241, 1999. doi: 10.1088/0954-3899/25/11/305.

[73] Jonathan T. Lenaghan and Dirk H. Rischke. The O(N) model at finite temperature: Renormalization of the gap equations in Hartree and large N approximation. *J. Phys.*, G26:431–450, 2000. doi: 10.1088/0954-3899/26/4/309.

[74] Jonathan T. Lenaghan, Dirk H. Rischke, and Jurgen Schaffner-Bielich. Chiral symmetry restoration at nonzero temperature in the SU(3)(r) x SU(3)(l) linear sigma model. *Phys. Rev.*, D62:085008, 2000. doi: 10.1103/PhysRevD.62.085008.

[75] Dirk Röder, Jörg Ruppert, and Dirk H. Rischke. Chiral symmetry restoration in linear sigma models with different numbers of quark flavors. *Phys. Rev.*, D68: 016003, 2003. doi: 10.1103/PhysRevD.68.016003.

[76] V. Fock. Näherungsmethode zur Lösung des quantenmechanischen Mehrkörperproblems. *Zeitschrift für Physik*, 61(1):126–148, 1930. doi: 10.1007/BF01340294.

[77] D. R. Hartree. The Wave Mechanics of an Atom with a Non-Coulomb Central Field. Part I. Theory and Methods. *Mathematical Proceedings of the Cambridge Philosophical Society*, 24(1):89–110, 1928. doi: 10.1017/S0305004100011919.

[78] Albert Einstein. Zur Allgemeinen Relativitätstheorie. *Sitzungsber. Preuss. Akad. Wiss. Berlin (Math. Phys.)*, 1915:778–786, 1915. [Addendum: Sitzungsber.Preuss.Akad.Wiss.Berlin (Math.Phys.) 1915, 799–801 (1915)].

[79] Albert Einstein. Über Gravitationswellen. *Sitzungsber. Preuss. Akad. Wiss. Berlin (Math. Phys.)*, 1918:154–167, 1918.

[80] M. Bailes et al. Gravitational-wave physics and astronomy in the 2020s and 2030s. *Nature Rev. Phys.*, 3(5):344–366, 2021. doi: 10.1038/s42254-021-00303-8.

[81] R. A. Hulse and J. H. Taylor. Discovery of a pulsar in a binary system. *Astrophys. J. Lett.*, 195:L51–L53, 1975. doi: 10.1086/181708.

[82] J. H. Taylor, L. A. Fowler, and P. M. McCulloch. Measurements of general relativistic effects in the binary pulsar PSR 1913+16. *Nature*, 277:437–440, 1979. doi: 10.1038/277437a0.

[83] Joel M. Weisberg and Joseph H. Taylor. Relativistic binary pulsar B1913+16: Thirty years of observations and analysis. *ASP Conf. Ser.*, 328:25, 2005.

[84] B. P. Abbott et al. Multi-messenger Observations of a Binary Neutron Star Merger. *Astrophys. J.*, 848(2):L12, 2017. doi: 10.3847/2041-8213/aa91c9.

[85] B. P. Abbott et al. GW170817: Observation of Gravitational Waves from a Binary Neutron Star Inspiral. *Phys. Rev. Lett.*, 119(16):161101, 2017. doi: 10.1103/PhysRevLett.119.161101.

[86] R. Abbott et al. GWTC-2: Compact Binary Coalescences Observed by LIGO and Virgo During the First Half of the Third Observing Run. *Phys. Rev. X*, 11:021053, 2021. doi: 10.1103/PhysRevX.11.021053.

[87] B. P. Abbott et al. GW150914: The Advanced LIGO Detectors in the Era of First Discoveries. *Phys. Rev. Lett.*, 116(13):131103, 2016. doi: 10.1103/PhysRevLett.116.131103.

[88] Edward Witten. Cosmic Separation of Phases. *Phys. Rev.*, D30:272–285, 1984. doi: 10.1103/PhysRevD.30.272.

[89] C. J. Moore, R. H. Cole, and C. P. L. Berry. Gravitational-wave sensitivity curves. *Class. Quant. Grav.*, 32(1):015014, 2015. doi: 10.1088/0264-9381/32/1/015014.

[90] Benjamin P. Abbott et al. Prospects for Observing and Localizing Gravitational-Wave Transients with Advanced LIGO, Advanced Virgo and KAGRA. *Living Rev. Rel.*, 21:3, 2018. doi: 10.1007/s41114-018-0012-9,10.1007/lrr-2016-1. [Living Rev. Rel.19,1(2016)].

[91] Jose R. Espinosa, Thomas Konstandin, Jose M. No, and Geraldine Servant. Energy Budget of Cosmological First-order Phase Transitions. *JCAP*, 1006:028, 2010. doi: 10.1088/1475-7516/2010/06/028.

[92] John Ellis, Marek Lewicki, José Miguel No, and Ville Vaskonen. Gravitational wave energy budget in strongly supercooled phase transitions. 2019.

[93] Vedran Brdar, Alexander J. Helmboldt, and Jisuke Kubo. Gravitational Waves from First-Order Phase Transitions: LIGO as a Window to Unexplored Seesaw Scales. *JCAP*, 1902(02):021, 2019. doi: 10.1088/1475-7516/2019/02/021.

[94] Andrei D. Linde. Decay of the False Vacuum at Finite Temperature. *Nucl. Phys.*, B216:421, 1983. doi: 10.1016/0550-3213(83)90293-6,10.1016/0550-3213(83)90072-X. [Erratum: Nucl. Phys.B223,544(1983)].

[95] Andrei D. Linde. Fate of the False Vacuum at Finite Temperature: Theory and Applications. *Phys. Lett. B*, 100:37–40, 1981. doi: 10.1016/0370-2693(81)90281-1.

[96] Carroll L. Wainwright. CosmoTransitions: Computing Cosmological Phase Transition Temperatures and Bubble Profiles with Multiple Fields. *Comput. Phys. Commun.*, 183:2006–2013, 2012. doi: 10.1016/j.cpc.2012.04.004.

[97] Mark Hindmarsh, Stephan J. Huber, Kari Rummukainen, and David J. Weir. Numerical simulations of acoustically generated gravitational waves at a first order phase transition. *Phys. Rev.*, D92(12):123009, 2015. doi: 10.1103/PhysRevD.92.123009.

[98] Marc Kamionkowski, Arthur Kosowsky, and Michael S. Turner. Gravitational radiation from first order phase transitions. *Phys. Rev.*, D49:2837–2851, 1994. doi: 10.1103/PhysRevD.49.2837.

[99] Mark Hindmarsh, Stephan J. Huber, Kari Rummukainen, and David J. Weir. Shape of the acoustic gravitational wave power spectrum from a first order phase transition. *Phys. Rev.*, D96(10):103520, 2017. doi: 10.1103/PhysRevD.96.103520.

[100] Kazuaki Kuroda, Wei-Tou Ni, and Wei-Ping Pan. Gravitational waves: Classification, Methods of detection, Sensitivities, and Sources. *Int. J. Mod. Phys.*, D24 (14):1530031, 2015. doi: 10.1142/S0218271815300311.

[101] M. Punturo et al. The Einstein Telescope: A third-generation gravitational wave observatory. *Class. Quant. Grav.*, 27:194002, 2010. doi: 10.1088/0264-9381/27/19/194002.

[102] M. Punturo et al. The third generation of gravitational wave observatories and their science reach. *Class. Quant. Grav.*, 27:084007, 2010. doi: 10.1088/0264-9381/27/8/084007.

[103] Pau Amaro-Seoane et al. eLISA/NGO: Astrophysics and cosmology in the gravitational-wave millihertz regime. *GW Notes*, 6:4–110, 2013.

[104] Pau Amaro-Seoane et al. Laser Interferometer Space Antenna. 2 2017.

[105] Kent Yagi, Norihiro Tanahashi, and Takahiro Tanaka. Probing the size of extra dimension with gravitational wave astronomy. *Phys. Rev.*, D83:084036, 2011. doi: 10.1103/PhysRevD.83.084036.

[106] Soichiro Isoyama, Hiroyuki Nakano, and Takashi Nakamura. Multiband Gravitational-Wave Astronomy: Observing binary inspirals with a decihertz detector, B-DECIGO. *PTEP*, 2018(7):073E01, 2018. doi: 10.1093/ptep/pty078.

[107] Eric Thrane and Joseph D. Romano. Sensitivity curves for searches for gravitational-wave backgrounds. *Phys. Rev.*, D88(12):124032, 2013. doi: 10.1103/PhysRevD.88.124032.

[108] Kent Yagi. Scientific Potential of DECIGO Pathfinder and Testing GR with Space-Borne Gravitational Wave Interferometers. *Int. J. Mod. Phys.*, D22:1341013, 2013. doi: 10.1142/S0218271813410137.

[109] Hiroaki Kohyama, Diji Kimura, and Tomohiro Inagaki. Parameter fitting in three-flavor Nambu–Jona-Lasinio model with various regularizations. *Nucl. Phys.*, B906:524–548, 2016. doi: 10.1016/j.nuclphysb.2016.03.015.

[110] C. J. Hogan. Nucleation of cosmological phase transitions. *Phys. Lett.*, 133B:172–176, 1983. doi: 10.1016/0370-2693(83)90553-1.

[111] Koji Tsumura, Masatoshi Yamada, and Yuya Yamaguchi. Gravitational wave from dark sector with dark pion. *JCAP*, 1707(07):044, 2017. doi: 10.1088/1475-7516/2017/07/044.

[112] Chiara Caprini and Daniel G. Figueroa. Cosmological Backgrounds of Gravitational Waves. *Class. Quant. Grav.*, 35(16):163001, 2018. doi: 10.1088/1361-6382/aac608.

[113] Takehiko Asaka and Mikhail Shaposhnikov. The νMSM, dark matter and baryon asymmetry of the universe. *Phys. Lett. B*, 620:17–26, 2005. doi: 10.1016/j.physletb.2005.06.020.

[114] Takehiko Asaka, Shintaro Eijima, and Hiroyuki Ishida. Kinetic Equations for Baryogenesis via Sterile Neutrino Oscillation. *JCAP*, 02:021, 2012. doi: 10.1088/1475-7516/2012/02/021.

[115] Sacha Davidson, Enrico Nardi, and Yosef Nir. Leptogenesis. *Phys. Rept.*, 466:105–177, 2008. doi: 10.1016/j.physrep.2008.06.002.

[116] Lars Husdal. On Effective Degrees of Freedom in the Early Universe. *Galaxies*, 4 (4):78, 2016. doi: 10.3390/galaxies4040078.

[117] A. D. Sakharov. Violation of CP Invariance, C asymmetry, and baryon asymmetry of the universe. *Pisma Zh. Eksp. Teor. Fiz.*, 5:32–35, 1967. doi: 10.1070/PU1991v034n05ABEH002497.

[118] Jeffrey A. Harvey and Michael S. Turner. Cosmological baryon and lepton number in the presence of electroweak fermion number violation. *Phys. Rev. D*, 42:3344–3349, 1990. doi: 10.1103/PhysRevD.42.3344.

[119] Mu-Chun Chen. TASI 2006 Lectures on Leptogenesis. In *Theoretical Advanced Study Institute in Elementary Particle Physics: Exploring New Frontiers Using Colliders and Neutrinos*, pages 123–176, 3 2007.

[120] W. Buchmuller, R. D. Peccei, and T. Yanagida. Leptogenesis as the origin of matter. *Ann. Rev. Nucl. Part. Sci.*, 55:311–355, 2005. doi: 10.1146/annurev.nucl.55.090704.151558.

[121] Karin Dick, Manfred Lindner, Michael Ratz, and David Wright. Leptogenesis with Dirac neutrinos. *Phys. Rev. Lett.*, 84:4039–4042, 2000. doi: 10.1103/PhysRevLett.84.4039.

[122] M. Fukugita and T. Yanagida. Baryogenesis Without Grand Unification. *Phys. Lett. B*, 174:45–47, 1986. doi: 10.1016/0370-2693(86)91126-3.

[123] Motohiko Yoshimura. Unified Gauge Theories and the Baryon Number of the Universe. *Phys. Rev. Lett.*, 41:281–284, 1978. doi: 10.1103/PhysRevLett.41.281. [Erratum: Phys.Rev.Lett. 42, 746 (1979)].

[124] Apostolos Pilaftsis and Thomas E. J. Underwood. Resonant leptogenesis. *Nucl. Phys. B*, 692:303–345, 2004. doi: 10.1016/j.nuclphysb.2004.05.029.

[125] A. D. Dolgov. NonGUT baryogenesis. *Phys. Rept.*, 222:309–386, 1992. doi: 10.1016/0370-1573(92)90107-B.

[126] A. D. Dolgov. Baryogenesis, 30 years after. In *25th ITEP Winter School of Physics*, 7 1997. doi: 10.1080/01422419808240874.

[127] Apostolos Pilaftsis and Daniele Teresi. Symmetry Improved CJT Effective Action. *Nucl. Phys.*, B874(2):594–619, 2013. doi: 10.1016/j.nuclphysb.2013.06.004.

[128] Sacha Davidson and Alejandro Ibarra. A Lower bound on the right-handed neutrino mass from leptogenesis. *Phys. Lett. B*, 535:25–32, 2002. doi: 10.1016/S0370-2693(02)01735-5.

[129] J. A. Casas and A. Ibarra. Oscillating neutrinos and $\mu \to e, \gamma$. *Nucl. Phys. B*, 618:171–204, 2001. doi: 10.1016/S0550-3213(01)00475-8.

[130] Takehiko Asaka, Shintaro Eijima, and Hiroyuki Ishida. Mixing of Active and Sterile Neutrinos. *JHEP*, 04:011, 2011. doi: 10.1007/JHEP04(2011)011.

[131] Juraj Klarić, Mikhail Shaposhnikov, and Inar Timiryasov. Uniting Low-Scale Leptogenesis Mechanisms. *Phys. Rev. Lett.*, 127(11):111802, 2021. doi: 10.1103/PhysRevLett.127.111802.

[132] Juraj Klarić, Mikhail Shaposhnikov, and Inar Timiryasov. Reconciling resonant leptogenesis and baryogenesis via neutrino oscillations. *Phys. Rev. D*, 104(5):055010, 2021. doi: 10.1103/PhysRevD.104.055010.

[133] Asmaa Abada, Giorgio Arcadi, Valerie Domcke, Marco Drewes, Juraj Klaric, and Michele Lucente. Low-scale leptogenesis with three heavy neutrinos. *JHEP*, 01: 164, 2019. doi: 10.1007/JHEP01(2019)164.

[134] G. Sigl and G. Raffelt. General kinetic description of relativistic mixed neutrinos. *Nucl. Phys. B*, 406:423–451, 1993. doi: 10.1016/0550-3213(93)90175-O.

[135] H. Arthur Weldon. Effective Fermion Masses of Order gT in High Temperature Gauge Theories with Exact Chiral Invariance. *Phys. Rev. D*, 26:2789, 1982. doi: 10.1103/PhysRevD.26.2789.

[136] José F. Nieves and Sarira Sahu. Neutrino effective potential in a fermion and scalar background. *Phys. Rev. D*, 98(6):063003, 2018. doi: 10.1103/PhysRevD.98.063003.

[137] Brian Shuve and Itay Yavin. Baryogenesis through Neutrino Oscillations: A Unified Perspective. *Phys. Rev. D*, 89(7):075014, 2014. doi: 10.1103/PhysRevD.89.075014.

[138] Frank F. Deppisch, Tomas E. Gonzalo, and Lukas Graf. Surveying the SO(10) Model Landscape: The Left-Right Symmetric Case. *Phys. Rev. D*, 96(5):055003, 2017. doi: 10.1103/PhysRevD.96.055003.

[139] Dibyendu Nanda and Debasish Borah. Common origin of neutrino mass and dark matter from anomaly cancellation requirements of a $U(1)_{B-L}$ model. *Phys. Rev. D*, 96(11):115014, 2017. doi: 10.1103/PhysRevD.96.115014.

[140] Alexander J. Helmboldt, Pascal Humbert, Manfred Lindner, and Juri Smirnov. Minimal conformal extensions of the Higgs sector. *JHEP*, 07:113, 2017. doi: 10.1007/JHEP07(2017)113.

[141] Miguel Escudero and Samuel J. Witte. The hubble tension as a hint of leptogenesis and neutrino mass generation. *Eur. Phys. J. C*, 81(6):515, 2021. doi: 10.1140/epjc/s10052-021-09276-5.

[142] Andrea Caputo, Pilar Hernandez, and Nuria Rius. Leptogenesis from oscillations and dark matter. *Eur. Phys. J. C*, 79(7):574, 2019. doi: 10.1140/epjc/s10052-019-7083-y.

[143] Lorenzo Basso, Alexander Belyaev, Stefano Moretti, and Claire H. Shepherd-Themistocleous. Phenomenology of the minimal B-L extension of the Standard model: Z' and neutrinos. *Phys. Rev. D*, 80:055030, 2009. doi: 10.1103/PhysRevD.80.055030.

[144] Satoshi Iso, Nobuchika Okada, and Yuta Orikasa. Classically conformal B^- L extended Standard Model. *Phys. Lett. B*, 676:81–87, 2009. doi: 10.1016/j.physletb.2009.04.046.

[145] Mikhail Shaposhnikov and Igor Tkachev. The nuMSM, inflation, and dark matter. *Phys. Lett. B*, 639:414–417, 2006. doi: 10.1016/j.physletb.2006.06.063.

[146] Marco Drewes and Jin U Kang. Sterile neutrino Dark Matter production from scalar decay in a thermal bath. *JHEP*, 05:051, 2016. doi: 10.1007/JHEP05(2016)051.

[147] Kari Enqvist, Sami Nurmi, Tommi Tenkanen, and Kimmo Tuominen. Standard Model with a real singlet scalar and inflation. *JCAP*, 08:035, 2014. doi: 10.1088/1475-7516/2014/08/035.

[148] T. Robens. Extended scalar sectors at current and future colliders. In *55th Rencontres de Moriond on QCD and High Energy Interactions*, 5 2021.

[149] Laurent Canetti, Marco Drewes, Tibor Frossard, and Mikhail Shaposhnikov. Dark Matter, Baryogenesis and Neutrino Oscillations from Right Handed Neutrinos. *Phys. Rev. D*, 87:093006, 2013. doi: 10.1103/PhysRevD.87.093006.

[150] Graciela B. Gelmini, Alexander Kusenko, and Volodymyr Takhistov. Possible Hints of Sterile Neutrinos in Recent Measurements of the Hubble Parameter. *JCAP*, 06:002, 2021. doi: 10.1088/1475-7516/2021/06/002.

[151] N. P. Landsman and C. G. van Weert. Real and Imaginary Time Field Theory at Finite Temperature and Density. *Phys. Rept.*, 145:141, 1987. doi: 10.1016/0370-1573(87)90121-9.

[152] Takeo Matsubara. A New approach to quantum statistical mechanics. *Prog. Theor. Phys.*, 14:351–378, 1955. doi: 10.1143/PTP.14.351.